12-2013

A Study of the Optical and Negative Ion Properties of Selected Chiral Molecules

Jason Michael Lambert
University of Tennessee - Knoxville, jlamber9@utk.edu

To the Graduate Council:

I am submitting herewith a dissertation written by Jason Michael Lambert entitled "A Study of the Optical and Negative Ion Properties of Selected Chiral Molecules." I have examined the final electronic copy of this dissertation for form and content and recommend that it be accepted in partial fulfillment of the requirements for the degree of Doctor of Philosophy, with a major in Physics.

Robert N. Compton, Major Professor

We have read this dissertation and recommend its acceptance:

Robert Hinde, Joseph Macek, Stuart Elston, Chuck Feigerle

Accepted for the Council:

Carolyn R. Hodges

Vice Provost and Dean of the Graduate School

(Original signatures are on file with official student records.)

A Study of the Optical and Negative Ion Properties of Selected Chiral Molecules

A Dissertation Presented for the

Doctor of Philosophy

Degree

The University of Tennessee, Knoxville

Jason Michael Lambert

December 2013

dedictation

I want to dedicate this to my wife whose tireless support and encouragement even when she was having the toughest times has helped me persevere. I would also like to dedicate this to my grandmother who always encouraged and supported me when I was growing up. Finally I would like to dedicate this to my Son Isaac and any future children that I have.

Acknowledgements

I would like to acknowledge all the people who acted as advocates for me throughout life. Without there work I could not have made it as far as I have. Particularly the admissions people a Berea College for providing a turning point in my life that set me on a new direction. Also, I want to think the people who demanded excellence out of me and forced me to push myself. I would like to acknowledge my advisor for working with me and helping me reach this goal.

Abstract

Chirality is subtle geometric property where objects lack reflection plane symmetry. In this thesis I study three chiral molecules using a combination of experimental and theoretical methods to elucidate the relationships between conformation freedom, solvent choice, and temperature. The importance of nuclear motion when predicting the optical rotation is explored. For carvone, corrections with each nuclear mode coordinate is important. Predictions of the ORD have the incorrect sign without the inclusion of vibrational corrections. For the case of two newly synthesized amino acid derivatives the vibrational corrections did not correct the sign of the calculated ORD to bring it into agreement with experiment. This case is still an unanswered question. Additionally, I measured the negative ion properties of the dehydrogenated amino acid derivatives and a cluster of the dehydrogenated ion and neutral with collision induced dissociation and used these results to estimate the bond dissociation energies.

Table of Contents

List of Tables

List of Figures

Chapter 1

An Introduction to Chirality

1.1 Overview of Content

This thesis represents a comprehensive study of the molecule carvone and the two newly synthesized molecules, N-paranitrophenylsulfonylalanine and N-paranitrophenylalanine. Chapter 1 is devoted to the historical development and theoretical overview of the concept of optical activity. Chapter 2 is a computational and experimental study of optical rotatory dispersion of carvone in a variety of solvents. Chapter 3 is devoted to the temperature dependence of the circular dichroism and estimations of the difference in Gibb's Free energy(ΔG), enthaply(ΔH), and entropy(ΔS) between enantiomers. Chapters 2 and 3 are closely related and reference each other frequently. Chapters 4 and 5 are devoted to the study of N-paranitrophenylsulfonylalanine and N-paranitrophenylalanine. Chapter 4 is a study of the valence and deprotonated ions of N-paranitrophenylsulfonylalanine, N-paranitrophenylalanine and a cluster of the N-paranitrophenylsulfonylalanine parent with the dehydrogenated ion. Chapter 5 is an experimental and computational study of of optical rotation and circular dichroism of N-paranitrophenylsulfonylalanine and N-paranitrophenylalanine. This thesis uses several different approaches in quantum chemistry including density functional theory, Mossler Plesset perturbation theory, and coupled cluster theory to name a few. The

basis for the methods included herein can be found in textbooks and therefore will not be discussed in great depth. A good source explaining the methods of quantum chemistry can be found in the textbook by Ira N. Levine.[1]

1.2 An Introduction to the Concept of Chirality

It always amazes me that nature, even from the subtlest difference creates such richness and depth of phenomena. Chirality is a subtle property but it is extremely important to many branches of science. An object is said to be chiral if no set of translations and rotations can map it onto its mirror image. This can exist in two or three dimensions. For example, the letter "P" is chiral if it is confined to two dimensions. In chemistry, chiral molecules are molecules that lack a reflection plane symmetry which is to say that they belong to the point groups C_n, D_n, T, O or I. This reason for this will be discussed later in this chapter.[2]

In biology, the vast majority of amino acids in biological systems are of one handedness, referred to as "L " amino acids. The implication of this being that biological systems have a specific chirality. The "D " amino acids in your mirror image could not be used by you for biological processes. There are many other ways in which chirality manifests itself in the biological world. For example, the light reflected of the green irradescent June Bug(Cotinis nitida) is left circularly polarized light*. In physics, chirality also manifests itself in many ways. According to Hubble's law, galaxies are moving away from us at an expanded rate the further they are away. If the projection of a galaxies angular momentum on the earth galaxy vector is non-zero, then the galaxy is chiral because of rotational motion. Photons have a spin angular momentum either parallel or antiparallel to their direction of propagation which makes them chiral. At the intersection between physics and biology it has been proposed that the so called Parity Violating Energy Difference (P.V.E.D.) is responsible for the asymmetry in the number of L versus D amino acids.[3] This energy difference results from the interaction of the weak force of the nucleus with the electrons and results in a very slight energy difference between two different enantiomers. The true enantiomer is the

*left circularly polarized light corresponds to light with right handed helicity

mirror image molecule but made of the corresponding antiparticles since charge and parity are conserved. An enhancement of either L or D amino acids is required for life to begin.

1.3 Historical Overview of Optical Activity

The study of optical activity began with its first observation by Arago in 1811. He observed that when quartz was placed between sunlight reflected from glass and spar that the ordinary and extraordinary rays would change color as the spar was rotated. The spar acted as a polarizer. Biot followed the work of Arago and published 5 works in the span of 26 years (1812-1838).[4] He discovered that quartz rotated the polarization vector of light and that the amount of rotation depended upon the thickness of the crystal and the wavelength. He noted that the angle of rotation was larger for shorter wavelengths of light. This led to the development of the the first inverse square law for optical rotatory dispersion. He also discovered that the other handedness of quartz rotated the polarization in opposite direction. He later discovered optical rotation in several organic compounds. In an attempt to measure the optical activity of a gas, Biot filled a 30 meter long iron tube with turpentine. Unfortunately the boiler exploded and set fire to the church(See page 101 of Lowry[4] for a diagram of the instrument). Biot was able to determine that the sample did have an optical rotation but was unable to quantify the rotation.

The connection between the molecular chirality and optical activity was first inferred by Pastuer in a famous experiment using sodium ammonium tartrate. He observed that there were three forms of the crystals, two of which were chiral. The rotation of the left handed crystal rotated light to the left when dissolved and vice versa for the right handed crystals[†]. This crystallization of these salt solutions into chiral crystals was the first time a racemic mixture has been resolved into its chiral elements.[4] More importantly, the observation of optical rotation in the solution showed that molecules themselves could be chiral.

[†]left and right handed is a colloquial term referring to the enantiomer

1.3.1 The Connections Between Chirality, Biology, and Optical Activity

The relationship between chirality and biology was also first established by Pastuer. He fermented racemic ammonium tartrate and monitored its optical rotation over time. The yeast consumed the dextrorotarory tartate while leaving the levorotatory untouched.[4] All amino acids save glycine are chiral. For the most part these amino acids are L amino acids in biological systems with rare exceptions.[5] Humans can distingiush between select chiral molecules by scent.[6] Some recent research has correlated the rigidity of the molecule and whether the scent between enantiomers was distingiushable.[7] They found that nonrigid molecules were more easily dinstingiushable.

Because of the inherent chirality of biological systems, any compound created to affect a biological system must take chirality into account. For example, a large number of drugs are chiral. In many cases one enantiomer is inactive or has an effect that is weaker or even detrimental to the user. One of the more nefarious examples of enantomeric interactions of chiral drugs with humans is Thalidomide. Thalidomide was used as a treatment for morning sickness in pregnant women.[8] It was long believed that one enantiomer of the drug caused horrible birth defects while the other was an effective treatment option. However, it was later found that thalidomide chemically racemizes in the blood so isolation of the proper enantiomer did not prevent birth defects. Pesticides represent another area where stereoselectivity has an effect. The specific chirality of the pesticide has some effects on the toxicity and biological decay rate.[9]

Life is made up of L amino acids and D sugars but the science behind this so called homochirality is yet to be discovered. There have been several hypotheses proposed for the specific homochirality.[10] A hypothesis by Yamagata for this discrepancy is the parity violating energy difference between enantiomers.[3] This small energy difference results from the interaction of the weak force with the enantiomers of the molecule. It occurs when electrons interact with the nucleus in the chiral center of the molecule. There have been several attempts at measuring this energy difference. This remains an active area of research. Lahamer et. al. quoted a measured value of $\approx 10^{-10} eV$ for an chiral iron complex but they could not rule out the effects of crystalline strain.[11] Since the parity voilating energy

difference scales with the atomic number of the nucleus as $Z^{6.2}$ it is therefore advantageous to explore compounds that have a large Z nuclei at the chiral center. An ideal case would be a high Z nucleus that can be probed with multiple techniques like NMR and Mossbauer spectroscopy. Other attempts are centered around looking for enantiomeric enrichment of a racemic mixture because of the slight energy difference between enantiomers.[12] Another approach is the measurement of the parity violating energy difference by means of infrared absorption spectroscopy.[13] Other hypotheses look to outer space where amino acids can be enriched by selective degradation by ultraviolet circularly polarized light. The Murchison meteorite was found to have an enantomeric excess of the L enantiomer amino acid leading to the hypothesis that homochirality comes from an enantiomeric enrichment of organics in the solar system.

1.4 Electromagnetic theory of optical activity

Optical activity, at least as it pertains to chiral molecules, results from the difference in absorption and dispersion of circularly polarized light. This includes multiphoton processes such as Raman optical activity(ROA) and multiphoton ionization. The electromagnetic implications of optical activity are seen below. Consider an electromagnetic wave propagating in a material where the complex index of refraction is different for left and right circularly polarized light. Light that was initially linearly polarized that passes through a chiral sample can be expressed with the Equation 1.1

$$\frac{E}{E_0} = \frac{1}{\sqrt{2}} \begin{bmatrix} 1 \\ i \end{bmatrix} e^{i(k(n_l + ic\kappa_l)z - \omega t)} + \frac{1}{\sqrt{2}} \begin{bmatrix} 1 \\ -i \end{bmatrix} e^{i(k(n_r + ic\kappa_r)z - \omega t)} \tag{1.1}$$

where l and r subscripts refer to left and right circular polarization and c is the concentration.[‡] The column vectors are unit vectors for left and right circularly polarized

[‡]When measuring the ellipticity, you are making observations at a fixed position in space and the light is coming toward you

light and will from this point on be referred to as $\hat{\mathbf{e}}_\mathbf{r}$ and $\hat{\mathbf{e}}_\mathbf{l}$ from this point.

$$\hat{\mathbf{e}}_\mathbf{l} = \frac{1}{\sqrt{2}} \begin{bmatrix} 1 \\ i \end{bmatrix} \tag{1.2}$$

$$\hat{\mathbf{e}}_\mathbf{r} = \frac{1}{\sqrt{2}} \begin{bmatrix} 1 \\ -i \end{bmatrix} \tag{1.3}$$

After passing through a chiral sample of thickness d, the electric field has been modified in two ways. First, a differential absorption occurs between the left and right components of the light and second, a phase shift is introduced between left and right circularly polarized light.

$$\frac{E}{E_0} = e^{i(k(n_l + ic\kappa_l)d)}\hat{\mathbf{e}}_\mathbf{l} + e^{i(k(n_r + ic\kappa_r)d}\hat{\mathbf{e}}_\mathbf{r} \tag{1.4}$$

From equation 1.4 the magnitude of the two effects is easily extracted. The phase shift introduced between the left and right circularly polarized light is given as $\alpha = \frac{\pi(n_l - n_r)d}{\lambda}$[§] Hence, the rotation per unit length is given by $\phi = \frac{\pi}{\lambda}(n_l - n_r)$. The effects are easily seen upon inspection of the polarization ellipse.

The semi-major axis magnitude is given by the sum $|e^{-\kappa_r kcd} + e^{-\kappa_l kcd}|$ when the electric field of the left and right circularly polarized light parallel. Conversely, the magnitude of the semi-minor axis of the polarization ellipse is given by $|e^{-\kappa_l kcd} - e^{-\kappa_r kcd}|$. The angle β in Figure 1.1 and Equation 1.5 is one measure of the ECD.

$$tan(\beta) = \frac{e^{\kappa_r kcd} - e^{-\kappa_l kcd}}{e^{-\kappa_r kcd} + e^{-\kappa_l kcd}} \tag{1.5}$$

where κ is the aforementioned exctinction coefficient for left and right circularly polarized light. Therefore, linearly polarized light propagating through a chiral sample will become elliptically polarized. The semi-major axis of the polarization ellipse will make an angle α between the initial direction of polarization and the semi-major axis of the ellipse after passing through the sample. We can rewrite Equation 1.5 to make it more succint, resulting

[§]when you add a positive phase to left circularly polarized light the electric field rotates by $-\phi$. For right circularly polarized light the electric field rotates by $-\phi$ for a negative phase shift.

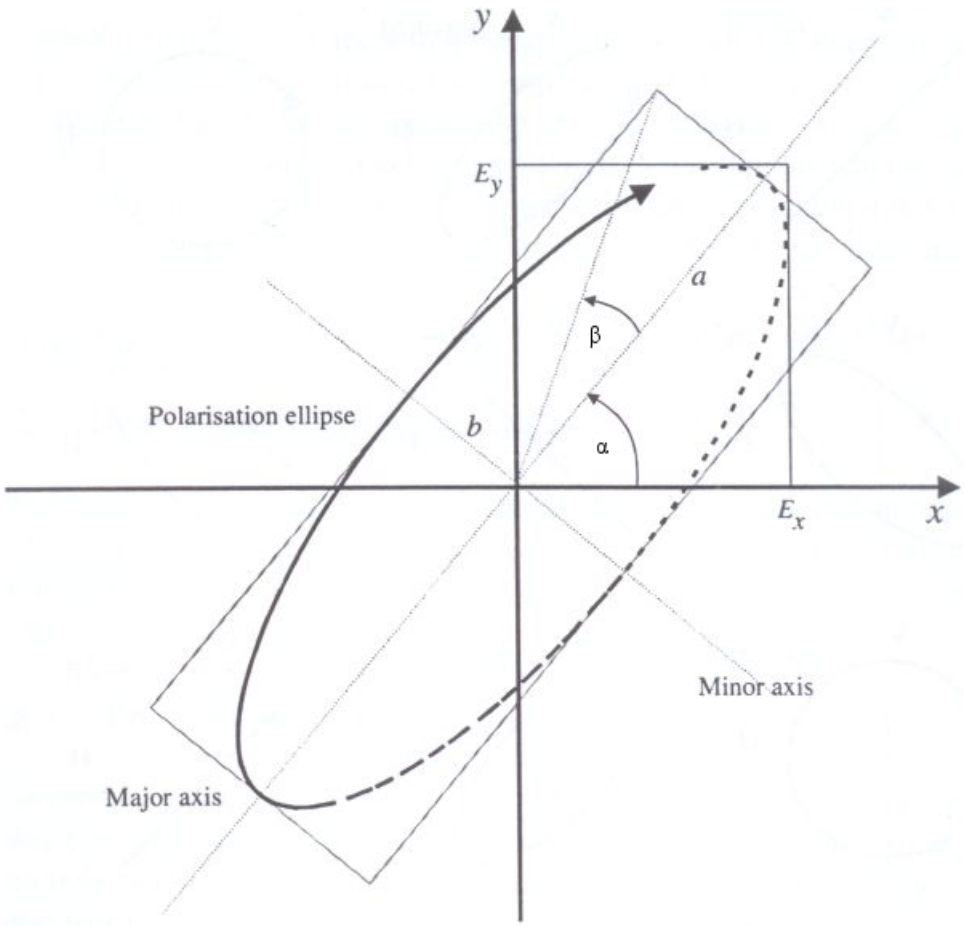

Figure 1.1: The polarization ellipse after light linearly polarized in the x direction passes through a chiral sample. The resulting light is elliptically polarized.

in Equation 1.6

$$\tan(\beta) = \tanh\left(\frac{(\kappa_r - \kappa_l)\pi cd}{\lambda}\right) \tag{1.6}$$

Typically, since absorption is usually measured with a base 10 law i.e. $I = I_0 10^{-A}$ it is useful to express the difference in absorption as the difference between concentration and path-length normalized absorption coefficients. Equation 1.7 converts from degrees of ellipticity to the concentration and path-length normalized difference in absorption between right and left circularly polarized light.

$$\Delta\epsilon = \frac{4}{\ln(10)cl}\operatorname{arctanh}\left(\tan\left(\frac{\beta\pi}{180}\right)\right) \tag{1.7}$$

where θ is the angle in degrees and c and l are the concentration and pathlength, respectively. Usually concentration is given as the solution molarity and the path-length is measured in centimeters.

1.4.1 Kramers-Kronig Relations

In 1926 Kronig and Kramers showed that there is a relationship between the real and imaginary parts of the index of refraction. Naturally, because the Kramers relations apply to the index of refraction they also apply to circular dichroism and optical rotation. This relationship was first realized by Moscowitz.[14] Following that work, the relationships have been applied to calculate ORD and ECD from each other in theoretical and experiment works. The Kronig-kramers relations interconvert between circular dichroism and optical rotatory dispersion but this requires that one spectrum is known at all wavelengths to calculate the other. Practically, this is not feasible and many workers have used the Kronig-Kramer's relations to approximate the ORD from ECD. Without solving exactly, these relations can still help you gauge how the circular dichroism will effect the optical rotation in a qualitative manner. The relationships between the circular dichroism and optical rotation are given as follows:

$$\phi(\omega) = \frac{2}{\pi}\int_0^\infty \frac{\Omega\theta(\Omega)}{\Omega^2 - \omega^2}d\Omega \tag{1.8}$$

$$\theta(\omega) = -\frac{2\omega}{\pi}\int_0^\infty \frac{\phi(\Omega)}{\Omega^2 - \omega^2}d\Omega \tag{1.9}$$

where ϕ is the optical rotation and θ is the circular dichroism. There have been several approaches to interconverting circular dichroism and optical rotation using numerical integration techniques to get around the pole in the integrand.[15;16] I have developed a complementary technique to the ones listed in the cited references. Looking at equations 1.8 and 1.8 it convenient to write them in a form that isolates the pole.

$$\phi(\omega) = \frac{2}{\pi}\left(\int_0^{\omega-\delta} \frac{\Omega\theta(\Omega)}{\Omega^2-\omega^2}d\Omega + \int_{\omega+\delta}^{\infty} \frac{\Omega\theta(\Omega)}{\Omega^2-\omega^2}d\Omega + \int_{\omega-\delta}^{\omega+\delta} \frac{\Omega\theta(\Omega)}{\Omega^2-\omega^2}d\Omega\right) \tag{1.10}$$

$$\theta(\omega) = -\frac{2\omega}{\pi}\left(\int_0^{\omega-\delta} \frac{\phi(\Omega)}{\Omega^2-\omega^2}d\Omega + \int_{\omega+\delta}^{\infty} \frac{\phi(\Omega)}{\Omega^2-\omega^2}d\Omega + \int_{\omega-\delta}^{\omega+\delta} \frac{\phi(\Omega)}{\Omega^2-\omega^2}d\Omega\right) \tag{1.11}$$

The first two terms in 1.10 and 1.11 are easily calculated using numerical quadrature. To deal with the integral containing the pole numerically we begin by further breaking down that portion.

$$\int_{\omega-\delta}^{\omega+\delta} \frac{\Omega\theta(\Omega)}{\Omega^2-\omega^2}d\Omega = \lim_{\varepsilon\to 0}\left(\int_{\omega-\delta}^{\omega-\varepsilon} \frac{\Omega\theta(\Omega)}{\Omega^2-\omega^2}d\Omega + \int_{\omega+\varepsilon}^{\omega+\delta} \frac{\Omega\theta(\Omega)}{\Omega^2-\omega^2}d\Omega\right) \tag{1.12}$$

$$\int_{\omega-\delta}^{\omega+\delta} \frac{\phi(\Omega)}{\Omega^2-\omega^2}d\Omega = \lim_{\varepsilon\to 0}\left(\int_{\omega-\delta}^{\omega-\varepsilon} \frac{\phi(\Omega)}{\Omega^2-\omega^2}d\Omega + \int_{\omega+\varepsilon}^{\omega+\delta} \frac{\phi(\Omega)}{\Omega^2-\omega^2}d\Omega\right) \tag{1.13}$$

These terms can be simplified further by making the subsitution $\Omega = \frac{\omega^2}{y}$ into one of the integrals in equations 1.12 and 1.13. Making this substitution allows us to modify the integrand in such a way that it has a limit at ω. Dropping the limit notation for succintness, an approximate integral for the region surrounding the pole is given in the equation below.

$$\int_{\frac{\omega^2}{\omega-\delta}}^{\frac{\omega^2}{\omega-\varepsilon}} \frac{\omega^2\theta(\frac{\omega}{y})}{y(y^2-\omega^2)}dy + \int_{\omega+\varepsilon}^{\omega+\delta} \frac{\Omega\theta(\Omega)}{\Omega^2-\omega^2}dy \approx \int_{\omega+\varepsilon}^{\omega+\delta} \frac{z^2\theta(z)}{z(z^2-\omega^2)} - \frac{\omega^2\theta(\frac{\omega}{z})}{z(z^2-\omega^2)}dz \tag{1.14}$$

$$\int_{\frac{\omega^2}{\omega-\delta}}^{\frac{\omega^2}{\omega-\varepsilon}} \frac{\phi(\frac{\omega}{y})}{y^2-\omega^2}dy + \int_{\omega+\varepsilon}^{\omega+\delta} \frac{\phi(y)}{\Omega^2-\omega^2}dy \approx \int_{\omega+\varepsilon}^{\omega+\delta} \left(\frac{\phi(z)}{z^2-\omega^2} - \frac{\phi(\frac{\omega}{z})}{z^2-\omega^2}\right)dz \tag{1.15}$$

This approximation is formed by expanding the limits and taking the first order term of the binomial expansion assuming that ω is much greater than δ and ε. Because the limit of the integrand is no longer ∞ when at ω this permits numeric evaluation of the region using a

trapezoidal rule as the following.

$$\frac{1}{2}\delta\left(\frac{(\omega+\delta)^2\theta(\omega+\delta)-\omega^2\theta\left(\frac{\omega^2}{\omega+\delta}\right)}{(\omega+\delta)(\delta^2+2\omega\delta)}+\frac{\theta(\omega)}{\omega}+\frac{d\theta}{d\omega}\right) \tag{1.16}$$

$$\frac{1}{2}\delta\left(\frac{\phi(\omega+\delta)-\phi\left(\frac{\omega^2}{\omega+\delta}\right)}{\delta^2+2\delta\omega}+\frac{1}{\omega}\frac{d\phi}{d\omega}\right) \tag{1.17}$$

This is one of many approaches used for numeric evaluation of the Kronig-Kramers relations. This was primarily used to ascertain expected qualitative features in the ORD from theoretical and experimental ECD.

1.4.2 Quantum Mechanicals of Optical rotation and Circular Dichroism

"The plight of optical activity is even worse, where not one, but two transition moments must be found." Eyring-Caldwell[2]

The Hamiltonian for an electron in a radiation field is given by Equation 1.18.

$$H=\frac{1}{2m}(-ih\nabla-\frac{e}{c}A)^2+e\phi. \tag{1.18}$$

The A^2 term is ignored because it is assumed that the intensity of the radiation is weak. In the analysis of the interaction of electromagnetic radiation with a molecule the total hamiltonian is given by $H=\frac{ie\hbar}{mc}\mathbf{A}\cdot\nabla+H_0$ where H_0 is the standard molecular hamiltonian(See the book by Caldwell and Eyring). The basis of the quantum theory of optical activity in isotropic media was introduced by Rosenfeld who derived the tensor β given in Equation 1.19 from time dependent perturbation theory.

$$\beta_n=\frac{c}{3\pi h}\sum_{m\neq n}\frac{\Im(\langle n|\boldsymbol{\mu}|m\rangle\cdot\langle n|\mathbf{m}|m\rangle)}{\nu_{nm}^2-\nu^2} \tag{1.19}$$

In the above equation, n and m are quantum states and ν_{nm} is the frequency difference between states n and m. The vectors μ and $\mathbf{m}$ are the electric and magnetic dipole operators.

$$\boldsymbol{\mu} = \sum_i e\,\mathbf{r_i} \tag{1.20}$$

$$\mathbf{m} = \frac{-i\hbar e}{mc}\sum_i \mathbf{r}\times\nabla \tag{1.21}$$

The ECD and the ORD are fundamentally related to the dot product between the electric dipole and magnetic dipole operator. The rotational strength, the fundamental quantity for optical activity, is given in Equation 1.22.

$$R^{1\to 2} = \Im(\langle 1|\boldsymbol{\mu}|2\rangle\cdot\langle 2|\mathbf{m}|1\rangle) \tag{1.22}$$

This requirement that the transition electric and magnetic dipole moment have a non-zero dot product explains why only certain point groups are acceptable. The relationship betweent the circular dichroism and the rotational strength assuming a gaussian lineshape is given by 5.2 The relationship between the rotational strength and the optical rotatory dispersion is given by

$$\theta = -\frac{72\cdot 10^6\,\hbar\,N_A\,2\omega^2 6\pi^2}{c^3 m_e^2 M}\left(\frac{1}{3}Tr(\beta)\right) \tag{1.23}$$

Where the units are θ are degrees ml decimeters^{-1} g^{-1}. These are the typical units used in the literature for reporting optical rotatory dispersion measurements. E.U. Condon showed that the difference in the Einstein B coefficients for a chiral molecule is given by Equation 1.24.[17]

$$B_l - B_r = \frac{2}{3\pi\hbar^2}R^{1\to 2} \tag{1.24}$$

1.4.3 The Quest for Absolute Configuration from Circular Dichroism and Optical Rotatory Dispersion

One of the most important applications of chiral sensitive spectroscopy is the determination of absolute configuration. The absolute configuration of a chiral molecule is whether the molecule is R and S. In general the R and S designation of molecules does not correlate with

the results of any spectroscopic method. Therefore, it is important to be able to make an accurate estimate of the optical activity of a chiral molecule. In the period before modern computers, determinations of absolute configuration relied on sector rules. For example, the octant rule for saturated ketones has been used in some cases to determine the sign of the $n \rightarrow \pi^{\star}$ transition of the electronic circular dichroism[18]. The sign is determined by dividing space into 8 different cartesian regions and the position of the chiral perturber relative the the carbonyl determines the sign.[19] Similar rules have been developed for different classes of ketones like α, β unsaturated ketones which are relevant to carvone.[20] These rules allowed one to establish the absolute configuration of a chiral ketone. The challenge with octant rules is that they are highly specific and become hard to apply with increasing complexity.[2] The use of these octant rules has been outmoded with the introduction of the quantum chemistry software with the capability to calculate the optical rotatory dispersion. Numerous studies exist that use high level quantum chemistry calculations of optical rotation, vibrational and electronic circular dichroism to establish absolute configuration.[21]

1.4.4 Optical Rotatory Dispersion and Vibrational Corrections

One of the most important assumptions for quantum chemistry is the Born-Oppenhiemer approximation. Because the electrons move much faster than the nuclei, calculations usually consider the positions of the nuclei to be fixed and calculate the electronic wavefunction with the nuclei positions as a parameter. The total energy is minimized as a function of the nuclear coordinates. This minimization gives a local minimum, refered to a stationary state. In the ground state of a molecule the nuclear positions are not fixed. It is most often the case that the nuclear motions about the equilibrium geometry are modeled with a coupled harmonic oscillator model. The results of this treatment yield a complete set of coordinates known as the normal mode coordinates. When comparing ORD to experiment, the sign of the ORD is considered a litmus test for the accuracy of the calculation. In some cases it has been shown that it is nessecary to correct the ORD for nuclear coordinate motion. A more detailed discussion of the literature related to this topic is given in Chapter 2. The goal here is to discuss the methodology used to calculate the vibrational corrections to the

ORD. First, since the electronic wavefunction is a function of the normal mode coordinates, it follows that the optical rotatory dispersion will follow suit. I begin by expanding the optical rotatory dispersion α in terms of the ground state normal mode coordinates about the equibrilium geometry.

$$\alpha = \alpha(q_0) + \sum \left.\frac{\partial \alpha}{\partial q_i}\right|_{q_0} (q_i) + \sum \left.\frac{\partial^2 \alpha}{\partial q_i q_j}\right|_{q_0} (q_i)(q_j)... \tag{1.25}$$

In quantum mechanics the expected result of an operator is given by its expectation value. In this derivation, the harmonic approximation is being used. This implies that the normal mode coordinates are orthogonal. Taking the expectation value of α gives Equation 1.26

$$\langle \alpha \rangle = \alpha(q_0) + \sum_i \left.\frac{\partial^2 \alpha}{\partial q_i^2}\right|_{q_0} \langle Q_i | q_i^2 | Q_i \rangle \tag{1.26}$$

where Q is the vibrational wavefunction. All terms that are linear in q_i go to zero because of parity. At room temperature the excited vibrational states have a non-zero population determined by a boltzmann distribution. To account for this the expectation value of q_i^2 as a function of temperature needs to be taken into account. The expectation value of the q_i^2 is easily calculated from the raising and lowering operators. The thermally weighted expectation value of q_i^2 for each vibrational quantum state is given by Equation 1.28.

$$\langle \alpha \rangle = \alpha(q_0) + \sum_i \frac{\partial^2 \alpha}{\partial q_i^2} \frac{\hbar}{2 m_i \omega_i} \frac{\sum_n (2n+1) e^{-\beta n \hbar \omega_i}}{\sum_n e^{-\beta n \hbar \omega_i}} \tag{1.27}$$

Equation 1.28 can be simplified to its final version by putting in the values obtained from the sums.

$$\langle \alpha \rangle = \alpha(q_0) + \sum_i \frac{\partial^2 \alpha}{\partial q_i^2} \frac{\hbar}{2 m_i \omega_i} \coth\left(\frac{\beta \hbar \omega_i}{2}\right) \tag{1.28}$$

This does not take into account the anharmonic effects associated with the shortcomings of the harmonic model. To evaluate the vibrational corrections I wrote a python script that takes a Gaussian output file with the normal mode coordinates and writes the nessecary output files required to run it on University of Tennessee's Newton cluster that is freely available upon request.

1.4.5 Literature Notation and Definitions Related to Optical Activity

There are several methods that are used to denote enantiomers of molecules. The simplest method uses l and d, which stand for levorotatory and dextrorotatory , uses the direction of rotation to distinguish the enantiomers. This has no bearing on the structure of the molecule. Levorotatory molecules rotate light counterclockwise when seen by an observer looking in the direction of the light and vice versa for Dextrorotatory. The "L " and "D " system uses the sodium D line rotation of the chiral amino acid precursor glyceraldehyde as a reference. The "L " amino acids are derived from the (S)-$(+)$-glyceraldehyde and vice versa. The R and S convention uses the rules to establish absolute configuration of the molecule and can be found in any organic text book. The "+" means that the sample rotates the polarization ccw when looking toward the light source and vice-versa for the "-" symbol. In this thesis the IUPAC preference using R and S will be used.

Chapter 2

Solvent and Vibrational Effects on the Optical Rotatory Dispersion of Carvone

Solute-solvent interactions are of central importance to chemistry. Numerous studies have focused on the effects of solvents on chemical reactions rates, NMR, UV-Vis, Raman, IR spectroscopy, CD, and ORD. A common approach taken to quantify the effects of solvation is to correlate the properties of solvents (dipole moment, polarizibility, hydrogen bond donation and acceptance, pH, dielectric constant, etc.) with trends in experimental observations.[22] This study focuses on the effects of solvent on the ORD and CD of the carvone molecule and the computational modeling of the ORD and CD of carvone in both the gas phase and in solution. The carvone molecule shown in Figure 2.1 is a chiral terpene which exists in two enantiomeric forms, (*S*)-(+)-carvone and (*R*)-(-)-carvone. Both enantiomers are natural products: (*S*)-(+)-carvone is a major component in the oil from caraway seeds and (*R*)-(-)-carvone is present in spearmint oil. As such, both enantiomers are heavily utilized in the food industry. Ballard *et al.*[23] and Suga *et al.*[24] studied the conformational flexibility of carvone using temperature dependent circular dichroism. Ballard *et al.*[23] reported an enthalpy difference of 2.0 kcal/mol between the axial and the lower energy equatorial structures of carvone (see Figure 2.1). The conformational properties of carvone have also been studied

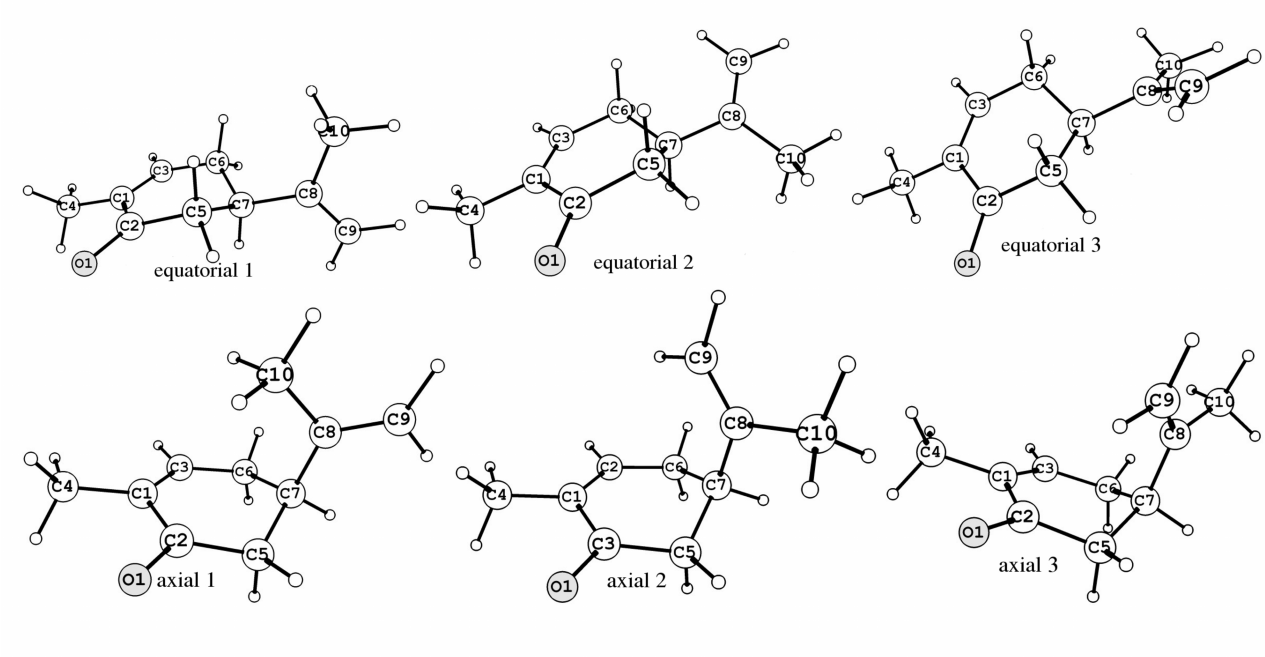

Figure 2.1: The six stable conformers of carvone.

using laser jet spectroscopy[25] and gas electron diffraction.[26] Eqawa *et al.*[25] determined that the "equatorial 1" conformer was $62 \pm 18\%$ abundant at 401K while the combination of the 2nd and 3rd equatorial conformers were the second most abundant structures. Mineyama *et al.*[26] measured the 1+1 REMPI spectrum of carvone but did not attempt to quantify the abundance of the conformers. It was concluded that the gas phase carvone was primarily composed of the three equatorial conformers distinguished by rotation about the C7−C8 bond shown in Figure 2.1. Jansík *et al.*[27] studied the conformational flexibility and the magnetochiral birefringence computationally. The populations calculated in their study are similar to the results presented in Table 2.5 of this article. The slight differences between this article and their results can likely be ascribed to differences in basis set. The nomenclature for the conformers of carvone used in this article is the same as that used by Eqawa *et. al*[25] and Mineyama *et. al.*[26] A large variety of solvent parameters[22;28–30] have been used to quantify the effects of solvation. These include both intrinsic parameters such as solvent dipole moment and empirical parameters like solvochromatic shifts in the UV/Vis absorption of a chosen reference molecule. The E_T^N values are a normalized unitless empirical parameter calculated using Equation 2.1 from the solvochromatic shift

Table 2.1: Solvent parameters used in this study.

solvent	E_T^N	ϵ	n(D)[a]	μ(Debye)	α	β	π^*
1-octanol	0.54	10.30	1.43	2.00	0.77	0.81	0.40
2-butanol	0.51	16.56	1.40	1.65	0.69	0.80	0.40
2-butanone	0.33	18.11	1.38	2.78	0.06	0.48	0.67
acetone	0.35	20.56	1.36	2.88	0.08	0.48	0.62
acetonitrile	0.46	35.94	1.34	3.44	0.19	0.40	0.66
benzene	0.11	2.27[31]	1.50[31]	0.00	0.00	0.10	0.55
benzonitrile	0.33	25.20	1.53	4.28	0.00	0.37	0.88
butanal	na	na	1.38	3.22	0.00	0.40	0.65
cyclohexane	0.01	2.02	1.43	0.00	0.00	0.00	0.00
cyclopentanone	0.27	14.45[b]	1.44	3.28	0.00	0.52	0.76
DMSO	0.44	46.45	1.48	4.10	0.00	0.76	1.00
ethanol	0.65	24.55	1.36	1.65	0.86	0.75	0.54
methanol	0.76	32.66	1.33	2.88	0.98	0.66	0.60
nitrobenzene	0.32	34.78	1.56	4.22	0.00	0.39	1.01
nitroethane	0.40	28.96	1.39	3.65	0.00	0.25	0.80
propionitrile	0.40	28.26	1.37	4.00	0.00	0.37	0.64
toluene	0.10	2.38[31]	1.49	0.30	0.00	0.11	0.49
valeronitrile	0.36	20.03	1.40	4.12	0.00	na	0.63

a. Index of refraction at 589 nm.
b. measured at 20°C

of the strongest UV/Vis absorption band of a pyridinium (N)-phenolate betaine dye.[22] The reference solvents chosen for the E_T^N values are water and tetramethylsilane(TMS).

$$E_T^N = \frac{\nu_{solvent} - \nu_{TMS}}{\nu_{water} - \nu_{TMS}} \tag{2.1}$$

In Equation 2.1 $\nu_{solvent}$ is the frequency of the strongest electronic absorption band for the pyridinium dye in the chosen solvent. The Kamlet-Taft parameters characterize a solvent with three parameters α, β, and $\pi^\star$ (Ref. Reichardt).

$$[\alpha]_\lambda^T = a\alpha + b\beta + c\pi^\star + [\alpha]_{cyclo,\lambda}^T \tag{2.2}$$

The term α represents the solvent's propensity toward hydrogen bond donation. The term β represents the tendency of a solvent to accept a hydrogen bond and $\pi^\star$ is a term that

accounts for the effects of solvent dipole moment and polarizability. The term $[\alpha]^{T}_{cyclo,\lambda}$ is the value of the specific rotation at temperature T and wavelength λ in cyclohexane, which is taken to be the least perturbative of the solvents. In Equation 2.2 the term a quantifies the hydrogen bond acceptance of the solute. For example, if the solute readily accepts a hydrogen bond then this parameter will be larger in magnitude. The parameter b quantifies the importance of hydrogen bond donation of the solute and the parameter c quantifies the importance of the dipolarity/polarizability term for the solute being studied. The terms a, b, and c are determined through a multivarible linear regression. Once a, b, and c are known for the measured property of the solute, then the value of the solute property being studied can be estimated for all other solvents provided that their Kamlet-Taft parameters are known. The Kamlet-Taft parameters have been applied with mixed success to NMR[32], UV/Vis[33], IR[34], and ORD[29]. The carvone molecule has a hydrogen bond acceptor site, as well, and possesses a dipole moment due to the oxygen double bond attached to the cyclohexane ring. The calculated dipole moment (B3LYP/aug-cc-pVDZ) in the gas phase for each of the three equatorial conformers are 3.6, 3.2, and 3.8 D for the equatorial conformer 1-3, respectively (see Figure 2.1). The Kamlet-Taft parameters are evaluated to determine their applicability to the conformationally flexible carvone molecule.

Quantum chemical calculations have developed rapidly over the past decade but calculations of ORD remain a challenge for electronic structure theory[21;35–39]. While excellent results have been obtained in most cases when comparing between advanced coupled cluster methods and gas-phase experimental data,[38;40] agreement with liquid-phase results is much worse.[38;41] Indeed, in some cases, it has been demonstrated that agreement with experiment occurs because of a fortuitous cancellation of errors,[38;42] and calculations of ORD have been known to produce results that differ in sign with that of the experimental data even at high levels of theory. Furthermore, even zero-point vibrational corrections have been found to be important in many cases.[40;43–47] For example, calculations carried out using coupled cluster theory with triples excitations produce the incorrect sign when compared to gas-phase values[48;49] for (S)-propylene oxide (methyloxirane)[43], unless vibrational corrections are included as well.[45] The incorporation of such effects, not to

mention the additional complexities of conformational flexibility[50–53] and solvation, is a challenging task.

Implicit solvation models are typically based upon the work of Kirkwood[54], Born[55], and Onsager[56], and vary primarily in the manner in which the electrostatic and non-electrostatic forces are treated and the manner in which the solvent cavity is formed. The electrostatic interactions are the result of the charge distribution of the solute and how it interacts with the polarizable continuum. For example, the molecular dipole can be utilized to polarize the solvent reaction field. Likewise a multipole expansion of the solute charge distribution centered on an atom or bond can be used similarly. The cavity that forms the solvent exclusion region can be formed by employing simple atomic centered spheres, overlapping van der Waals surfaces, or more complex elliptical shapes. The non-electrostatic forces describe other effects such as the cavitation energy , dispersion forces, and repulsion forces. The polarizable continuum model (PCM) places the solute charge distribution inside an infinite polarizable medium with the dielectric constant ϵ equal to that of the chosen solvent. The solvent reaction field responds to the solute charge distribution and then the solute charge distribution is modified by the solvent reaction field. This model has been successfully applied to a wide variety of problems.[57] However, PCM-based approaches have been useful for ORD computations only in select cases. For example, Mennucci and coworkers combined DFT calculations of specific rotations with their implicit PCM, and reported sodium D-line rotations in reasonable agreement with corresponding measurements in cyclohexane, acetone, methanol, and acetonitrile, but significant errors appeared for others, such as CCl_4, benzene, and $CHCl_3$.[58] Given the inherent limitations in their model, they attributed the discrepancies to non-electrostatic effects, and role of the functional (B3LYP) in the errors they observed remains unknown. Pecul *et al.*[59] reported analogous DFT-based PCM studies of electronic circular dichroism in 2005 for methyloxirane, camphor, norbornenone, and fenchone. They found that the reliability of their predictions depended not only on the shortcomings of available exchange-correlation functionals, but also on the type of transition in question, with Rydberg- type excitations and the $n \rightarrow \pi^*$ transitions of norcamphor and norbornenone were especially problematic, perhaps due to specific solute-solvent interactions.

2.1 Computational methods

The six stable conformers of carvone shown in Figure 2.1 were optimized using DFT/B3LYP[60–62] with the 6-311G(d,p) basis set and the higher accuracy G3 method[63] as implemented in Gaussian03.[64] The G3 and G3MP2 method perform an intial Hartree-Fock/6-31G(d) optimization and frequency calculation to determine the zero point vibrational energy correction. This is followed by a MP2(full)/6-31(d) geometry optimization for both the G3 and the G3MP2 method. Specific rotations for each conformer were computed using linear-response theory in conjunction with the coupled cluster singles and doubles (CCSD) approach,[41;42;65–67] a second-order approximation to CCSD referred to as CC2,[68] and a time-dependent DFT (TD-DFT) formulation[69] with the B3LYP functional.[70] To ensure origin independence of the computed rotations, gauge-including atomic orbitals (GIAOs)[70–72] were employed with the B3LYP method, and the modified velocity representation of the electric dipole operator was used with the CCSD and CC2 methods.[73] The 1s core orbitals for all carbon and oxygen atoms were held frozen in the coupled cluster computations. Optical rotations were computed using the correlation-consistent basis sets of Dunning and co-workers, including one or two sets of diffuse functions as necessary.[74;75] For simplicitly, the names of the Dunning basis sets will be abbreviated as follows: DZ = cc-pVDZ, aDZ = aug-cc-pVDZ, aTZ = aug-cc-pVTZ, daDZ= d-aug-cc-pVDZ, aDZ/DZ = aug-cc-pVDZ on carbon and oxygen atoms plus cc-pVDZ on hydrogens, aT(D)Z/DZ = aug-cc-pVTZ on atoms involved in double bonds plus aug-cc-pVDZ on all other carbons plus cc-pVDZ on hydrogens, (d)aDZ/DZ = d-aug-cc-pVDZ on atoms involved in double bonds plus aug-cc-pVDZ all other carbons plus cc-pVDZ on hydrogens. The calculations demonstrate the existence of six stable conformers, in agreement with Harding *et al.* and Jansík *et al.*[27;76] Boltzmann populations were computed using Gibbs free energies from both B3LYP/6-311G(d,p) and G3 approaches, within the ideal-gas, rigid-rotor, and harmonic-vibration approximations.[77;78] (These populations will be referred to hereafter as "B3LYP" and "G3", respectively.) Contributions from temperature-dependent (300 K) molecular vibrations were computed for each conformer following the approach described by Wiberg *et al.*,[50] using the B3LYP/6-311G(d,p) harmonic force field. Displacements along each normal mode were computed using stepsizes of 0.05 (cf. Ref. 50). In order to obtain stability of the numerical

differentiation, the equilibrium geometries were converged to a root-mean-square force of $1 \times 10^{-6}\ E_h/a_0$, with pruned numerical integration grids of at least 99 radial shells and 509 angular points per shell. All B3LYP computations were carried out using Gaussian03.[64] and Gaussian09,[79] while all coupled cluster computations were carried out using PSI3.[80] The PCM model calculations utilized the integral equation formulation using UAO (Simple United Atom Topological Model) to construct the solvent exclusion region as implemented in Gaussian03.[64]. The structure of the six conformers were optimized in each of the solvents listed in Table 2.10 using the PCM model coupled with B3LYP/aDZ method and the higher accuracy G3MP2 method.[81] The goal with the usage of the G3MP2 calculations is to obtain more accurate Gibbs free energies which influence the relative populations drastically. The geometries obtained from optimization with B3LYP/aDZ with the PCM model were used to calculate the optical rotation at 589 nm, 578 nm, 546 nm and 436 nm. A Boltzmann averaged OR using the Gibbs free energy obtained from B3LYP/aDZ and G3MP2 method was calculated at 25°C ("G3MP2 Avg" refers to a boltzmann average in solution using G3MP2 coupled with the PCM model and "B3LYP/aDZ Avg" uses B3LYP/aDZ coupled with the PCM model to calculate Boltzmann averages). As with the gas phase calculations, the populations are determined within the ideal gas, rigid rotor, and harmonic- vibrational approximation with additional corrections for the electrostatic, cavitation, dispersion and repulsion interactions in solution. All solution phase calculations were performed on (*S*)-(+)-carvone.

2.2 Experimental Methods

2.2.1 Concentration-Dependent ORD

(*R*)-(-)-carvone and (*S*)-(+)-carvone were obtained from Alfa Aesar with a stated purity of 98% and 96%. These samples of carvone were used for all the experiments in this paper. The quoted specific rotation of the samples for the samples were 60.8 deg dm^{-1} $(g/mL)^{-1}$and 60.2 deg dm^{-1} $(g/mL)^{-1}$. Each solution was prepared without purification using seven or eight different concentrations ranging from 1.28×10^{-3} g/mL to 3.85×10^{-2} g/mL. Data for each wavelength and concentration were measured five times and the average

of these five measurements was used to determine the ORD at infinite dilution in order to minimize the effect of solute-solute interactions.[82–84] All the measurements of optical rotation in this article except for the neat value for carvone, are the result of an extrapolation to infinite dilution. Optical rotations were measured at 22° to 25° C using a 10 cm path length at 589 nm, 578 nm, 546 nm, and 436 nm with a Perkin Elmer model 241 polarimeter. With this apparatus the typical fluctuation in the measured angle was 0.002°. The extrapolated intrinsic rotation was determined by fitting the absolute rotation to a fourth-order polynomial, using the constraint that the rotation must decay to zero at zero concentration. The error bars for each measurement are the fitting parameter error bars using a scaled Levenberg-Marquardt algorithm for the fitting. The ORD curves obtained from the extrapolation method were compared to the Drude model to check for consistency. All the parameters used to fit the Drude model to the ORD data are given in Table 2.12.

2.2.2 Gas and solution phase CD

The solution phase CD was measured using a 1mm path-length in an Aviv Biomedical model 202 CD spectrometer. The gas-phase CD was measured using a 1cm path-length in the same spectrometer with a small amount of sample placed in the bottom of the sample container. Various concentrations were used when preparing the solutions. The temperature of the gas-phase measurements were varied from 20°C to 60°C. The gas-phase measurement is unreliable below 250 nm because of the absorption of the quartz cell. The sample container was monitored for condensation on the walls. No obvious condensation was observed but the possibility of a thin layer being deposited on the surface cannot be ruled out, but this should not affect the room-temperature data. The data were taken with four seconds of averaging per data point at 0.5 nm steps for both solution and gas phase CD.

2.3 Results and discussion

2.3.1 Experimental ORD

The chemical literature is replete with efforts to correlate properties such as ORD and CD with various properties of solvents, both pure and mixtures. For example, in a series of

Table 2.2: Sample concentrations used in the CD measurements.

Solvent	Concentration(g/mL)
2-butanol(racemic)	0.10
2-butanone	0.12
acetone	0.04
acetonitrile	0.11
benzene	0.12
2-butanal	0.13
cyclohexane	0.03
cyclopentanone	0.13
ethanol	0.19
propionitrile	0.08
valeronitrile	0.05

papers in the 1930s, Rule and co-workers studied the effects of solvent polarity on the specific rotation of several chiral solutes, include, for example 1-menthyl methyl naphthalate,[85] and found that for solvents of the same type a rough approximation to a smooth curve is obtained when rotatory powers are plotted against dipole moments." However, other studies from the same group found the relationship between the dipole moment of the solvent and the ORD of the solute to be erratic, such as for methylentartaric acid.[86]

In 1970, Kumata *et al.*[87] considered a number of solvent parameters, including dipole moment, Onsager dielectric function,

$$f(\epsilon) = \frac{\epsilon - 1}{2\epsilon + 1} \tag{2.3}$$

as well as the $E_T(30)$ parameter, which is defined as the excitation energy corresponding to the maximum absorption of a standard dye in a given solvent.[22] Using propylene oxide (methyloxirane) as a test case, they attempted to correlate such properties with the rotivity, Ω, which is the specific rotation modulated by the Lorentz solvent factor,

$$3\Omega = \frac{3}{n^2 + 2}[\alpha] \tag{2.4}$$

where n is the index of refraction of the solvent. While they did find reasonable correlation between Ω and solvent polarity, the relationship with other parameters was considered "poor," apart from indicating "a general trend."

More recently, Wiberg *et al.* studied the ORD of (S)-2-chloropropionitrile in different solvents,[88] and compared their measured rotations to the corresponding Onsager reaction field values. While most solvents exhibited reasonable correlation between the two, the measured rotation in benzene fell far below that of the other solvents, and the extrapolated ($\epsilon = 1$) gas-phase value of -21 deg dm^{-1} (g/mL)$^{-1}$ was nearly a factor of three smaller than that measured via cavity ring-down polarimetry at -8 deg dm^{-1} (g/mL)$^{-1}$. In 2006 Fischer *et al.*[29] correlated the extrapolated ORD of 3-methylbenzylamine with the various solvent parameters and the Kamlet-Taft parameters. 3-methylbenzylamine was chosen because it both donates and accepts hydrogen bonds. There was no strong correlation for any of the chosen solvent parameters in their study, and they reported an R^2 value of 0.667 when comparing experimental data to Kamlet-Taft parameters.

Measurements of the ORD for (S)-(+)-carvone at 436 nm, 546 nm, 578 nm, and 589 nm, dissolved in 17 different solvents are summarized in Table 2.3, and the ORD is seen to fit well with the Drude model as shown in Figure 2.2, regardless of solvent. This fitting

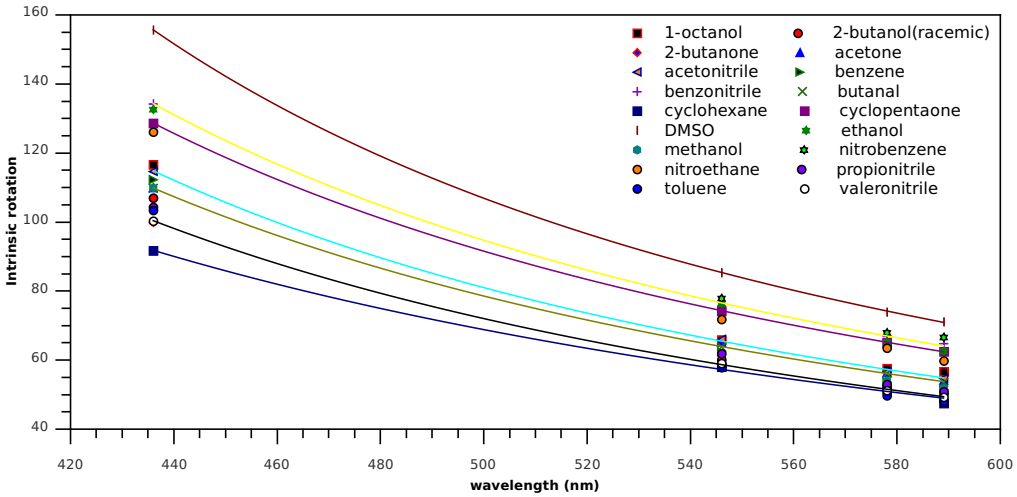

Figure 2.2: The ORD of S-(+)-carvone in 17 different solvents fit to a one parameter Drude model. For clarity some of the Drude model fits have been omitted but the parameters for those fits are included in Table 2.12

Table 2.3: Measured ORD of (*S*)-(+)-carvone (deg dm^{-1} (g/mL)$^{-1}$) at 4 wavelengths.

Solvent	436 nm	546 nm	578 nm	589 nm
1-octanol	116.7 ± 11.1	66.0 ± 5.8	57.6 ± 5.0	56.8 ± 4.8
2-butanol (racemic)	107.0 ± 13.9	60.1 ± 7.9	52.6 ± 6.8	50.4 ± 6.4
2-butanone	100.9 ± 5.3	59.0 ± 3.3	52.0 ± 3.0	49.8 ± 2.8
acetone	110.0 ± 5.1	65.2 ± 2.8	56.4 ± 2.8	54.2 ± 2.6
acetonitrile	114.8 ± 9.4	66.2 ± 5.3	56.8 ± 4.8	54.8 ± 4.8
benzene	112.4 ± 13.6	62.5 ± 7.9	53.8 ± 7.4	51.6 ± 7.0
benzonitrile	134.4 ± 7.0	75.7 ± 3.8	67.1 ± 3.4	64.9 ± 2.8
butanal	109.9 ± 8.6	64.0 ± 5.0	56.2 ± 4.7	53.7 ± 4.1
cyclohexane	91.7 ± 7.9	58.1 ± 5.9	51.6 ± 4.4	47.6 ± 5.8
cyclopentanone	128.7 ± 8.9	74.3 ± 5.3	65.2 ± 4.4	62.5 ± 4.6
DMSO	155.7 ± 12.1	85.4 ± 6.7	74.0 ± 5.4	71.1 ± 5.3
ethanol	132.7 ± 14.3	76.5 ± 8.5	65.3 ± 7.3	62.7 ± 6.8
methanol	110.0 ± 4.4	61.8 ± 2.8	54.1 ± 2.6	51.8 ± 2.7
nitrobenzene	none	77.9 ± 3.3	68.0 ± 2.6	66.7 ± 2.7
nitroethane	126.2 ± 15.6	71.9 ± 9.1	63.5 ± 8.1	59.8 ± 8.0
propionitrile	104.4 ± 1.7	61.9 ± 1.4	53.0 ± 1.5	51.0 ± 1.5
toluene	103.4 ± 8.5	57.9 ± 4.7	49.7 ± 4.1	48.1 ± 3.9
valeronitrile	100.4 ± 6.2	59.1 ± 3.7	51.3 ± 3.0	49.3 ± 3.0
neat	-	-	-	61.0

opens the question as to what solvent characteristics have the most significant influence on the rotation. Thus, using the values of the ORD at 589 nm, linear fits were made to the solvent parameters of Table 2.1. The resulting correlation was generally weak, and the strongest match ($R^2 = 0.611$) was obtained with the dipolarity/polarizability Kamlet-Taft parameter, π^*. The solvent dipole moment and dielectric constant had correlation values of $R^2 = 0.442$ and $R^2 = 0.455$ while other terms did not have a significant correlation. A least-squares fit of Eq. (2.2) was then carried out using the measured value of the specific rotation in cyclohexane ($[\alpha]^T_{0,\lambda} = 44.69$ deg dm^{-1} (g/mL)$^{-1}$) as a constraint, yielding values of a, b, and c of -9.16, 11.04, and 9.83, respectively, and an average root-mean-squared difference between the experimental and calculated ORD of 4.1 deg dm^{-1} (g/mL)$^{-1}$. The slope of the best fit line and its R^2 value are 0.98 and 0.95 in Figure 2.3 is close to the ideal slope of 1. This fit leads to the tenuous conclusion that the ORD of carvone most strongly depends upon the dipolarity/polarizability of the solvent and that hydrogen bonding has

little effect. This does not agree with the expectation that the terms and a and c should be

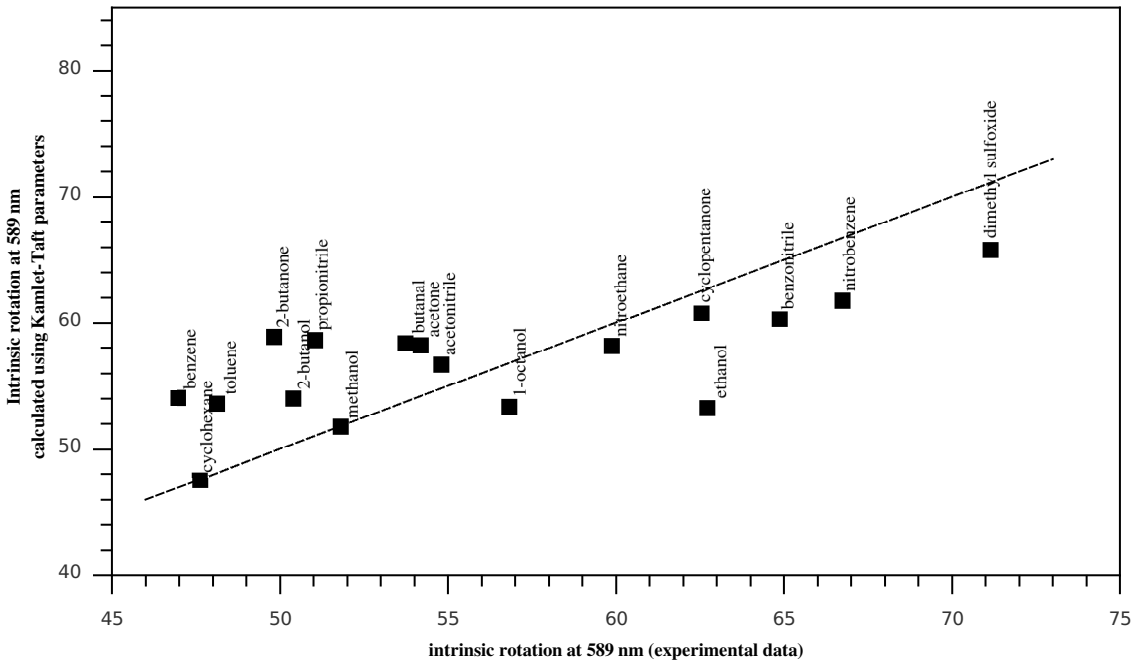

Figure 2.3: Plot of data calculated using the Kamlet-Taft parameters found in this study versus the measured experimental optical rotation at 589 nm. The line represents perfect correlation between the experimental and calculated values.

larger in magnitude . However, the overall correlation between the experimental data and the Kamlet-Taft parameters remains relatively weak (see Figure 2.3), suggesting that other factors — conformer populations, molecule-specific solvent-solute interactions, etc. — must be considered for a more complete understanding.

2.3.2 Experimental gas-phase and solution-phase CD spectra

Measured UV-Vis and CD spectra for (R)-(-)-carvone dissolved in cyclohexane are shown in Figure 2.4. We note that the positive CD vibrational features correlate exactly with the vibrational peaks in the UV-Vis spectrum in the $n \rightarrow \pi^{\star}$ transition, but, most interestingly, the negative CD peaks do not correlate with their UV-Vis counterparts. CD spectra of carvone in 11 different solvents are shown in Figure 2.5, and the sign, width, and positions of the peaks are observed to vary with the choice of solvent. For the ketone solvents, the CD is noisy at short wavelength because of strong solvent absorption. Also, for benzene and

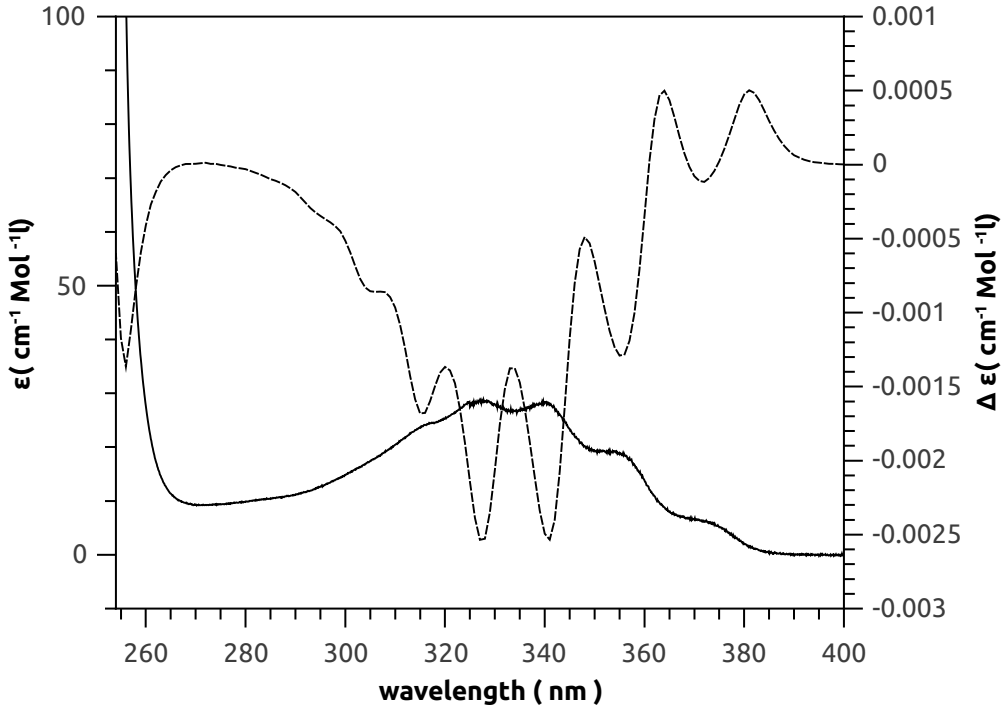

Figure 2.4: Representative CD(dashed line) and UV/vis(solid line) spectrum of (*S*)-carvone in cyclohexane.

valeronitrile, the CD was above the maximum measureable of 0.5 degrees of ellipticity at 320 nm.

It is interesting to note that the relative intensity and sign of vibronic peaks change with choice of solvent around 355 nm. Each of the six conformers will interact with each solvent differently. Therefore, the solvent environment is expected to affect both the conformer populations as well as the rotational strengths of each for different transitions.

The solution phase CD in Figures 2.5 and 2.4 spectra show significant shifting and even sign changes for particular vibronic peaks in the $n \rightarrow \pi^*$ transition region from 300 to 400 nm. The structure seen in the $n \rightarrow \pi^\star$ transition between 400 and 300 nm has been reported previously by Ballard *et al.*[23] who attributed them to vibrational structure due primarily to the carbonyl stretching mode at $\nu \simeq 1200$ cm^{-1}. Our analysis does not support this interpretation because the frequency for the carbonyl stretching mode was calculated to be greater than 1700 cm^{-1} when using B3LYP with both aDZ and 6-311G(*d*,*p*) basis sets. Instead, the vibrational states from 971 cm^{-1} to 1226 cm^{-1} involving ring deformations,

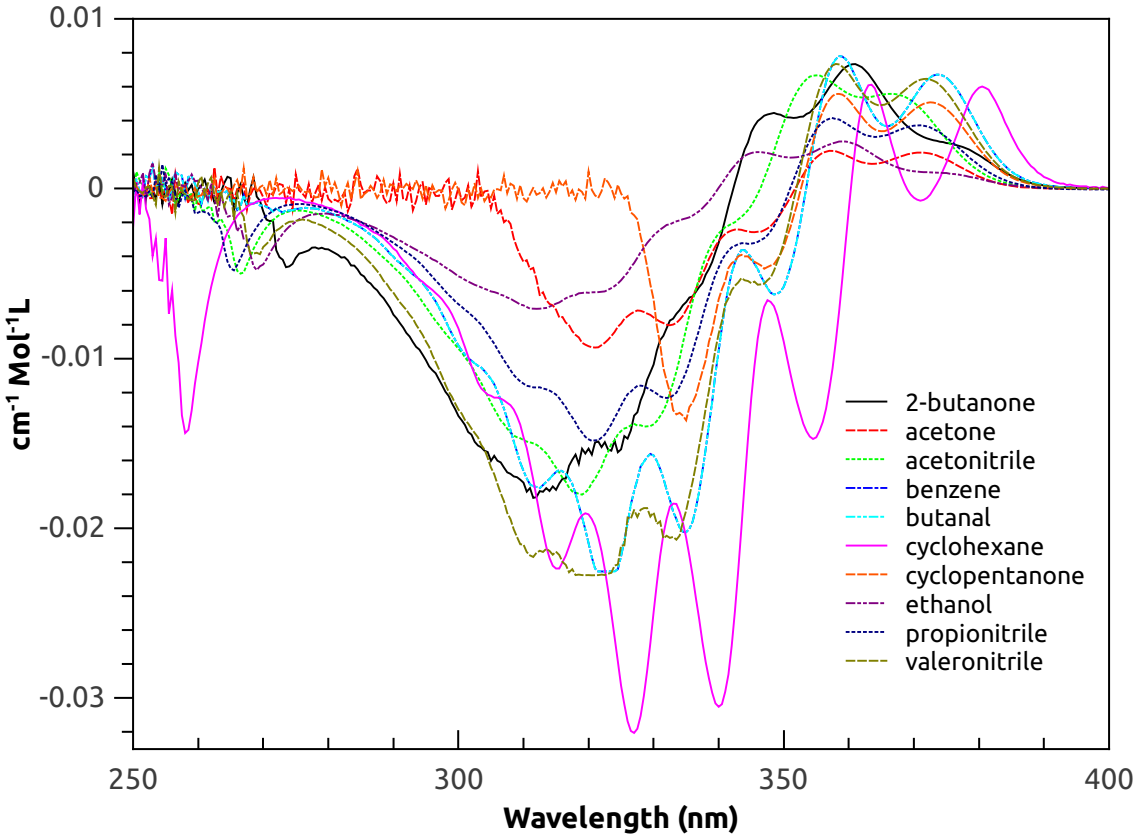

Figure 2.5: CD spectra of (S)-(+)-carvone in various solvents. The acetone and cyclopentanone data sets have large error below 315 nm and 340 nm respectively due to solvent absorption.

propene bending, C−C stretching, and hydrogen bending and rocking are the bands making the largest contribution to the CD in the $n \rightarrow \pi^{\star}$ region. The $n \rightarrow \pi^{\star}$ peaks given in Table 2.4 have spacings of $\simeq 1000\,\mathrm{cm}^{-1}$. It is also interesting to note the red shifting of the onset of the peak located at $\simeq 266\,\mathrm{nm}$ as the temperature increases. This could be a peak broadening effect from the increased pressure or it is also possible that this is the result of more specific gas phase molecular interactions similar to the Franck-Condon solvation principle. Similar vibrational structure is seen in the gas-phase ECD spectrum shown for comparison in Figure 2.6. It is particularly interesting to note that the ECD for carvone in strongly polar molecules such as acetonitrile resembles that for the gas phase or in cyclohexane (cf. Figure 2.4).

Table 2.4: Transition energies of the $n \rightarrow \pi^*$ peaks and corresponding energy differences between adjacent peaks in the (R)-carvone ECD spectrum.

Wavelength (nm)	E (cm^{-1})	ΔE (cm^{-1})
373.5	26773.76	0.00
360.0	27777.78	1004.02
348.0	28735.63	957.85
335.0	29850.75	1115.11
322.5	31007.75	1157.01
311.5	32102.73	1094.98

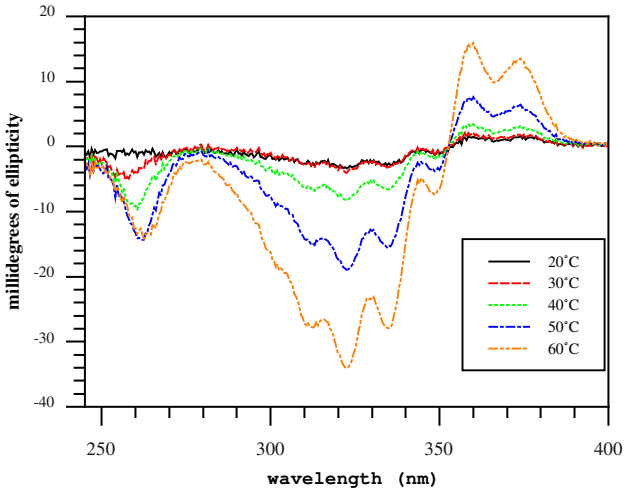

Figure 2.6: Measured gas phase ECD of (S)-(+)-carvone in millidegrees of ellipticity

This is reminiscent of the observation by Vaccaro and co-workers[49] that their gas-phase ORD measurements more closely resemble those measured in polar rather than non-polar solvents. We propose a possible explanation for the non-perturbing nature of certain highly polar molecules on the ORD and ECD of certain chiral molecules. Molecules with dipole moments greater than 2.5 Debye are known to form very diffuse, weakly-bound dipole-bound anions.[89–93] The extra electron exists in a very diffuse orbital at an extended distance from the molecular framework. Klahn *et al.*[94] and Mikulski *et al.*[95] have measured the mobility of excess electrons in CH_3CN (dipole moment = 3.925 Debye) and HCN (dipole moment = 2.985 Debye) and found a strong gas density dependence of the "zero-field" density-normalized mobility (μn). Both CH_3CN[89] and HCN[96] are known to form dipole

bound anions. In order to rationalize this anomalous effect they proposed a transport process in which short-lived dipole-bound anions (lifetime $\geq$ 12 ps) as quasilocalized states are produced and electrons "hop" from one dipole to another. It is possible that a similar situation can exist in solution in which the excited electron in the excitation of carvone enters into a dipole-bound quasi-stationary state of the polar solvent. The excess electron is proposed to rapidly "jump" from one surrounding dipole to the next with little scattering effects. Thus, the solvent provides a type of "band structure" which only slightly perturbs the excited electron through scattering.

2.3.3 Theoretical calculations of ORD

Table 2.5 summarizes the relative energies and corresponding Boltzmann populations at 298 K for each of the six relevant conformers of carvone in the gas phase. Initial computations using the B3LYP/6-311G(d,p) method indicated that the three axial conformers have energies at 8.0 kJ/mol and higher relative to the lowest-energy conformer and thus contribute no more than 1.7% to the average specific rotation at room temperature. However, subsequent computations using both DFT and coupled cluster methods employing only the equatorial conformers yielded specific rotations at 589 nm for (R)-(-)-carvone ranging from 20 to 63 deg dm^{-1} (g/mL)$^{-1}$, i.e. qualitatively incorrect results compared to experiment (cf. Table 2.3 for the (S) enantiomer). Higher level conformer computations using the G3 method produced significantly different energetics, with the three equatorial conformers much closer in energy and two of the axial conformers falling to within 3.4 kJ/mol of the lowest-energy equatorial structure. The corresponding populations at 298 K indicate that the axial conformer cannot be neglected as together they contribute more than 18% of the total average.

Tables 2.8, 2.6, and 2.7 report specific rotations at 589 nm for all six conformers with various basis sets at the B3LYP, CC2, and CCSD levels of theory, respectively. All three methods agree that the individual conformers exhibit substantially different specific rotations, much larger than the absolute value of that measured in solution. (See Table 2.3.) Two of the three lower-energy equatorial conformers give positive rotations for the (R) enantiomer (which has a negative rotation experimentally). On the other hand, two of the

Table 2.5: Computed relative energies and populations of the conformers of carvone.

Conformer	Dihedral Angle[a]		Relative Energy(kJ/mol)		Populations @ 298 K	
	B3LYP/6-311**	G3	B3LYP/6-311G**	G3	B3LYP/6-311**	G3
1(eq)	121.7	126.8	0.0	0.0	0.44	0.30
2(eq)	249.9	251.7	1.3	0.48	0.26	0.25
3(eq)	348.2	348.3	1.3	0.28	0.26	0.27
1(ax)	116.2	115.0	8.9	6.4	0.012	0.022
2(ax)	248.8	241.1	8.7	3.4	0.013	0.075
3(ax)	355.1	4.8	8.0	3.0	0.017	0.090

a. Defined as the C9−C8−C7−C5 angle of Figure 2.1

three axial conformers exhibit negative rotations — another reason that their contribution must be included for accurate computations. The basis-set dependence of the B3LYP results is small; only a few deg dm^{-1} (g/mL)$^{-1}$shift between the aDZ, daDZ, and aTZ basis sets is observed. The basis-set dependence of the CC2 method is somehwat larger, but the use of a triple-zeta basis on the doubly-bonded atoms (aT(D)Z/DZ) tends to produce the opposite shift from the use of extra diffuse functions on the same atoms [(d)aDZ/DZ]. Only one basis set (aDZ/DZ) was possible with the more expensive CCSD method, but some estimate of the impact of higher angular momentum and diffuse functions can be obtained by comparison with the CC2 data. While diffuse functions are requisite, including such functions on the hydrogen atoms makes little difference in this case.

For example, at the CC2 level of theory using the aug-cc-pVDZ basis set on the carbon and oxygen atoms but only cc-pVDZ on the hydrogen atoms yields an optical rotation at 589 nm of 94.6 deg dm^{-1} (g/mL)$^{-1}$, while extending the hydrogen-atom basis set to aug-cc-pVDZ given a rotation of 99.9 deg dm^{-1} (g/mL)$^{-1}$. Two Boltzmann averages are reported in Tables 2.8-2.7, *viz.* those from the B3LYP/6-311G(*d*,*p*) structures and those from the G3 computations, with the latter expected to be significantly more accurate for a gas-phase simulation. For every method, the G3 populations yield a more negative average rotation for the (*R*) enantiomer, because G3 gives greater weight to the equatorial-3 and axial-3 conformers both of which have strong negative rotations. However, for the B3LYP and CCSD methods, the G3 populations still do not produce overall negative specific rotations for (*R*)-(-)-carvone, in disagreement with experiment. At the B3LYP level, the aTZ basis set gives a G3-averaged rotation of 11.8 deg dm^{-1} (g/mL)$^{-1}$, and at the CCSD level, the aDZ/DZ basis

Table 2.6: Specific rotations (in deg dm^{-1} (g/mL)$^{-1}$) at 589 nm computed using CC2 and various basis sets with ($\langle[\alpha]_D\rangle$) and without ($[\alpha]_D$) vibrational corrections from Table 2.9.

	CC2							
	aDZ/DZ		aDZ		aT(D)Z/DZ		(d)aDZ/DZ	
Conformers	$[\alpha]_D$	$\langle[\alpha]_D\rangle$	$[\alpha]_D$	$\langle[\alpha]_D\rangle$	$[\alpha]_D$	$\langle[\alpha]_D\rangle$	$[\alpha]_D$	$\langle[\alpha]_D\rangle$
1 (eq)	94.6	12.5	99.9	17.9	107.6	25.5	99.9	17.8
2 (eq)	203.9	347.6	203.9	347.6	221.9	365.6	203.6	347.3
3 (eq)	-291.6	-410.3	-292.5	-411.2	-297.1	-415.8	-288.4	-407.1
1 (ax)	-97.4	-197.5	-95.3	-195.4	-110.4	-210.5	-98.9	-199.0
2 (ax)	11.7	35.6	22.1	46.1	7.8	31.8	14.2	38.2
3 (ax)	-212.6	-360.0	-214.4	-361.7	-221.6	-368.9	-212.6	-359.9
B3LYP[a]	14.1	-19.2	16.4	-17.0	22.7	-10.7	17.2	-16.1
G3[b]	-19.8	-54.4	-17.8	-52.3	-14.4	-48.9	-17.3	-51.8

a. 'B3LYP Avg' population
b. 'G3 Avg' population

set gives a corresponding 4.4 deg dm^{-1} (g/mL)$^{-1}$. The CC2 method, however, does give negative rotations (with all basis sets used here) when the G3 populations are employed. The CC2/(d)aDZ/DZ level gives an average rotation of -17.3 deg dm^{-1} (g/mL)$^{-1}$. (Note that the B3LYP populations produce the incorrect sign for all methods.)

Application of the vibrational corrections given in Table 2.9 to the equilibrium rotations shifts the Boltzmann averaged results closer to experiment for all methods. The vibrationally averaged rotations are also given in Tables 2.8-2.7. For the B3LYP method, the best result is approximately -24 deg dm^{-1} (g/mL)$^{-1}$ (B3LYP/daDZ), while for CC2 and CCSD the best vibrationally averaged results are ca. -52 and -30 deg dm^{-1} (g/mL)$^{-1}$, respectively, which bracket the the value of $[\alpha]_D$ measured in cyclohexane (see Table 2.3) of -44.7 deg dm^{-1} (g/mL)$^{-1}$(corrected for the choice of enantiomer). Greater accuracy would be obtained from inclusion of anharmonicities as well as the use of CC-based vibrational corrections. We note that the B3LYP and CCSD averages are reasonably close to one another, even though the specific rotations of the individual conformers differ dramatically in some cases. The tendency of B3LYP to overestimate the specific rotation is related to its concomitant

Table 2.7: Specific rotations (in deg dm^{-1} (g/mL)$^{-1}$) at 589 nm computed using CCSD and the aDZ/DZ basis set with ($\langle[\alpha]_D\rangle$) and without ($[\alpha]_D$) vibrational corrections from Table 2.9.

	CCSD	
Conformer	$[\alpha]_D$	$\langle[\alpha]_D\rangle$
1 (eq)	112.7	30.6
2 (eq)	201.4	345.2
3 (eq)	-231.0	-349.7
1 (ax)	-59.4	-159.5
2 (ax)	7.6	31.6
3 (ax)	-183.5	-330.8
B3LYP[a]	38.1	4.7
G3[b]	4.4	-30.2

a. 'B3LYP Avg' population
b. 'G3 Avg' population

tendencies to underestimate excitation energies[42;46] and to overestimate CD rotational strengths.[45]

The theoretical ORD in each solvent listed in Tables 2.10 and 2.11 was calculated using the Gibbs free energy obtained using B3LYP/aDZ and the G3MP2 method coupled with the PCM model. There are two significant differences between the Boltzmann populations obtained in each solvent using B3LYP/aDZ and G3MP2 energies. The solution phase B3LYP/aDZ Avg is dominated by the eq(1) conformer in all solvents while the G3MP2 avg has a more equitable distribution of population between the equatorial conformers. In ethanol the B3LYP/aDZ population of eq(1) conformer is 46% of the total populations compared to a G3MP2 Avg population of 32% . In fact, for the aromatic solvents benzene and toluene, the eq(2) conformer is the most stable structure followed by the eq(1) and eq(3) structures. The Axial conformers make an insignificant contribution to the total ORD with the B3LYP/aDZ Avg. For example, in ethanol the axial conformers make up 4% of the total population and contribute 3.5 deg dm^{-1} (g/mL)$^{-1}$to a total specific rotation of -58.6 deg dm^{-1} (g/mL)$^{-1}$. With the G3MP2 Avg the axial conformers make up 17% percent of the total population and contribute 20 deg dm^{-1} (g/mL)$^{-1}$to the total rotation versus the equatorial contribution of -29 deg dm^{-1} (g/mL)$^{-1}$. The ORD at five wavelengths is

Table 2.8: Specific rotations (in deg dm^{-1} $(g/mL)^{-1}$) of (*R*)-(-)-carvone at 589 nm computed using B3LYP and various basis sets with ($\langle[\alpha]_D\rangle$) and without ($[\alpha]_D$) vibrational corrections from Table 2.9. Populations were determined using the G3 gibbs free energy and B3LYP energies.

B3LYP						
	aDZ		daDZ		aTZ	
Conformer	$[\alpha]_D$	$\langle[\alpha]_D\rangle$	$[\alpha]_D$	$\langle[\alpha]_D\rangle$	$[\alpha]_D$	$\langle[\alpha]_D\rangle$
1 (eq)	191.2	109.1	195.6	113.5	193.2	111.1
2 (eq)	237.4	381.1	240.3	384.0	242.2	385.9
3 (eq)	-340.1	-458.8	-341.1	-459.8	-336.8	-455.5
1 (ax)	-66.4	-166.5	-73.2	-173.3	-66.3	-166.4
2 (ax)	82.4	106.4	81.1	105.0	82.2	106.1
3 (ax)	-230.1	-377.4	-231.7	-379.1	-225.9	-373.2
B3LYP[a]	53.8	20.5	56.1	22.7	56.8	23.5
G3[b]	8.8	-25.8	10.1	-24.4	11.8	-22.8

a. B3LYP population average.
b. G3 population average.

summarized in Tables 2.10 and 2.11. In all cases the use of the G3MP2 Avg pushed the results closer to the experimentally measured positive rotation. In the case of methanol and toluene the rotation was calculated to be positive for four of the five wavelengths. However, the calculated ORD does not have the correct form because it is becomes more negative as the wavelength decreases. Additional corrections are needed to obtain a qualitatively correct ORD in solution. Based upon the gas phase results, it is likely that the vibrational corrections need to be considered to bring a solvent phase calculations into agreement with experimental results.

2.3.4 Theoretical calculations of ECD

The electronic circular dichroism of (*S*)-(+)-carvone was calculated using TD-DFT/B3LYP with the aDZ basis set without the inclusion of corrections due to excited state geometry changes, Franck-Condon factors, and vibronic coupling between the ground and excited states.[97;98] The calculated rotational strengths and oscillator strengths for 10 transitions of all the conformers are given in Table 2.13. The CD plotted in Figure 2.7 was calculated

Table 2.9: Harmonic vibrational corrections (in deg dm^{-1} $(g/mL)^{-1}$) to the specific rotation at 589 nm for each conformer of (*R*)-carvone.

B3LYP/aDZ//B3LYP/6-311G(*d*,*p*)	
Conformer	Vibrational Correction
1 (eq)	-82.1
2 (eq)	143.7
3 (eq)	-118.7
1 (ax)	-100.1
2 (ax)	24.0
3 (ax)	-147.3

Table 2.10: Calculated optical rotation (deg dm^{-1} $(g/mL)^{-1}$) of (*S*)-(+)-carvone using the PCM model. Both the structure and the optical rotation were computed using the aDZ basis set.

	B3LYP/aDZ				
	Wavelength (nm)				
solvent	436	532	546	578	589
acetone	-191.1	-71.6	-64.2	-51.2	-47.7
acetonitrile	-198.0	-76.2	-68.6	-55.0	-51.3
benzene	-212.6	-80.6	-72.5	-58.2	-54.3
cyclohexane	-144.3	-29.4	-25.2	-25.2	-18.1
DMSO	-200.3	-77.0	-69.4	-55.7	-51.9
ethanol	-206.3	-81.1	-73.1	-59.0	-55.1
methanol	-187.8	-70.1	-62.9	-50.1	-46.6
toluene	-193.6	-73.6	-66.1	-53.0	-49.3

using the following equations

$$CD_i = 0.0247 \sum_{j=1}^{N} \frac{R_j \nu_j}{\sigma} e^{\frac{(\nu-\nu_j)^2}{\sigma^2}} \tag{2.5}$$

$$CD_{total} = \sum_{1}^{6} P_i \cdot CD_i \tag{2.6}$$

where CD_i is the CD for the ith conformer, R_j is the rotational strength 10^{-40} erg esu cm Gauss^{-1}, ν_j is the frequency in cm^{-1}, respectively, of each CD band, and P_i is the population of the ith conformer. The peak broadening parameter σ was chosen to be 2000 cm^{-1}.[99] The positions of the excited states are close to expected values based upon the CD spectrum and data from

Table 2.11: Calculated optical rotation (deg dm^{-1} (g/mL)$^{-1}$) of (*S*)-(+)-carvone using the PCM model. The ORD was calculated using structures optimized with B3LYP/aDZ and the relative population of each conformer was determined using the Gibbs freee energy obtained from G3MP2 calculations.

	G3MP2				
	Wavelength (nm)				
solvent	436	532	546	578	589
acetone	-104.8	-34.3	-30.3	-23.3	-21.4
acetonitrile	-60.6	-9.3	-6.9	-3.1	-2.1
benzene	-116.2	-41.8	-37.3	-29.5	-27.4
cyclohexane	-45.5	-1.0	0.7	3.4	4.0
DMSO	-62.1	-16.2	-13.4	-8.7	-7.5
ethanol	-75.2	-18.3	-15.4	-10.5	-9.2
methanol	-41.7	-0.3	1.4	3.9	4.4
toluene	-87.3	-22.7	-19.3	-13.7	-12.3

Mineyama *et. al.*[26] The measured excited state transition at 266.72 nm for the equatorial 1 conformer is close to the calculated value of 265 nm.[26] There is not significant aggreement between theory and experiment because of the lack of vibrational structure in the ECD. The calculated position of the $n \rightarrow \pi^\star$ for this ketone is 349 nm which is in the correct range of experimental data. The frequencies of the calculated transitions was scaled by factor of 0.95 so the wavelength matched match the highest intensity peak of the ECD in the $n \rightarrow \pi^\star$ region.

The position of the electronic features were close to their expected positions but the lack of vibrational contributions is believed to be the primary explanation for the large disagreement between experimental and theoretical ECD for the $n \rightarrow \pi^\star$ transition. Any correction to obtain an accurate CD spectrum would need to include vibronic coupling into the theory. The circular dichroism for carvone in the gas phase and in solution with various solvents including cyclohexane have the same general structure. The structure of the ECD over the $n \rightarrow \pi^\star$ in the gas phase and in each solvent starts negative and crosses zero to become positive but the position of the zero crossing, the number of peaks to the left and right of the zero crossing varies and the resolution changes with solvent choice. Nonetheless, it is unlikely that the difference in sign of theoretical and experimental ORD is due to solvent

A.

B.

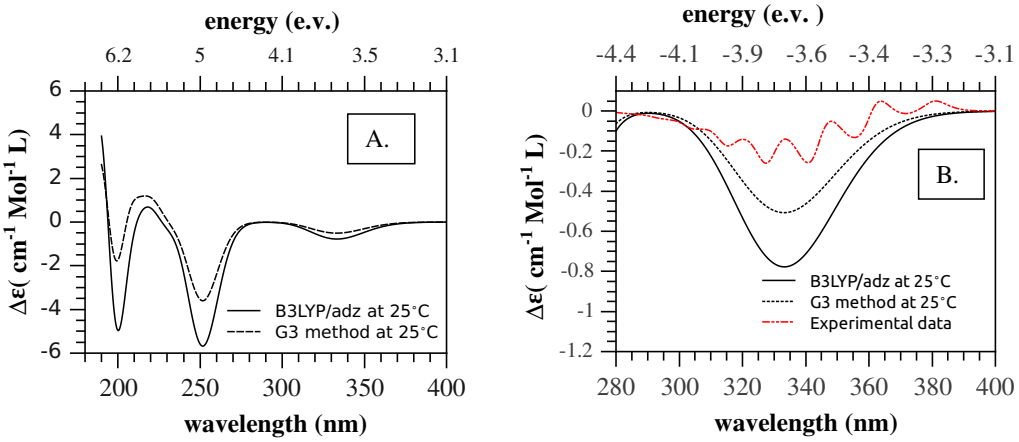

Figure 2.7: Computed ECD spectrum of (S)-(+)-carvone. Figure A. is a plot theoretical ECD calculated using populations from the G3 method and B3LYP/adz. Figure B. is a comparison of theory and experimental CD of (S)-(+)-carvone in cyclohexane.

effects. Based upon the calculations in Figure 2.7 there should be many other strong ECD features below 250 nm.

2.4 Summary and Conclusions

We have carried out both experimental and theoretical studies of the optical activity of carvone in order to elucidate the potential importance of solvent effects on its ORD and CD spectrum. Correlation of the experimentally determined ORD in various solvents with a variety of parameters, including dipole moments, Kamlet-Taft parameters and others, suggest that solvent polarization plays the most significant role in the measured response. However, the correlation in this case is still weak, which is not surprising given that such parameters do not take into account the conformational flexibilty of the carvone solute. Experimental CD measurements confirm the vibrational structure in the $n \rightarrow \pi^*$ regime reported earlier, though the previous assignment of this progression to the carbonyl stretching mode is not borne out by quantum chemical computations. Interestingly, the gas-phase CD spectrum agrees better with solution-phase CD spectra taken in polar rather than non-polar solvents. We offer a hypothesis for this phenomenon based on the observation

that solvents with strong dipole moments ($>$ 2.5 Debye) can exhibit a "band" structure in which electrons (such as those excited from the solute) can occupy quasi-stationary states of the solvent molecules. Such a band structure will not exist for non-polar solvents, which thus perturb the solute's diffuse excited states more strongly compared to the gas-phase. Although this hypothesis is appealing and appears to account for the current set of observations, more experimental and computational studies will be necessary to test it.

High-level coupled cluster computations of the ORD of carvone are found to yield incorrect signs compared to solution-phase experiments unless accurate Boltzmann populations and harmonic vibrational corrections are included. While some of the discrepancy between theory and experiment in this case undoubtedly arises from the lack of incorporation of solvent effects in the former, in this case it appears to be more important to model the conformer energetics correctly and to include temperature-dependent vibrational motion. Also, the inclusion of solvent effects using the PCM model predicts results similar to the gas phase calculations when the same method and basis set are used and vibrational corrections are not included. This further supports the argument that vibrational corrections are of primary importance to calculating an accurate ORD in the case of carvone.

2.5 Acknowledgements

This work was supported by grants from the U.S. National Science Foundation. Contributions from U. Tennessee were funded by grant number CHE-0650524, and those from Virginia Tech by CHE-1058420 and a Multi-User Chemistry Research Instrumentation and Facility (CRIF:MU) award CHE-0741927. Also the authors would like to thank undergraduate student Jin Shim for his assistance in recording some of the experimental measurements of ORD.

Table 2.12: parameters for the one wavelength drude fit $\theta = \frac{\kappa}{\lambda^2 - \lambda_0^2}$.

Solvent	λ_0	κ
1-octanol	216.1	1.67×10^7
2-butanol (racemic)	185.1	1.56×10^7
2-butanone	225.7	1.49×10^7
acetone	191.5	1.69×10^7
acetonitrile	216.1	1.64×10^7
benzene	238.0	1.50×10^7
benzonitrile	216.1	1.93×10^7
butanal	199.3	1.65×10^7
cyclohexane	199.3	1.65×10^7
cyclopentanone	205.7	1.90×10^6
DMSO	242.6	2.04×10^7
ethanol	219.2	1.89×10^7
methanol	225.6	1.53×10^7
nitrobenzene	147.7	2.15×10^7
nitroethane	215.6	1.81×10^7
propionitrile	195.8	11.59×10^7
toluene	233.3	1.40×10^7
valeronitrile	195.0	1.53×10^7

Table 2.13: The oscillator strength and rotatory strength of (S)-(+)-carvone. The wavelength λ is in nanometers, f is the dimensionless oscillator strength, and R is the rotational strength in 10^{-40} erg esu cm Gauss^{-1}.

	eq1			eq2			eq3	
λ	f	R	λ	f	R	λ	f	R
349.12	0.0006	-2.9161	354.40	0.0002	-3.1918	352.89	0.0002	-0.4133
264.91	0.0477	-24.542	262.47	0.0123	8.1153	263.48	0.0050	-2.1767
237.92	0.1568	2.3744	236.08	0.1555	-39.2539	234.70	0.1855	33.2424
215.53	0.0173	-7.2472	216.09	0.0251	13.0810	214.31	0.0046	4.3819
210.54	0.0032	4.5795	209.58	0.0317	9.3396	209.83	0.0027	-2.2662
209.37	0.0238	-31.6213	206.17	0.0141	15.379	207.64	0.0073	-3.8939
203.48	0.0084	5.6527	202.64	0.0041	0.8495	201.79	0.0015	3.9314
201.41	0.0101	4.3470	200.29	0.0133	-24.6184	200.47	0.0013	0.5372
198.74	0.0039	6.4503	197.64	0.0013	-2.1935	198.69	0.0093	-2.1112
197.12	0.0305	4.2940	197.24	0.0075	3.9527	194.69	0.0044	12.4543
	ax1			ax2			ax3	
λ	f	R	λ	f	R	λ	f	R
356.47	0.0005	4.0869	354.71	0.0004	4.1728	354.05	0.0002	-0.2026
269.28	0.0507	5.5880	275.49	0.0124	-5.8581	274.40	0.0063	1.4787
239.33	0.1456	-8.1218	235.83	0.1375	-41.0432	236.36	0.1608	54.3385
219.05	0.0050	-4.2183	223.54	0.0199	3.1369	222.85	0.0011	-2.0680
213.02	0.0114	1.2183	216.06	0.0161	15.5187	213.85	0.0021	-4.1256
206.85	0.0032	-1.3343	210.08	0.0070	12.1064	211.77	0.0211	-4.6739
203.21	0.0016	-2.1332	203.82	0.0046	-6.6964	205.60	0.0122	-14.9251
202.82	0.0108	2.7834	203.15	0.0000	-0.0838	201.52	0.0126	-6.9943
198.00	0.0023	-1.0555	200.77	0.0452	21.4622	200.75	0.0020	-0.1982
196.92	0.0062	2.0642	199.49	0.0010	2.5559	197.86	0.0116	17.2194

Chapter 3

Temperature Dependent Circular Dichroism of Carvone

3.1 Introduction

The material herein is not only applicable to circular dichroism it can be extended to other spectroscopic techniques as well. Any experiment where the measured signal has a form like Equation 3.1 can use this method with obvious considerations of signal to noise. This study follows two previous studies that considered the electronic circular dichroism of carvone in solvents. The first was performed by Ballard *et. al*[23] reported the temperature dependent CD and derived the enthalpy of formation for the higher energy axial structure to be 0.087 eV with temperature dependent data. Temperature dependent CD data of carvone in solution phase was published Suga *et. al* as well.[24] They studied carvone in decalin at 298.15 K and 419.15 K as well as a 1:3 by volume mixture of methycyclohexane and isopentane at 181.15 K and 298.15 K. Also, 3-methylcyclopentanone has been studied using CD as a method to determine entropy and enthalpy of formation of the higher energy conformer.[100] This study looks at ECD of carvone in multiple solvents given in Table 3.1. To explore conformational effects with carvone in various solvents the temperature dependence was examined and compared with gas phase ECD (see 2.6). The method of analysis used by Ballard *et. al* and Basheer to determine the ΔH and ΔS rely on the assumption that the molecule has

only two conformers.[23;100] Ballard's paper ignored the rotamers of carvone and assumed that it comprised of two primary structures, referred to herein as the axial and equatorial conformers. It is known that carvone can exist in at least six conformers (see page 16). There is much more discussion on the conformational flexibility of carvone listed in Chapter 2. The important thing to note is that the conformers of carvone can be classified as either equatorial or axial depending upon whether the bond is approximately parallel or perpendicular to the plane formed by the cyclic portion of the molecule. The angle formed between the normal of the plane formed by atoms $c1$, $c2$, and $c3$ and bond $c7-c8$ as given in Figure 2.1 determines whether it is axial or equatorial. The equatorial conformer is nearly perpendicular and the axial conformer is nearly parallel.

In this analysis we ignore the rotamers of carvone and also assume that only two conformers exist. With this assumption, the ECD of a molecule is at a given temperature and wavelength is given by equation 3.1 where $\Delta\epsilon_0$ is the ECD of the lowest energy conformer which in this case of carvone is the equatorial conformer. $\Delta\epsilon_1$ is the ECD of the higher energy axial conformer and $\Delta G = \Delta H - T\Delta S$ is the difference in the Gibbs free energy between the two conformers.

$$\Delta\epsilon\left(\lambda, T\right) = \frac{\Delta\epsilon_0\left(\lambda\right) + \Delta\epsilon_1\left(\lambda\right) e^{\frac{-\Delta G}{K_B T}}}{1 + e^{\frac{-\Delta G}{K_B T}}} \tag{3.1}$$

If the ECD of the two conformers is know at the selected wavelength then the population of each conformer can be determined for any temperature from Equation 3.1. The populations f_i of each respective conformer are given by equations 3.2 and 3.3.

$$f_1 = \frac{e^{\frac{-\Delta G}{K_B T}}}{1 + e^{\frac{-\Delta G}{K_B T}}} \tag{3.2}$$

$$f_0 = \frac{1}{1 + e^{\frac{-\Delta G}{K_B T}}} \tag{3.3}$$

From the ratio of the populations of the two conformers the difference in entropy and enthalpy can be determined from Equation 3.4 using a Van't Hoff plot.

$$K_B \log\left(\frac{f_1}{f_0}\right) = \frac{-\Delta H}{t} + \Delta S \tag{3.4}$$

The challenge of employing this method lies in the determination of $\Delta\epsilon_0$ and $\Delta\epsilon_1$. In the low and high temperature limit the ECD is given by Equations 3.5 and 3.6.

$$\Delta\epsilon\left(\lambda, T \to 0\right) = \Delta\epsilon_0\left(\lambda\right) \tag{3.5}$$

$$\Delta\epsilon\left(\lambda, T \to \infty\right) = 0.5\left(\Delta\epsilon_0\left(\lambda\right) + \Delta\epsilon_1\left(\lambda\right)\right) \tag{3.6}$$

Using the High and low temperature limits to experimentally approximate the ECD of each conformer. Combining Equations 3.1, 3.5, and 3.6 to solve for the ECD at any temperature in terms of the ECD at the low and high temperature limits yields Equation 3.7.

$$\Delta\epsilon(\lambda, T) = \Delta\epsilon(\lambda, T \to 0)\tanh\left(\frac{\Delta G}{2\,K_B\,T}\right) + \frac{2\Delta\epsilon(\lambda, T \to \infty)}{1 + e^{\frac{\Delta G}{K_B T}}} \tag{3.7}$$

This formula was derived by first by Ballard *et. al* with the minor difference that they did not consider the entropy difference between the conformers.[23] There does not seem to be any reason to leave out this term. This term was first included by Basheer, Pagni and Compton.[101]

Both Ballard *et. al* and Basheer *et. al* ignored the fact that the solvent expansion has an effect on concentration of the solution and therefore the CD used in the extrapolation. The concentration can be modified with solvent temperature expansion coefficient assuming that the solution is dilute. Assuming the solution is dilute 3.1, Equation 3.1 is modified to include a solvent expansion coefficient given in Equation 3.8.

$$\Delta\epsilon\left(\lambda, T\right) = (1 + \alpha(t - t_0))\frac{\Delta\epsilon_0\left(\lambda\right) + \Delta\epsilon_1\left(\lambda\right)e^{\frac{-\Delta G}{K_B T}}}{1 + e^{\frac{-\Delta G}{K_B T}}} \tag{3.8}$$

furthermore, Both Ballard *et. al* and Watheq *et. al* made the assumption that the ECD of each conformer is independent of temperature. This assumption is reasonable considering that the vibrational population would be the main source of error. The vibrational population should not contribute greatly to the ECD. Nonetheless, vibrations can definitely have an effect. For example, Wiberg *et. al* measured the optical rotation of the bicyclic α-pinene, β-pinene, pinane, camphene, camphor, and fenchone as a function of temperature.[102] These molecules are conformationally rigid but they do have some low frequency vibrational

modes. Wiberg *et. al* observed that the optical rotation that the varied with temperature even though α-pinene is largely a rigid molecule lacking conformational degrees of freedom. The effect was small which justifies it being ignored in the case of carvone where the temperature dependence of the ECD is dominated by the conformational flexibility.

3.2 Experimental and Analysis Details

The circular dichroism data was acquired using an Aviv model 202 CD spectrometer in a 1mm quartz cuvette for the solution phase measurements and 1 cm quartz cuvette for the gas phase measurements. Each reported ECD measurement is the average of three scans and each point is averaged for four seconds. The concentration at each temperature was corrected using the solvent thermal expansion coefficients. The ECD was measured at 293 K, 303 K, 313 K, 323 K, and 333 K. A wavelength step size of 0.5 nm and a monochromator bandwidth 0.5 nm where used for each scan. The temperature was allowed to equilibrate for 90 seconds once the setpoint temperature was reached. In the case of cyclohexane and acetone, one

Table 3.1: Sample concentrations ($^{g}/_{ml}$) used in the CD measurements.

Solvent	Concentration($^{g}/_{ml}$)	volumetric expansion coefficient($\frac{\Delta V}{V}1000$)
2-butanal	0.13	1.067
2-butanone	0.12	1.084
acetone	0.04	1.488
acetonitrile	0.11	1.02
benzene	0.12	1.14
cyclohexane	0.03	1.168
cyclopentanone	0.13	0.757
ethanol	0.19	1.427
propionitrile	0.08	0.953
valeronitrile	0.05	0.759

of the the temperature measurements was clearly an outlier and therefore ignored. When performing the analysis, the positions of the maximum and minimum might shift slightly between measurements so the maximum/mininum value of a small range was used when performing the analysis at a peak/valley. Acetone, cyclopentanone and butanal restrict the usable range of the ECD because of solvent absorption. In general, to minimize the error of

a the CD measurements the total absorption to decrease the light intensity by $I_0 e^{-2}$.[17] All ECD spectra were taken with (S)-(+)- carvone except where benzene and ethanol were used as the solvent. For the solvent 2-butanone the error increased slightly in the range 300 to 330nm because of solvent absorption. Some peaks at shorter wavelength were not included because the increased experimental error inhibited the analysis.

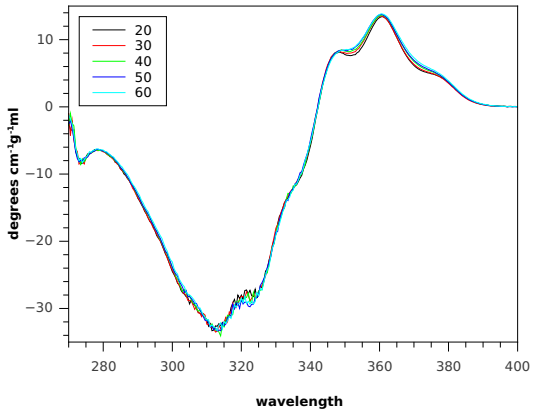

Figure 3.1: temperature dependent ECD of carvone in 2-butanone

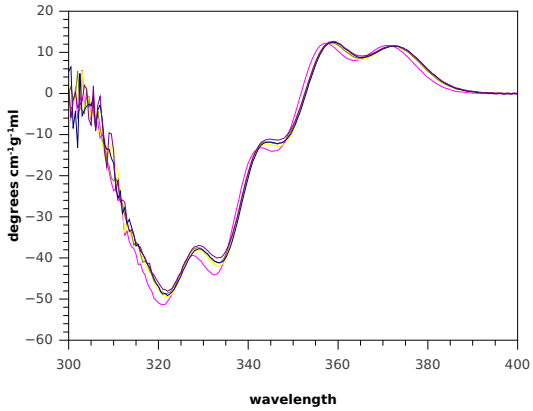

Figure 3.2: temperature dependent ECD of carvone in acetone

3.3 Experimental Results

The ΔH and ΔS results for each solvent are given in Table **??**. For the purpose of comparison with those obtained from G3MP2 simulations in solvents, the average ΔH and ΔS for the

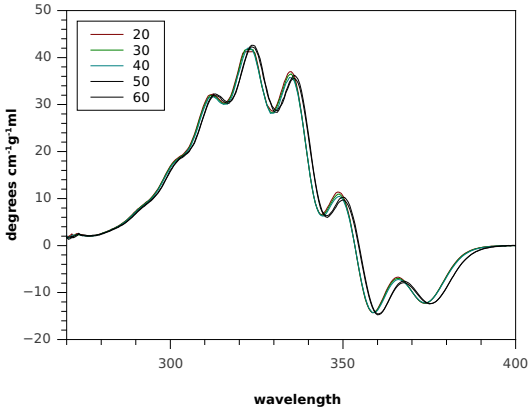

Figure 3.3: temperature dependent ECD of carvone in benzene

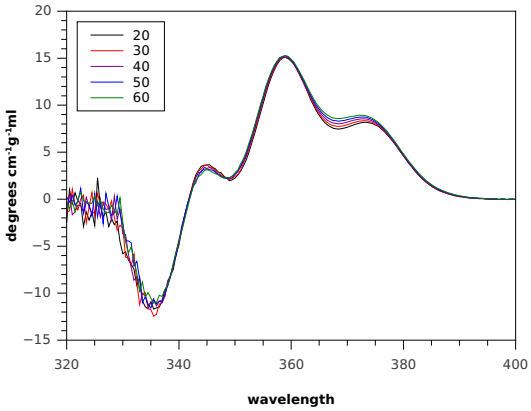

Figure 3.4: temperature dependent ECD of carvone in butanal

axial conformers was subtracted from the average ΔH and ΔS of the equatorial conformers. The details of the calculations are given in Chapter 2, Section 2.1. For all measurements the observed trend was that the ECD decreased for (S)-(+)-carvone with increase in temperature while the converse was true for (R)-(-)-carvone. The effects of the solvent are quite evident from the CD spectra taken for this chapter. For nonpolar solvents like cyclohexane, the vibronic peaks were well defined in low polarity solvents but as the solvent polarity increased the resolution decreased. This is a common observation. Furthermore, the more polar solvents tended to redshift the CD spectrum. The indicate that the excited state is more polar then the ground state because of the decreased energy of the transition. It is interesting that the sign of that the 3rd lowest energy vibronic in the $n \rightarrow \pi^{\star}$ transition region changes sign when ethanol or butanal is used as a solvent. This is easily ascertained by a visual

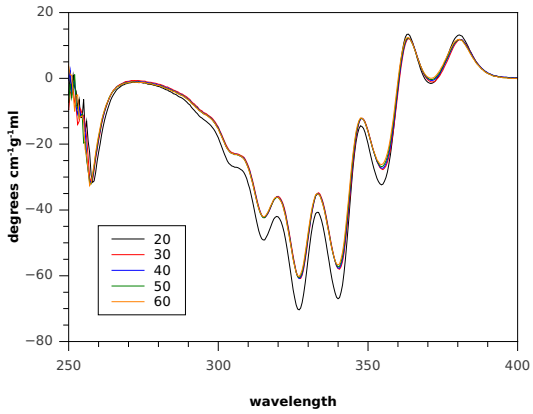

Figure 3.5: temperature dependent ECD of carvone in cyclohexane

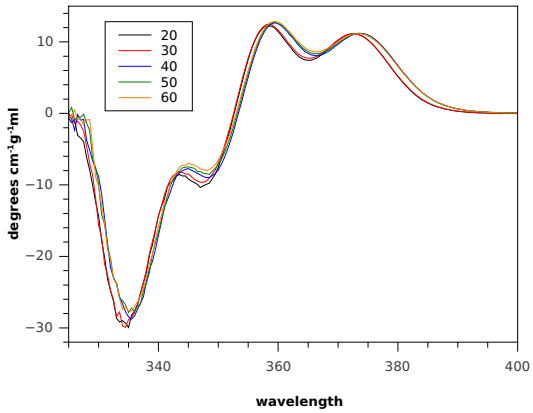

Figure 3.6: temperature dependent ECD of carvone in cyclopentanone

inspection of Figures 3.1 through 3.9. A comparison of solvents of the ECD in various solvents is shown in figure 2.5. Solvents can have a drastic effect on the ECD and the ORD, even to the point of a changing sign.[103]

3.3.1 Errors from Linear Extrapolation of ECD limits

Ballard *et. al* and Al-Basheer extrapolated to to the limits $\Delta\epsilon\left(\lambda, T \to 0\right)$ and $\Delta\epsilon\left(\lambda, T \to \infty\right)$ with a straight line. The error associated with this method was not discussed. R.E. Ballard measured the ECD of carvone at over a range of 195-500 Kelvin. temperatures and Al-Basheer measured the ECD of 3-methylcyclopentanone over 4 or 5 temperatures in a variety of solvents. This Chapter analyzes this approach to quantify the error bars associated with this method. We began by analyzing an ideal system and determine the error between the

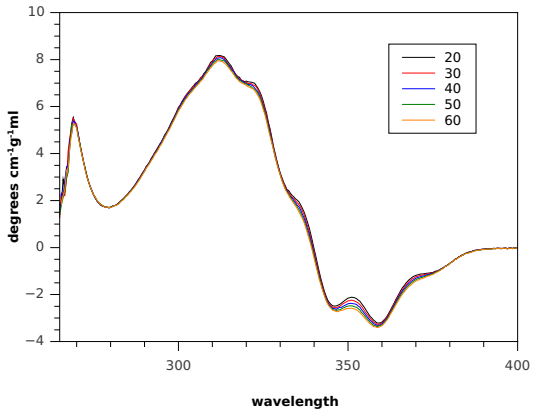

Figure 3.7: temperature dependent ECD of carvone in ethanol

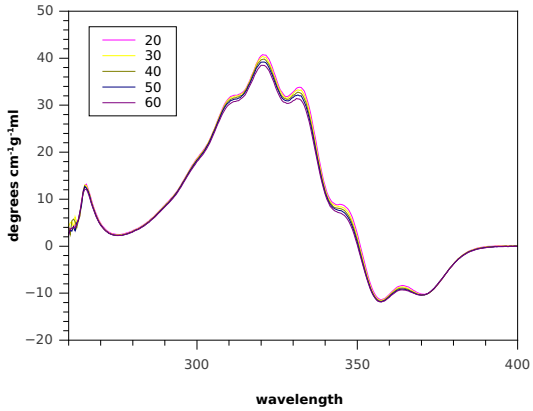

Figure 3.8: temperature dependent ECD of carvone in propionitrile

actual ΔH and ΔS of the model and the one obtained by extrapolating to low and high temperature limits. A linear extrapolation is an approximation of the tangent line at the central temperature of the measurement, provided that the temperature variation is not large. The slope of the CD as a function of temperature and inverse temperature β is given in Equations 3.9 and 3.10.

$$M(t) = \frac{\Delta H \, \mathrm{e}^{\frac{-\Delta H + t\Delta S}{R\,t}} \, (\Delta\epsilon_1 - \Delta\epsilon_0)}{\left(1 + \mathrm{e}^{\frac{-\Delta H + t\Delta S}{R\,t}}\right)^2 R\,t^2} \tag{3.9}$$

$$M(\beta) = \frac{-\Delta H \, \mathrm{e}^{\frac{-\beta\Delta H + \Delta S}{R}} \, (\Delta\epsilon_1 - \Delta\epsilon_0)}{\left(1 + \mathrm{e}^{\frac{-\beta\Delta H + \Delta S}{R}}\right)^2 R} \tag{3.10}$$

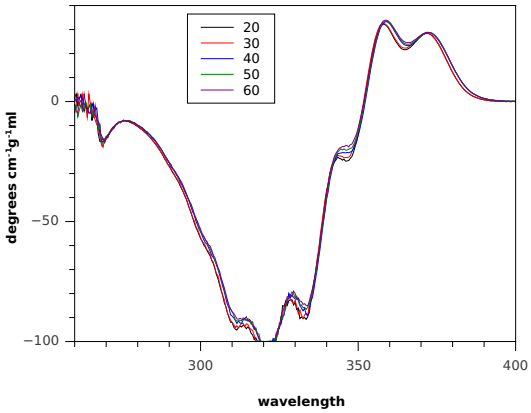

Figure 3.9: temperature dependent ECD of carvone in valeronitrile

Approximations of the ECD of the two conformers is given in Equations 3.11 and 3.12.

$$\Delta\epsilon_0(\lambda) \approx \Delta\epsilon(\lambda, t) - M(t)\, t \tag{3.11}$$

$$\Delta\epsilon_1(\lambda) \approx 2\left(\Delta\epsilon(\lambda, \beta) - M(\beta)\, \beta\right) - \Delta\epsilon_0(\lambda) \tag{3.12}$$

The goal of this exercise is to obtain the population of the conformers as a function of temperature. Using Equation 3.4 the enthalpy and entropy can be determined from the population. Equation 3.13 is obtained by combining Equations 3.1, 3.11, and 3.12 and gives the relationship between the population and the limits obtained from extrapolating.

$$f_0 = \frac{2M(\beta)\,\beta - M(t)\,t}{2\,M(\beta)\,\beta - 2\,M(t)\,t} = \frac{3}{4} \tag{3.13}$$

Equation 3.13 shows that using a linear extrapolation to obtain the limits is incorrect because it predicts that the population of the lowest energy conformer is constant. Therefore, this study suggests that using that a procedure using linear extrapolation to obtain the limits of the circular dichrosim is flawed.

3.3.2 Fitting of ECD to determine ΔH and ΔS

In this section we attempt to obtain the enthalpy and entropy difference for the two conformer case without relying on the extrapolation approximation to obtain the CD of the two conformers. There are multiple methods available for such fitting. For a fit like

this the excel solver routines would work. Nonetheless, I used a different approach which is extensible to systems with more conformational degrees of freedom. The CD at any temperature is given by the Equation 3.14.

$$\begin{bmatrix} \Delta\epsilon(T_1) \\ \Delta\epsilon(T_2) \\ \Delta\epsilon(T_3) \\ . \\ . \\ . \\ \Delta\epsilon(T_n) \end{bmatrix} = \begin{bmatrix} P_1(T_1) & P_2(T_1) & .. & P_m(T_1) \\ P_1(T_2) & P_2(T_2) & .. & P_m(T_2) \\ P_1(T_3) & P_2(T_3) & .. & P_m(T_3) \\ . & & ... & . \\ . & & .. & . \\ . & & . & . \\ P_1(T_n) & P_2(T_n) & .. & P_m(T_n) \end{bmatrix} \begin{bmatrix} \Delta\epsilon_1 \\ \Delta\epsilon_2 \\ \Delta\epsilon_3 \\ . \\ . \\ . \\ \Delta\epsilon_m \end{bmatrix} \tag{3.14}$$

where the left side of the equation is the CD as a function of temperature and the right side is a matrix of the populations of the inidividual conformers at each temperature multiplied by the ECD of each conformer at a single wavelength. If the population matrix is known then there is a best set of the $\Delta\epsilon_i$ that reproduces the temperature dependence of the ECD. This of course requires the condition that $n \geq m$. The goal is to find the set of ΔH_i, ΔS_i, and $\Delta\epsilon_i$ that reproduces the spectrum with smallest sum squares error. To optimize the fit a two stage approach was used that varied ΔH_i, ΔS_i and then used linear regression to find the data that best reproduced the spectrum. the LAPACK package subroutine DGELS(see www.netlib.org/lapack/) was used to solve the linear regression problem. This allows for evaluation at many different wavelengths. For carvone the range depended upon the noise of the measurement. All wavelengths were included unless precluded by excessive noise. a simple grid was used to find the optimum values of ΔH and ΔS. For a system with more conformers the code can be adapted to use other optimization approaches. To test the validity of this approach a simple two conformer *ideal* system with known parameters was fit so the values of ΔH, ΔS, $\Delta\epsilon_1$, and $\Delta\epsilon_2$. The results of this *ideal* fitting are given in Table 3.2.

Table 3.2: A comparison of the the exact and fitted values for a two conformer system

	exact	fit	percent difference
ΔH	3.450E-02	3.453E-02	-9.28E-002
ΔS	5.500E-05	5.520E-05	-3.64E-001
$\Delta\epsilon_1$	2.300E+01	2.299E+01	3.11E-002
$\Delta\epsilon_2$	-2.100E+01	-2.095E+01	2.23E-001

Table 3.3: The fits of the experimental data using the fitting approach presented in Section 3.3.2. The error is reported as the average of the squared difference between experimental data and the fit.

Solvent	ΔH fit	ΔS fit	*Error*	ΔH pcm	ΔS pcm
2-butanone	9.98E-002	-1.00E-004	0.01634		
acetone	8.49E-002	-8.42E-005	0.12087	3.71E-002	-4.57E-005
benzene	6.74E-002	-7.50E-005	0.63738	3.65E-002	-3.52E-002
butanal	7.09E-002	-9.09E-006	0.00000		
cyclohexane	7.58E-002	-9.09E-006	0.01382	3.38E-002	-1.33E-005
cyclopentanone	1.27E-002	7.88E-005	1.00163		
ethanol	1.44E-002	8.98E-005	0.00016	3.66E-002	-4.80E-005
propionitrile	3.50E-002	-8.90E-005	0.01665		
valeronitrile	1.50E-002	-9.09E-006	0.81526		

3.3.3 ECD of the Equatorial and Axial conformers

The temperature dependence of the ECD combined with accurate calculations of the enthalpy and entropy difference between the two conformers allows for the extraction of the ECD of the individual conformers. To avoid error resulting from the ECD switching order unduly because of experimental error, the maximum difference in temperature was used to calculate the equatorial and axial contribution.

$$P_{eq}(T) = \frac{1}{1 + e^{\frac{-\Delta H + T\Delta S}{K_B T}}} \tag{3.15}$$

$$P_{ax}(T) = 1 - P_{eq}(T) \tag{3.16}$$

$$\Delta\epsilon_{eq} = \frac{CD(T_1)P_{ax}(T_2) - CD(T_2)P_{ax}(T_1)}{P_{eq}(t_1)P_{ax}(T_2) - P_{eq}(T_2)P_{ax}(T_1)} \tag{3.17}$$

$$\Delta\epsilon_{ax} = CD(T) - P_{eq}(T)\Delta\epsilon_{eq} \tag{3.18}$$

In equations 3.15 through 3.18 $P_{eq}(T)$ is the population of the equatorial conformer at a given temperature, $P_{ax}(T)$ is the population of the axial conformer at a given temperature, $CD(T)$ is the total CD, and $\Delta\epsilon_{eq}$ and $\Delta\epsilon_{ax}$ are the equatorial and axial contributions to the ECD. Equations 3.15 through 3.18 are easily extensible to other spectroscopic techniques where there are multiple conformers provided you have acquired data with at least n well separated temperatures. Carvone represents an interesting case when comparing the axial and equatorial ECD. Because the axial conformer is higher in energy, the spectrum tends toward the ECD with higher temperature. When examining closely the data from each experimental run it becomes apparent the the major sign change does not depend upon the temperature, at least to the precision of the measurements. This is true for the gas phase experimental data as well(see Figure 2.6). This implies that the major zero crossing of the axial and equatorial conformers occurs very close to the same position. Using the relations given in Equations 3.15 through 3.18 the ECD of the axial and equatorial conformer is calculated. This is done for the ECD as measured in acetone, ethanol, benzene, and cyclohexane. The equatorial and axial conformers have the opposite sign but the magnitude of axial ECD is consistently larger than the equatorial ECD. The reason for this is the changing direction of the transition magnetic dipole moment for the $n \rightarrow \pi^{\star}$ with the change of conformation while the electric transition dipole moment for the same transition remains relatively unchanged.

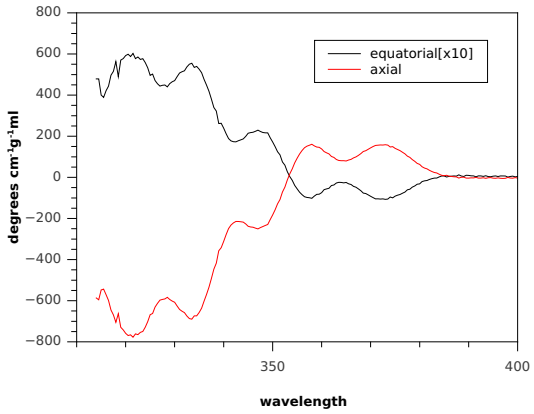

Figure 3.10: Deconvoluted ECD spectrum of carvone in acetone.

The structures used to calculate the ECD were optimized using density functional theory with the B3LYP functional and aug-cc-pVDZ basis set and the ECD of each conformer

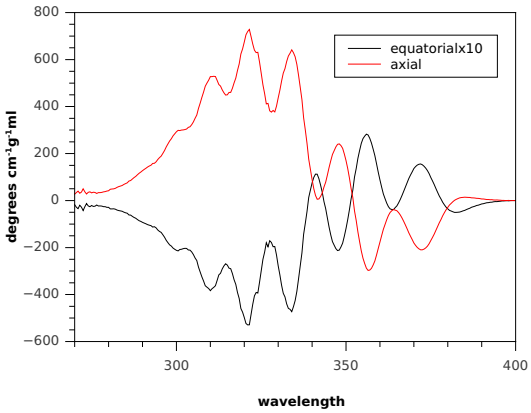

Figure 3.11: Deconvoluted ECD spectrum of carvone in benzene.

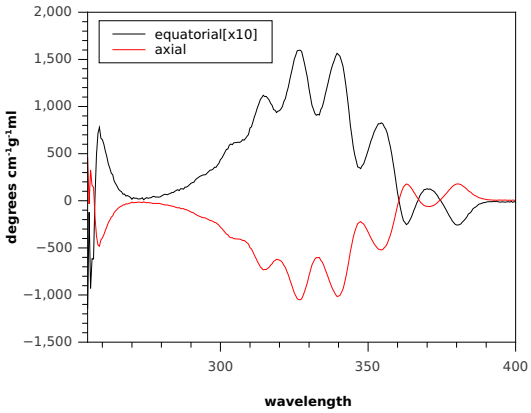

Figure 3.12: Deconvoluted ECD spectrum of carvone in cyclohexane.

was calculated using time dependent density functional theory with the B3LYP functional and the aug-cc-pVDZ basis set. The structure used to calculate the ECD is given the computational methods section of Chapter 2. Comparison between the experimental and theoretical ECD is complicated by the fact that vibronic effects were not included in the calculation. Nonetheless, the deconvolution of the ECD allows for easy comparision between the axial and equatorial ECD and theoretical predictions. For two of the three rotational isomers of the axial conformer the $n \rightarrow \pi^{\star}$ transition of (S)-(+)-carvone was positive when calculated B3LYP/aVDZ while the calculated ECD of the equatorial conformer of (S)-(+)-carvone for the $n \rightarrow \pi^{\star}$ was negative for all three cases. Furthermore, the magnitude of the equatorial ECD was much smaller than the magnitude of the axial conformers which agrees with the experimentally observed results. The results are already presented in Table 2.13.

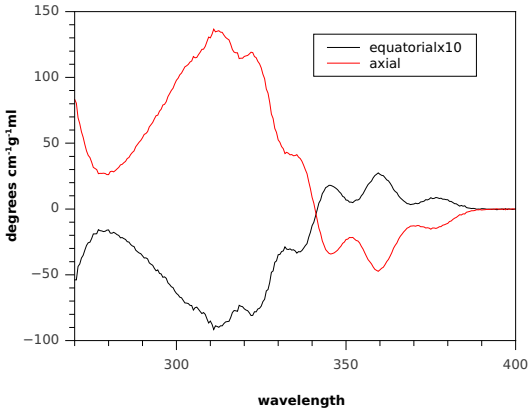

Figure 3.13: Deconvoluted ECD spectrum of carvone in ethanol.

3.4 Results and conclusion

The contribution of the equatorial and axial conformers to the ECD was seperated using high accuracy G3MP2 calculations of ΔH, ΔS with the solvent model coupled with temperature dependent ECD spectra of carvone's $n \rightarrow \pi^\star$ transtion. The relationship between the axial and equatorial conformers was interesting. The magnitude of the ECD of the axial conformer was much larger than the ECD of the equatorial conformer. Also, the axial and equatorial conformers have the opposite sign and if the the magnitude difference is ignored the the spectra are almost mirror images. Ballard *et. al* also inferred this trend from using sector rules for α,β unsaturated ketones although no attempt to quantify the magntitude was made. The same trend can be seen when examining the lowest energy transition when calculated with TD-DFT simulations of the ECD in solvents given in Table 2.13. The ECD of the equatorial and axial conformers of carvone have the opposite sign. The broadening of the ECD due to vibronic effects is not included in the simulation so the sign changes over the $n \rightarrow \pi^\star$ region are not simulated by the ECD. The validity of the experimental determination of ΔH and ΔS between the two conformers, ϵ_1, and ϵ_2 using an extrapolation based procedure was found to have some glaring inconsistiencies which limit its applicability. A two stage optimization where, given a ΔH and ΔS, the optimum values of ϵ_1 and ϵ_2 are found. Each iteration considers different values of ΔH and ΔS which then are used to calculate new optimum values of ϵ_1 and ϵ_2 with linear regression. The set that minimizes the sum of the squares difference between the experimental and theoretical result is taken

as the result. The results of this fitting between experimental and theoretical data are given in Table 3.3 In general, it is recommended that a computational analysis of the potential energy surface of labile moieties of the molecule are included particularly when working with optical activity where enantiomers can have a drastically different circular dichroism. These should be followed by higher accuracy model chemistries if the molecule is not to large.

Chapter 4

Negative Ion Properties of N-paranitrophenylsulfonylalanine and N-paranitrophenylalanine

4.1 Abstract

(S)- and (R)- chiral molecular complexes of N-paranitrophenylsulfonylalanine (NPNPSA) and N-paranitrophenylalanine (NPNPA) were synthesized, and their negative ion properties were experimentally and theoretically studied. The valence anions of both (S)- and (R)-NPNPSA were studied by negative ion photoelectron spectroscopy. As expected, both of these chiral molecules share the same valence adiabatic electron affinities, 1.7 ± 0.1 eV, and vertical detachment energies, 2.3 ± 0.1 eV. Calculations for four low lying conformers of (S)- and (R)- NPNPSA valence anions gave adiabatic electron affinities in the range of 1.6 to 2.1 eV and vertical detachment energies in the range of 2.0 to 2.4 eV, which are substantially larger than the known AEA of 1.0 eV for the nitrobenzene valence anion.[104] For (S)- and (R)- NPNPA valence anions, six conformers were identified and predicted to have adiabatic electron affinities in the range of 0.7 to 1.2 eV and vertical detachment energies in the range of 0.9 to 1.6 eV. Collision induced dissociation energy thresholds for various channels of their deprotonated anions were measured and from this data, bond dissociation energies were

estimated employing the CRUNCH program. In addition, the bond dissociation energy for the deprotonated-NPNPSA/NPNPSA dimer cluster anion was determined to be 0.32 ± 0.08 eV. Dipole-bound anions for both molecules were studied using DFT methods. These studies were made in effort to examine the effects of each component in the extended molecule (i.e., a molecule-in-molecule, MIM, approach) as within each contains a nitrobenzene and alanine molecule within the larger molecular complex.

4.2 Introduction

Within the past two decades, new experimental and theoretical methods have been developed to explore the properties of complex molecules and their ions in the gas phase. The conformational flexibility and fragility of these extended molecules have required preparation of these gas phase species at low temperatures. Gentle heating of molecules from a surface into the gas phase followed by electron attachment in a nozzle jet allows for meaningful studies of photoelectron spectroscopy (PES) of parent negative ions for the determination of electron affinities. Likewise, electrospray ionization also allows the preparation of intact molecular anions, albeit often their deprotonated anions, for study by collision induced dissociation (CID).

Herein we employ both PES and CID techniques to study the negative ion properties of two newly synthesized amino acid derivatives. We also examine the influence of different well characterized moieties on the negative ion properties of the molecule as a whole by a molecule-in molecule (MIM) approach. In particular, the nitrobenzene moiety has been linked to (*S*)- and (*R*)- alanine either directly to form (*S*)- and (*R*)- N-paranitrophenylalanine (NPNPA) or indirectly via a sulfonyl (SO_2) bride to form (S)- and (*R*)- N-paranitrophenylsulfonylalanine (NPNPSA). A number of recent theoretical studies have explored the concept of MIM for the prediction of properties of large molecules.[105] The negative ion properties of the three "components" of these two molecules, nitrobenzene, sulfur dioxide and alanine have been well studied. The object of this study is to combine experiment and theory to examine how the molecular properties of these individual "components" of a large molecule can be correlated to that of the "super" molecule to better characterize these newly synthesized unnatural amino acids' negative ion properties.

Unnatural amino acids have become especially important in many areas of molecular biology where they act as protein markers.[106] The addition of unnatural amino acids to proteins has become a routine procedure in molecular biology and a number of review articles have appeared on this subject.[107–109]

4.3 Sample Preparation

4.3.1 Preparation of (*S*)-NPNPSA (2a) and (*R*)-NPNPSA (2b)

To synthesize (*S*)-NPNPSA (2a, see Figure 4.1), a 1 M sodium hydroxide solution (5 ml) was added to (*S*)-alanine (1a, 0.21 g, 2.40 mmol) and cooled to 0^{deg}C. 4- nitrobenzenesulfonyl chloride (0.82 g, 3.61 mmol) was next added in small portions, and the reaction mixture was stirred at room temperature overnight, followed by rinsing with ethyl acetate (20 ml).The aqueous layer was then acidified with 1 M hydrochloric acid (10 ml) and extracted with ethyl acetate (15 ml). The resultant organic layer was dried with magnesium sulfate, filtered, and concentrated. Column chromatography over silica gel with gradient elution from 5% to 20% methanol/dichloromethane gave the product 2a as a yellow solid (0.29 g, 44%). Its enantiomer (*R*)-NPNPSA (2b), was similarly prepared using (*R*)-alanine (1b, 0.23 g, 2.58 mmol), 1 M sodium hydroxide (7 ml) and 4-nitrobenzenesulfonyl chloride (0.87 g, 3.86 mmol), which yielded 2b as a white solid (0.24 g, 35%). The characterization results [1H NMR (300 MHz, DMSO (dimethyl sulfoxide)-d6) δ 8.37 (d, $J = 7.1$ Hz, 2H), 8.04 (d, $J = 7.1$ Hz, 2H), 3.68 (q, $J = 7.1$ Hz, 1H), 1.19 (d, $J = 7.1$ Hz, 3H)] match those reported in the literature.[110;111]

4.3.2 Preparation of (*S*)-NPNPA (3a) and (*R*)-NPNPA (3b)

To synthesize (*S*)-NPNPA (3a, see Figure 4.1), 20 ml of N,N-dimethylformamide (DMF) was added to (*S*)-alanine (1a, 0.95 g, 10.7 mmol). Potassium carbonate (2.95 g, 21.3 mmol) and potassium iodide (1.77 g, 10.7 mmol) were then added to the stirring solution. 4-Chloronitrobenzene (3.36 g, 21.3 mmol) was next added in small portions, and the reaction

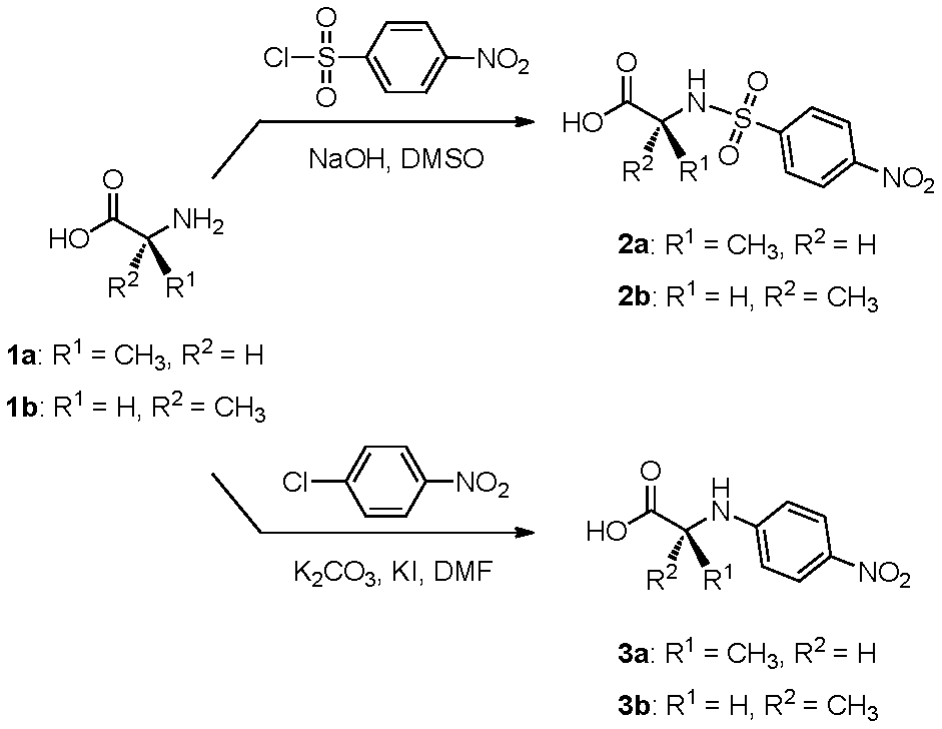

Figure 4.1: Diagram of the reaction used to create NPNPA and NPNPSA.

mixture was stirred and refluxed at 120 degC overnight. Next, the solvent was removed via rotary evaporation. The crude product was then dissolved in 50 ml of water, acidified with 1 M hydrochloric acid (20 ml), and extracted with ethyl acetate (50 ml). The resultant organic layer was dried with magnesium sulfate, filtered, and concentrated. Column chromatography over silica gel with gradient elution from 1 to 25% methanol/dichloromethane gave the product as a yellow solid (1.21 g, 54%). Enantiomer 3b was similarly prepared using (R)-alanine (1b, 0.88g, 9.90 mmol), 20 ml of DMF, potassium carbonate (2.74 g, 19.8 mmol), tetrabutylammonium iodide (3.66 g, 9.90 mmol), and 4- chloronitrobenzene (3.12g, 19.8 mmol), which yielded 3b as a yellow solid (0.67 g, 32 %). The characterization results [1H NMR (300 MHz, CD_3OD) δ 8.02 (d, 2H, J = 9 Hz), 6.60 (d, 2H, J = 9 Hz), 3.96 (q, 1H, J = 9 Hz), 1.48 (d, 3H, J=9 Hz)] match those reported in the literature.[112]

4.4 Experimental Methods

4.4.1 Photoelectron Spectroscopy Technique

Negative ion photoelectron spectroscopy was conducted by crossing a mass-selected beam of parent negative ions with a fixed-frequency photon beam and energy-analyzing the resultant photodetached electrons. The photodetachment process is governed by the relationship $h = EBE + EKE$, where h is the photon energy, EBE is the electron binding energy or the transition energy needed to take the anion to a particular vibrational state of its neutral counterpart, and EKE is the electron kinetic energy. Photodetachment is essentially an instantaneous process, and therefore the Franck-Condon overlap of the anion and neutral wave functions is reflected in the vertical detachment energy, which can be estimated as the maximum EBE in the photoelectron spectral profile. When there is a good Franck-Condon overlap between the lowest vibrational level of the anion (υ'') and the lowest vibrational level of its corresponding neutral (υ'), the adiabatic electron affinity of the neutral species can be extracted from the photoelectron spectrum. When the spectral profile is vibrationally resolved, the low electron binding energy threshold value of the spectrum is equal to the adiabatic electron affinity value, which corresponds to the $\upsilon'' = 0 \rightarrow \upsilon' = 0$ transition. In contrast, the determination of the adiabatic electron affinity is more approximate when the profile is unresolved. If the anions were to be cold, that is, if only $\upsilon'' = 0$ were occupied, then the electron binding energy threshold value of the spectrum would be equal to the adiabatic electron affinity value. However, anions are often generated at significant temperatures. In this case, the first few vibrational levels of the anions will be populated, leading to observed photoelectron intensities at electron binding energy values less than the adiabatic electron affinity value due to "hot bands". Lastly, if the structural difference between the anion and its corresponding neutral is large enough to preclude the significant Franck-Condon overlap at the $\upsilon'' = 0 \rightarrow \upsilon' = 0$ transition, then the adiabatic electron affinity value will lie below the low electron binding energy threshold value and no photoelectron signal will be detected. The parent negative ions were formed in a supersonic expansion nozzle-ion source. Each chiral sample was placed in the stagnation chamber of the source, heated up to $100 - 130°C$, and co-expanded with $\approx 3 - 4$ atm of argon gas through a 15μm orifice into $\approx 10^{-4}$ torr

vacuum. The negative ions were then formed by injecting low energy electrons from a hot and even more negatively biased, thoriated iridium filament into the expanding jet where the microplasma was formed in the presence of a weak external magnetic field. These anions were then extracted, and transported via a series of ion optics through the flight tube of a 90° magnetic sector mass spectrometer with a typical mass resolution of ≈ 400. The mass-selected anions of interest were then crossed with an intracavity run argon ion laser beam, and the resultant photodetached electrons were energy-analyzed in a hemispherical electron energy analyzer with a resolution of ≈ 30 meV. The photoelectron spectra reported here were all recorded with 2.54 eV photons and calibrated against the well known photoelectron spectrum of the O^-.[113]

4.4.2 Collision Induced Dissociation Technique

Collision induced dissociation (CID) was performed using an Applied Biosystems Q-star Elite triple quadrupole mass spectrometer(MS). The deprotonated anions were produced by an electrospray ionization (TurboIonSpray) source with a flow rate from 5 to 20 $\frac{ul}{min}$. The ion spray voltage was optimized empirically for each CID spectrum to give the largest deprotonated parent anion and the temperature of the source was set to 100° C. Each sample of (S)-NPNPSA and (S)-NPNPA was prepared at a concentration of 200 μg/ml in a 1:1 mixture of HPLC grade water and methanol. The instrumentation used to perform the CID experiment is outlined in the paper by Smith et al.[114] Briefly, the mass selection and CID were performed in an initial quadrupole MS and then introduced into the collision region. The ions resulting from the collision region were then analyzed by a reflectron time-of-flight MS. Energy points in all of the CID spectra were averaged for thirty seconds. Nitrogen (N2) was used as the collision gas for (S)-NPNPSA and (S)-NPNPSA/NPNPSA dimer anions while argon was used for (S)-NPNPA and I_3 anions. The lab frame energy was increased by 1 eV steps from 1 to 26 eV for (S)-NPNPSA anions, 1 to 22 eV for (S)-NPNPA anions, and 1 eV to 40 eV for the (S)-NPNPSA/NPNPSA dimer anions. All estimations of bond or cluster dissociation energies are recorded under single collision conditions. This was determined from the estimated mean free path of the ion at the pressure of 0.035 millitorr and by varying the collision gas pressure.

4.4.3 Estimation of Dissociation Energies.

$$\sigma_{total} = \sum_i \sigma_i \tag{4.1}$$

The total cross-sections were calculated using the sums of cross-sections given in Equation 1. In order to analyze the CID data the total integrated ion intensity of the parent and every product was summed to produce total ion intensity. The intensity of every ion analyzed in the spectrum was divided by the total number of ions as given in Equation 4.1.

$$I_0(E) = I_{parent}(E) + \sum I_{products}(E) \tag{4.2}$$

The total cross-section as a function of energy was determined using the Beer-Lambert law. The temperature and pressure were used to calculate the collision gas number density. The total cross-section was calculated using Equation 3.

$$I = I_0 e^{-\sigma_{total}(E)\frac{Pl}{Kt}} \tag{4.3}$$

Once the total cross-section was obtained then the cross-section for each subsequent channel can be obtained from Equation 4.

$$\sigma_i = \frac{I}{I_0} \frac{\sigma_{total}}{1 - \frac{I_{parent}}{I_0}} \tag{4.4}$$

The measured relative cross-sections for dissociation involves a complicated folding of the true cross-section with the energy distributions of the ion beam and target gas as well as the internal rotational-vibrational energy distribution of the ion. The CRUNCH program developed primarily by Armentrout-Erwin and Rodgers[115–120] 12-17 represents a convenient method for extracting energy thresholds from such experimental data. In this model, a functional cross-section was first chosen and CRUNCH has implemented multiple assumed cross section models. The one adapted for this article is based on the ansatz that energy is only transferred along the line of centers between two colliding spheres.[121] This leads to a cross-section of the form given in Equation 5 where Ea is the bond dissociation energy and E is the energy available for dissociation, including energy from internal sources above the

zero point energy.

$$\sigma_i = \frac{(E - E_a)^n}{E^m} \tag{4.5}$$

The internal energy due to rotational and vibrational contributions was determined from the density of states which is calculated using a Beyer-Swineheart-Stein-Rabinovich Algorithm.[122;123] The collision energy is a statistical quantity resulting from a Maxwell Boltzmann distribution of collision gas energies and a normal distribution of ion energies. The convolution of the ion and collision gas energy distributions was carried out using the method by Lifshitz et al.[124] The pressure and effective path-length used for all cross-section calculations were 0.035 millitorr and 21 cm, respectively. When fitting data with the CRUNCH program, there are several ways to treat the transition state used to determine the reaction rate. If an optimized transition state was available from quantum chemistry simulations then the rotational and vibrational constants obtained from the calculation can be used to calculate the reaction rate. The indication of an acceptable transition state comes from the observation of a single negative vibrational frequency in the simulation. If a transition state geometry was not available then it is possible to make a "tight" approximation in which the reactant and the transition state are treated as the same, excluding the one vibrational frequency that is relevant to the dissociation pathway and the transition state guess. A more detailed account of these approximations can be found in the review article by Armentrout et al.[120] All of the collisions were analyzed in the center-of-mass frame where it was assumed that the ion is stationary in the lab frame, which is given by Equation 6.

$$E_{c.o.m} = E_{lab}(\frac{m_2}{m_1 + m_2}) \tag{4.6}$$

4.5 Computational Methods

Computational investigations focused on characterizing both valence and dipole-bound states of the NPNPSA and NPNPA anions. These molecules are too large to use reliable ab initio methods, which are typically required for accurately predicting electron affinities, therefore more approximate methods must be used. Regarding valence states, a number of density functionals were tested first using the nitrobenzene anion, and then used to

predict the attachment energies of the analogous states of the larger "super" molecules. As for the dipole-bound states, the situation was even more challenging and for several anionic conformers we relied entirely on Koopman's Theorem (KT) and comparing trends. Three basis sets were employed: Dunning's correlation consistent double-ζ (Aug-cc-pVDZ) and triple-ζ(Aug-cc-pVTZ) sets, and Ahlrichs's redefined triple-ζ set augmented with a minimal set of diffuse functions (ma-Def2-TZVP).[125–128] For consistency, all geometry optimizations of neutral and negatively charged conformers of nitrobenzene, NPNPSA, and NPNPA were carried out using the same method, that is, the M06-2X hybrid functional26 and the Aug-cc-pVDZ basis set. The performance of different methods for computing attachment energies was then studied in detail using the 2B1 valence state of nitrobenzene as a prototype. Regarding ab initio methods, self-consistent field (SCF) calculations, second-order Moeller-Plesset perturbation theory (MP2), coupled-cluster calculations with single and double substitutions (CCSD), CCSD with a perturbative estimate of triple substitutions (CCSD(T)), and an equation-of-motion couple-cluster method for electron affinities (EOM-CCSD) were used. In the MP2 and all coupled-cluster calculations, the core electrons were frozen in their SCF orbitals. Moreover, for the open-shell valence state of the nitrobenzene anion, CCSD(T) calculations were started from unrestricted (UHF) and restricted (ROHF) SCF wavefunctions of the anion as well as from an anion-like occupation of the SCF orbitals of the respective neutral (QRHF). In terms of the density functionals, the generalized-gradient-approximation (GGA) functional BLYP, BP86, PBE, and OLYP, the meta-GGA functional TPSS, and the hybrid functionals M06-2X, B3LYP, and O3LYP were used.[62;129–134] Three program packages were employed for the study of both the valence and dipole bound anions; Gaussian09[79] for M06-2X calculations, Orca[135] for all other density functional and some of the MP2 calculations, and CFOUR[136] for MP2 and all coupled-cluster calculations.

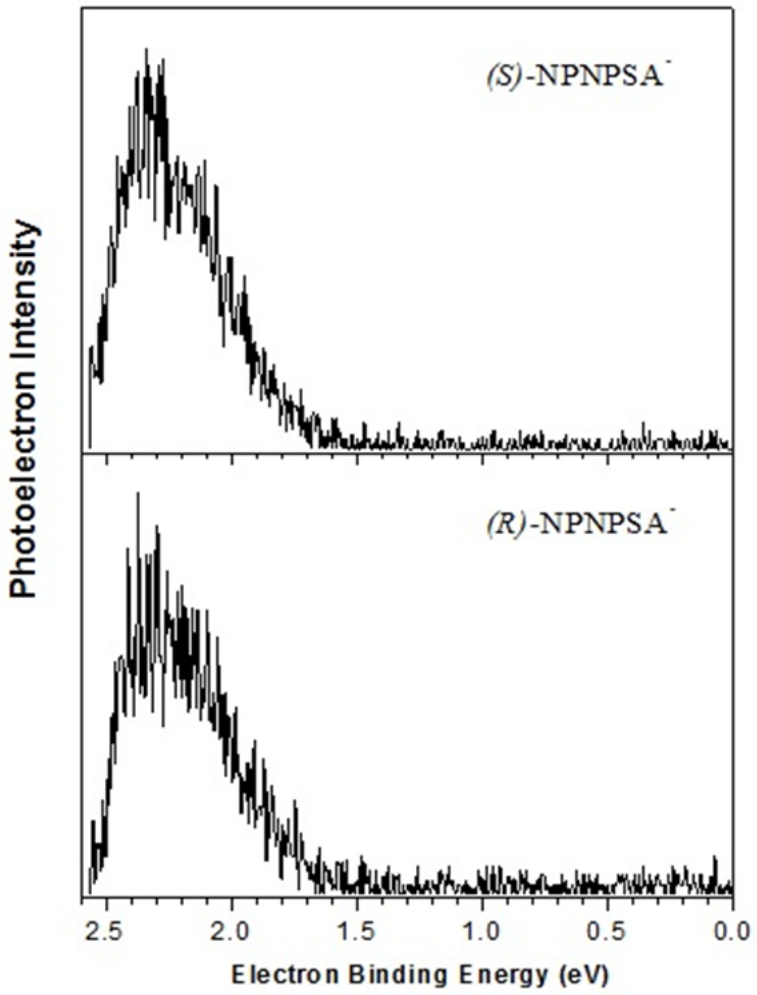

Figure 4.2: Photoelectron spectra of (S)- and (R)- NPNPSA anions recorded with 2.54 eV photons.

4.6 Experimental Results and Discussion

4.6.1 PES

The photoelectron spectra of the valence (S)- and (R)- NPNPSA anions are shown in Figure 4.2. As expected, both chiral anions exhibit very similar, if not identical, photoelectron spectral profiles as was expected. Each photoelectron spectrum of (S)- and (R)- NPNPSA anions has a maximum electron binding energy (EBE) value at ≈ 2.3 eV and a threshold EBE value at ≈ 1.7 eV. Thus, the VDEs of both chiral molecular anions are at2.3 ± 0.1 eV.

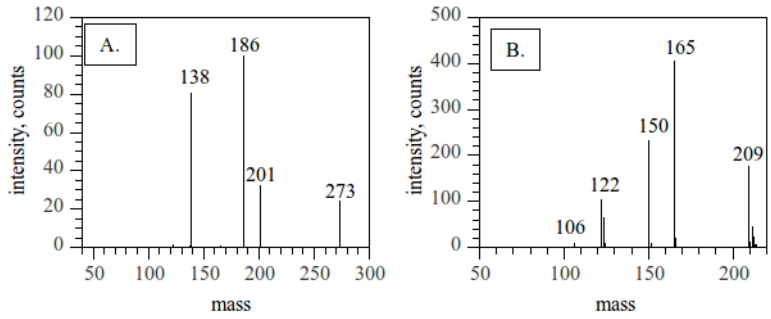

Figure 4.3: (A) Mass spectrum of (S)-NPNPSA-H after CID (B.)Mass Spectrum of (S)-NPNPA-H after CID.

Based on the location of the threshold and typical patterns of anion photoelectron spectral profiles, the AEA values of both chiral molecules are assigned as lying in the vicinity of 1.7±0.1 eV. Due most certainly to the Franck-Condon factors and large degrees of freedom for this anion, any vibrational structures in both spectra remain unresolved. Much time and effort was directed toward producing the (S)- and (R)- NPNPA anions and recording their photoelectron spectra, however, we were unable to produce parent anions of these molecules. Multiple samples were prepared and many searches with the ion source adjusted for optimum ion intensities were carried out to no avail. NPNPA has a predicted positive electron affinity of approximately 1 eV from calculations depending on the conformer. However, it is possible that the cross section for electron attachment to this molecule is too small to be produced by slow electron attachment or that the cross section peaks at higher energy. The absence of the NPNPA anion is either demonstrating some interesting physics at play or we have missed an important experimental variable.

4.6.2 CID

The secondary ion mass spectra of deprotonated (S)-NPNPSA (referred to as NPNPSA-H) and (S)-NPNPA (referred to as NPNPA-H) anions following collision induced dissociation (CID) are shown in Figure **??**.

The various fragments formed during collision with argon or N_2 as a function of the center-of-mass collision energy of NPNPSA-H and NPNPA-H are shown in Figure 4.4 and Figure 4.5, respectively. The CID data for both anions are very smooth and reproducible.

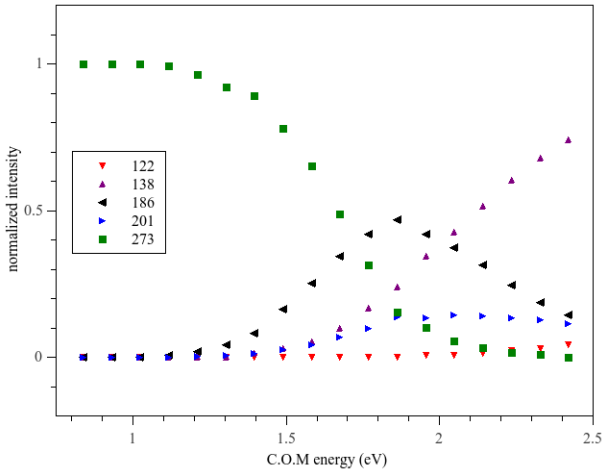

Figure 4.4: Collision induced dissociation spectrum obtained for (S)-NPNPSA-H.

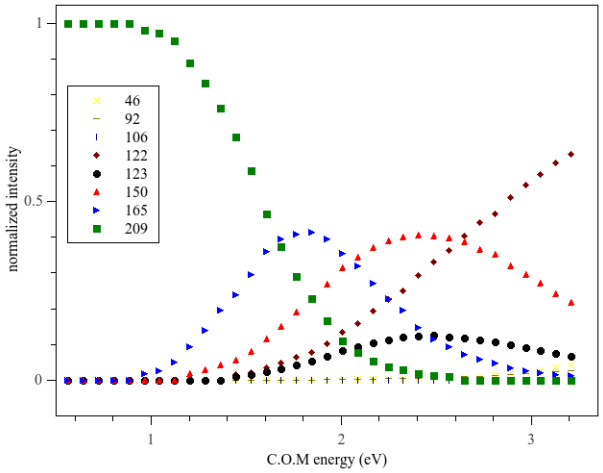

Figure 4.5: Collision induced dissociation spectrum obtained for (S)-NPNPA-H.

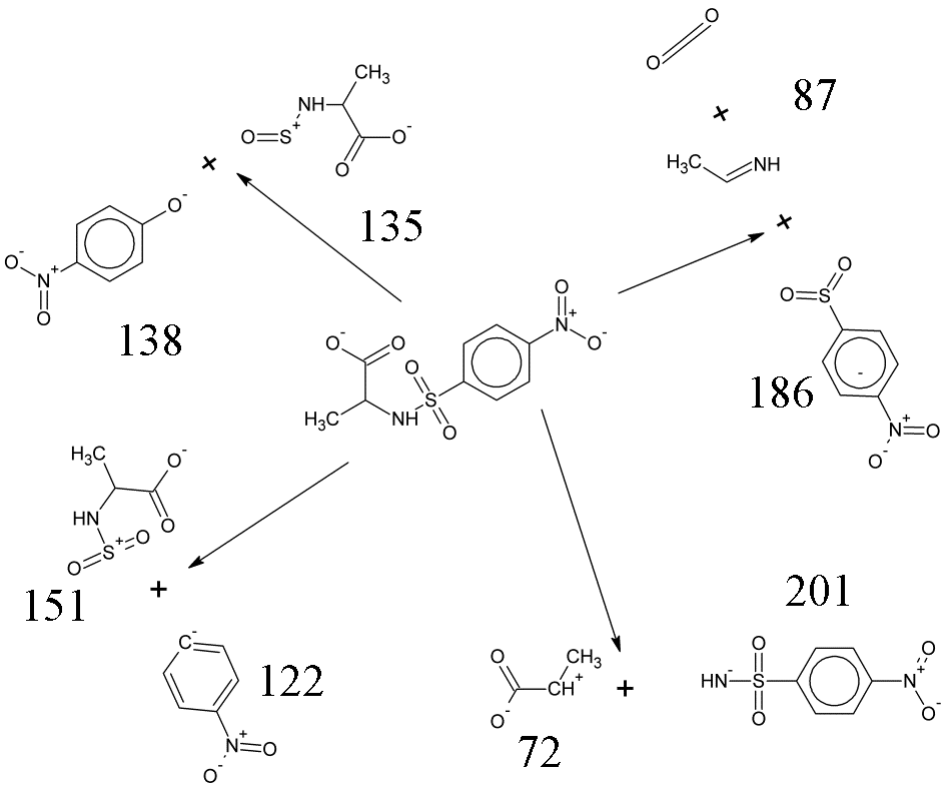

Figure 4.6: Collision induced dissociation fragmentation pathways for the NPNPSA-H anion.

The primary fragments of NPNPSA-H anions (273 amu) upon collisions with N_2 were the following: 201 amu, 186 amu, and 138 amu and to a much lesser extent 122 amu. Figure 4.6 illustrates all major fragmentation pathways of NPNPSA-H yielding these fragments. The 201 amu mass peak was produced from bond breakage between the stereocenter of alanine and the nitrogen. The 186 amu mass peak was the loss of a doubly deprotonated alanine. From the 186 amu mass fragment, a smaller 87 amu mass was determined from B3LYP/Aug-cc-pVDZ optimizations as the result of bond breakage forming acetaldimine (and CO_2).[137]

The 138 amu mass fragment, requiring a rearrangement reaction, resulted in the attachment of oxygen to nitrobenzene in place of the sulfur at the para-position, in other words forming a deprotonated nitrophenol. This was supported by geometry optimizations of the 138 amu anion and the 135 amu neutral fragment with B3LYP/Aug-cc-pVDZ. There exists the possibility that the formation of the 138 anion resulted from the attachment of

NH_2 at the para-position of the nitrobenzene. Isotopic distribution could not be used to clarify this further because of alterations caused by the mass filter, but regardless this seems unlikely considering the structure of the anion. Furthermore, pondering the alternative where NH_2 was attached does not satisfy the so called "even electron rule."[138;139] Thus the rearrangement reaction involving the loss of SO_2 is not unprecedented. Wang et al.[140]observed a similar rearrangement reaction for a biologically derived sulfonamide $\beta 3$ agonist, although they reported only the loss of SO_2. This differs in the experiments reported here-in because it is believed that the oxygen was being scavenged from SO_2. Lastly, the 122 amu mass peak observed corresponds to a deprotonated nitrobenzene anion at the para-position. This anion signal was extremely weak for NPNPSA-H but much more prevalent in the NPNPA-H case to be discussed. The primary fragments of NPNPA-H anions (209 amu) upon collisions with argon were the following: 165 amu, 150 amu, 123 amu, 122 amu, and ions of lower intensity were 106 amu, 92 amu, and 46. Figure 4.7 illustrates all major fragmentation pathways of NPNPA-H yielding these fragments. The 165 amu mass resulted from the loss of CO_2. The 150 amu mass peak most likely resulted from the loss of both CO_2 and NH coupled with a rearrangement reaction where the alanine stereocenter attached to the para-position of the nitrobenzene. This reaction thus produces an anion which satisfies the "even electron rule." Competition was observed between the 123 amu and 122 amu mass fragments. The 123 amu mass peak is a nitrobenzene anion and is therefore a doublet anion. It was dominated by the 122 amu mass peak even though they follow each other closely at lower energies and was attributed to the intact nitrobenzene anion. The 106 amu mass peak is attributed to a deprotonated nitrosobenzene anion formed by oxygen loss from the 122 amu mass fragment. The remaining smaller mass fragments at 92 amu and 46 amu are due to formation of a deprotonated phenol and $N0_2$ ions, respectively. Unfortunately, the 106 amu, 92 amu, and 46 amu mass fragments had extremely low abundance in the CID spectrum of NPNPA preventing the estimation of bond dissociation energies. It is interesting that the anions are formed through deprotonation of the carboxylic group, yet the charge was always found on the delocalized π orbitals of the nitrobenzene. The exception was for the very weak case of the NO_2 anion, whose delocalized orbitals stabilized the negative ion by reducing the repulsive columbic interactions. This was evident from the fact that the nitrobenzene unit

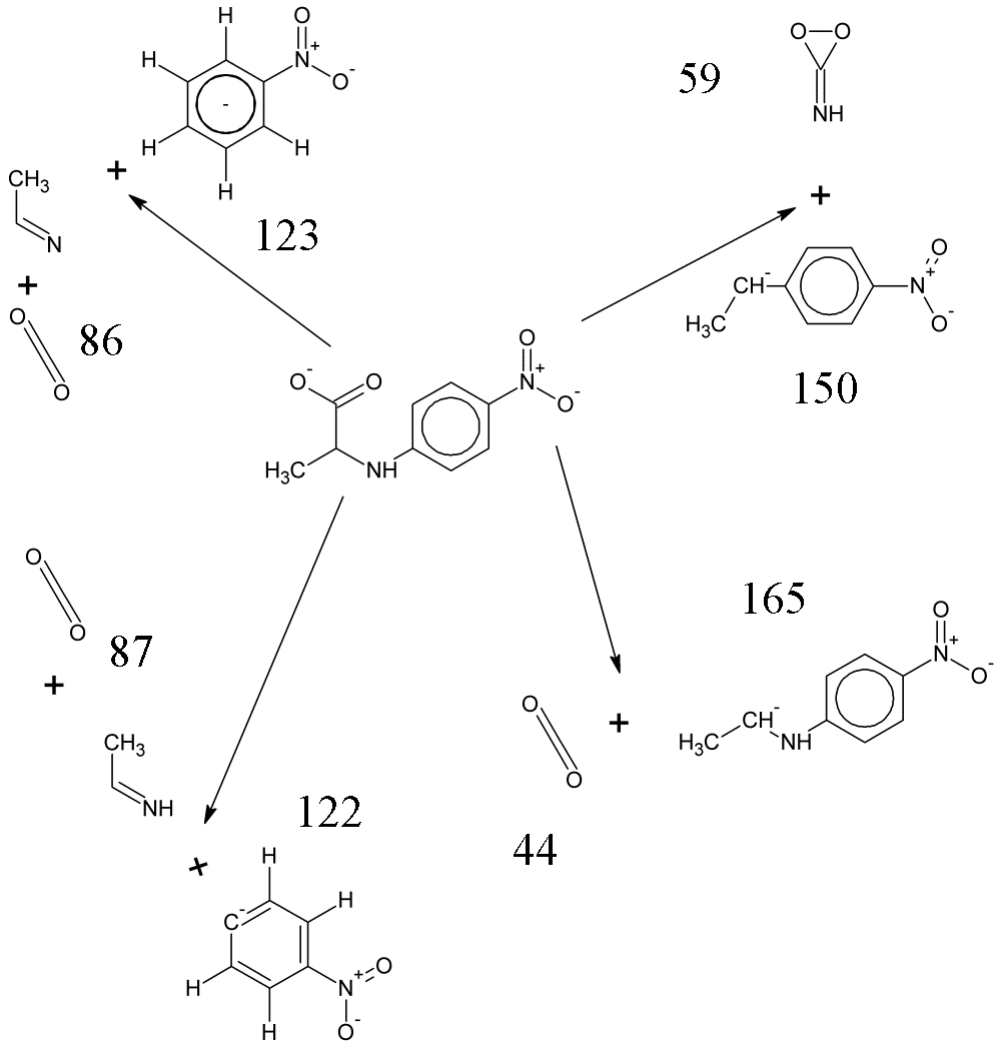

Figure 4.7: Collision induced dissociation fragmentation pathways for the NPNPA-H anion.

appeared in all the anions that were observed in these experiment, and the fact that the NO_2 anion was only observed at very low intensities in the NPNPA spectrum. We cannot rule out the possibility of the metastable CO_2 anion (44 amu) being formed and then decaying before the fragment can be detected, considering its lifetime is about 22 to 60 μsec depending on its internal energy.[141] The fragmentation pathways of NPNPSA and NPNPA showed some similarities. The 87 amu fragment with the neutral complement to the 186 amu fragment in NPNPSA and the 123 amu fragment of NPNPSA occur for both ions. The 87 amu neutral fragment for both ions was predicted to fragment into CO_2 and acetaldimine. It is interesting to note that both NPNPSA and NPNPA have a bond dissociation energy of 1.26 eV associated with the 123 amu ion and 186 amu ion, the charged counterpart of the 87 amu neutral fragment. The NPNPSA and NPNPA anions behave as expected if a comparison to para-nitroaniline (pNA) is made. The pNA anion has a rearrangement reaction followed by the loss of NO which has been measured by Smith et al. to be 2.25 ± 0.07 eV.[114] This is larger than any of the channels of NPNPA by approximately 1 eV. The loss of the NO_2 anion from pNA has a measured bond dissociation energy 3.80 ± 0.07 eV. An interesting study could be performed to measure the NO_2 anion dissociation energy as a function of the functionalization of the benzene ring. This high level of stability explains why every negative ion observed included the nitrobenzene moiety.

4.6.3 CID CRUNCH Fitting Results

The laboratory energy scale was calibrated using the known collisional dissociation energy of the triiodide anion; $I_3 \rightarrow I^- + I_2$.[142] Although Do et al. employed helium as their collision gas, the data herein was recorded using argon gas was essentially identical, except for the magnitude of the estimated cross section. Our value was larger as expected, but the model used has an adjustable scaling factor, whose differences were scaled out when fitting with CRUNCH. The dataset collected for I_3^- , as shown in Figure 4.8, was used to estimate the ion energy spreads, and the parameters obtained from the data fitting with CRUNCH are given in Table 4.1.

These thresholds obtained with CRUNCH agree well with the measurement of 1.305 ± 0.06 eV given by Do et al. RRKM theory was included in this simulation of the CID using the

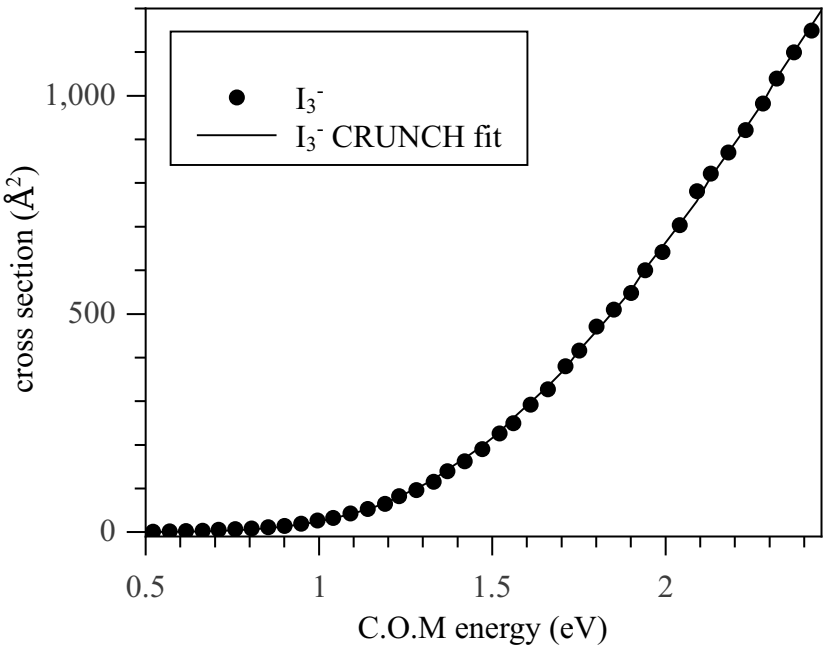

Figure 4.8: The CID of I_3^- $\rightarrow I_2+I^-$ and the corresponding fit made with the crunch program.

Table 4.1: The parameters obtained for I_3^- fitting with Crunch.

D.E.(eV)	χ^2	n
1.33[a]	0.500	1.98
1.27[b]	0.505	1.88

a. without RRKM
b. with RRKM

CRUNCH program. The I_3^- transition state was optimized using the B3LYP functional with the LANL2DZ and DGDZVP basis sets that includes an effective core potential.[143–145] The frequencies obtained from the LANL2DZ and DGDZVP simulation are listed in Table 4.2 along with the parameters obtained for the transition state structure. The vibrational frequencies for I3- were taken from Parrett et. al.[146] The NPNPSA-H and NPNPA-H dissociation energy fittings were a much more challenging endeavor because of the multiple channels available for their dissociation. Each channel was treated independently, and the fitting was performed with the cross-section model given in coupled with RRKM transition state theory. The vibrational frequencies and the rotational constants calculated using the

Table 4.2: The calculated parameters of the I_3^-.

	LANL2DZ	DGDZVP
r_{12} Å	6.88	7.28
r_{23} Å	3.05	2.88
θ	177.86	177.68
ν_1	-11	-8
ν_2	9	8
ν_3	137	156

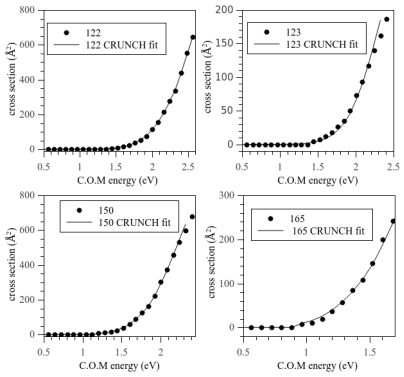

Figure 4.9: Estimated cross-section data with corresponding CRUNCH fits of NPNPA-H fragments produced using parameters listed in Table 4.12

lowest energy conformer of the deprotonated ion and simulated using the B3LYP functional with Aug-cc-pVDZ basis set. The vibrational frequencies with this functional and basis set combination were scaled by a factor of 0.9709 as recommended by Sinha et al.[147] Attempts were made at calculating the transition states but finding transition states is often not a straight forward process. The estimations for the dissociation energy values for each CID channel of NPNPA-H are listed in Table 4.3 and the corresponding fits in Crunch show good agreement with experimental results as seen in Figure 4.9.

For all dissociation pathways, a tight transition state was taken as an approximation to the real transition state. The same was repeated for each CID channel of NPNPSA-H. The dissociation energy values are listed in Table 4.4 and the CID reaction products data and corresponding CRUNCH fittings are shown in Figure 4.10. The fitting process was more challenging for this molecule, particularly for the channels with masses corresponding to 201 amu and 122 amu.

Table 4.3: The estimated bond dissociation required to produce the listed anion fragment from [NPNPA-H].

Mass	D.E.(eV)	n	σ
165	1.03 ± 0.1	0.5	1.55
150	1.15 ± 0.1	0.5	1.55
123	1.262 ± 0.1	0.5	0.65
122	1.16 ± 0.1	1.56	1.156

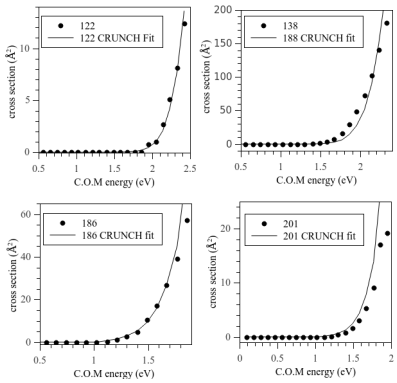

Figure 4.10: Estimated cross-section data with corresponding CRUNCH fits of NPNPSA-H fragments produced using parameters listed in Table 4.4

As a result of their small intensities the uncertainties tended to be larger for these data sets and the error estimations reflect this fact. For the NPNPSA/NPNPSA-H cluster anion, the geometry was first optimized with molecular mechanics followed by optimization using the B3LYP functional with 6-31+G(d) basis set. Because of the large cluster size and number of potential conformers, a full analysis would require copious amounts of time to calculate frequencies and optimize for all possible structures. Our prediction is that the neutral and the deprotonated anion attach to each other via hydrogen bonding between the deprotonated carboxylic end of the ion and hydrogen attached to the carboxylic moiety in the neutral. This cluster fragmented even when the collision energy was well below the binding energy of the cluster determined from the CID fitting. In fact, at low energy there was a decrease in fragmentation with increased collision energy.

I determined the cluster anion undergoes auto-detachment which combined with shorter flight times and the reaction rate of the auto-dissociation, produces a decrease in the relative product ion intensity as the collision energy increases. The CID spectrum in Figure **??** shows

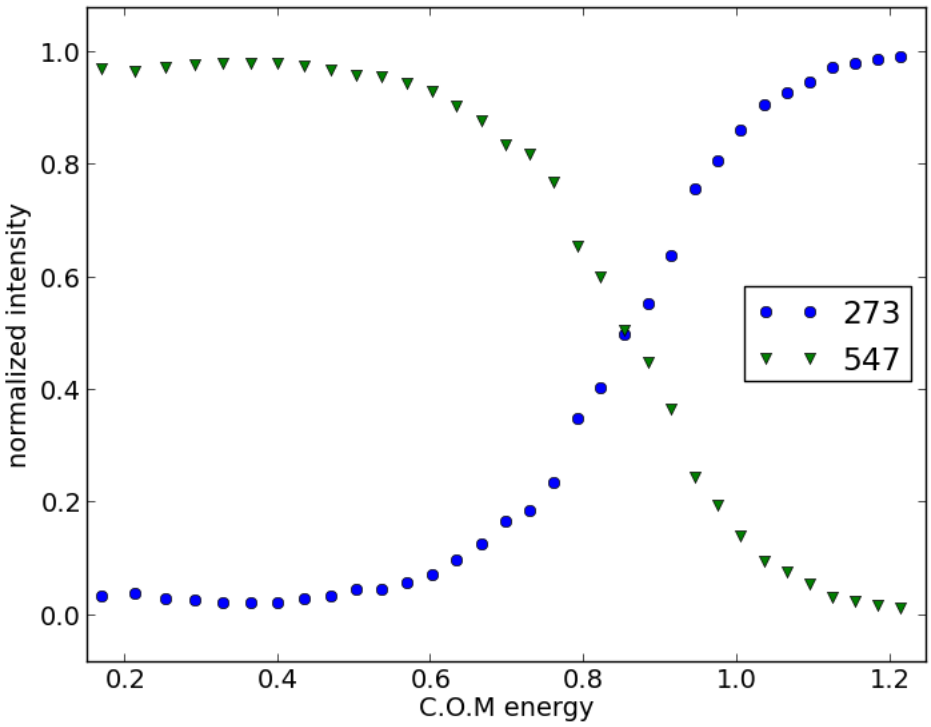

Figure 4.11: The CID spectrum of the cluster of [NPNPSA+NPNPSA-H] which yields NPNPSA-H.

Table 4.4: The estimated bond dissociation required to produce the listed anion fragment from [NPNPSA-H] ion and the cluster.

Mass	D.E. (eV)	n	σ
201	1.17 ± 0.21	0.41	0.928
186	1.26 ± 0.1	0.156	13.59
138	1.30 ± 0.1	0.259	4.559
122	1.53 ± 0.21	1.094	12.6
273[a]	0.32 ± 0.08	2.74	7.32

a.)Results obtained for the cluster.

this for energies between 0 and 1.4 eV. Still, we were able to fit the data with CRUNCH and find an estimate of the bond dissociation for this cluster. The results of this fit are shown in Figure 4.12.

4.7 Computational Results and Discussion

DFT simulations were used to assist in the CID analysis, particularly in determining the stable structures of the fragments as well as the minimum structure of the deprotonated anions and determining the vibrational frequencies and rotational constants used to calculate reaction rates. The optimized structure and frequencies of NPNPA and NPNPSA and their fragments were calculated using B3LYP/Aug-cc-pVDZ. Frequencies were included to account for the zero-point vibrational energy. The DFT calculations predicted the loss of a CO_2 from the 87 amu fragment of NPNPSA, and the 86 amu, and 87 amu fragment of NPNPA. Two of the fragmentation pathways of NPNPSA have a negative ΔG and ΔH calculated at 300K, implying that the fragments are more stable than the deprotonated ion. The ΔG and ΔH resulting from these calculations are shown in Table 4.6 and Table 4.5. The pathways accounting for each mass fragment in the CID spectra of NPNPA and NPNPSA are shown in Figure 4.7 and Figure 4.6.

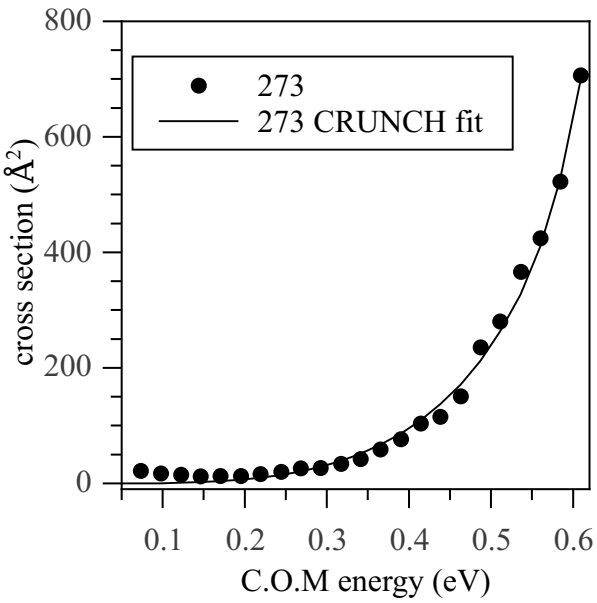

Figure 4.12: The CID spectrum of the cluster of [NPNPSA+NPNPSA-H] which yields NPNPSA-H.

Table 4.5: Calculated Changes in Gibbs Free Energy (ΔG) and Enthalpy (ΔH) of NPNPSA-H with B3LYP/Aug-cc-pVDZ, Including Vibrational Corrections

Products	ΔG (eV)	ΔH (eV)
$273 \rightarrow 201 + 72$	1.52	2.05
$273 \rightarrow 186 + 44 + 43$	-0.53	-1.57
$273 \rightarrow 138 + 135$	-1.06	-0.54
$273 \rightarrow 122 + 151$	3.2	3.73

4.7.1 DFT performance for the valence state of nitrobenzene

The first focus was the valence state, that is, the 2B1 state of nitrobenzene. Nitrobenzene is a useful reference system, because both NPNPSA and NPNPA have analogous states that form the same type of anions with the excess electron being localized essentially on the nitrobenzene moiety. Also, the experimental AEA of nitrobenzene is well known from experiment (1.00 eV[104]). For validation purposes, the AEA value without zero-point corrections is more useful, even though the experimental result of reference 1 includes zero-point effects. To obtain an "experimental" value without zero-point effects, the zero-point

Table 4.6: Calculated Changes in Gibbs Free Energy (ΔG) and Enthalpy (ΔH) of NPNPA-H with B3LYP/Aug-cc-pVDZ, Including Vibrational Corrections

Products	ΔG (eV)	ΔH (eV)
$209 \rightarrow 165 + 44$	1.43	1.92
$209 \rightarrow 150 + 59$	4.21	4.92
$209 \rightarrow 123 + 42 + 44$	1.53	2.58
$209 \rightarrow 122 + 43 + 44$	1.95	2.97

correction of the AEA of nitrobenzene was computed using three density functionals, M06-2X, B3LYP, and TPSS, with the Aug-cc-pVDZ basis set. The three functionals agreed with each other reasonably well and yielded corrections of 84, 71, and 73 meV, respectively. Therefore, the "experimental" value for the uncorrected AEA should be close to 0.92 eV. The first set of methods considered was the standard sequence of ab initio methods: SCF, MP2 and coupled-cluster based methods (see Table 4.7). Unfortunately, the UHF wave function for the anion showed a large spin-contamination, so that neither ΔSCF nor ΔMP2 are expected to yield useful results, which was indeed the case. Coupled cluster calculations are known to be able to recover from spin contamination in the reference wavefunction. Thus, UHF-based CCSD(T) calculations yielded results much more reasonable than UHF or UHF-based MP2. Yet, CCSD(T) calculations started from a ROHF reference (ROHF-CCSD(T)), or from a reference constructed using the orbitals of the neutral (QRHF-CCSD(T)) yielded virtually identical results, which were quite a bit higher than the UHF based coupled-cluster results (≈70 meV). This suggests that in this case, recovery from spin-contamination was not complete. Another test was a direct computation of the electron affinity with the EOM-CCSD method, which resulted in close agreement with ROHF-based ΔCCSD(T). Regarding basis sets effects, the coupled cluster values followed the usual trend that the experimental value was approached from below as the basis set quality increases. This behavior reflects that there is more electron correlation in the anion than there is in the neutral, and better basis sets will yield a larger energy difference. With the Aug-cc- pVDZ basis set, the result was about 0.1 eV too low; with the Aug-cc-pVTZ set, this result was less than 50 meV too low. Therefore, the CCSD(T) calculations clearly converge to the experimental value of 0.92 eV in a systematic manner. Based on this finding for the AEA, the ROHF-based

Table 4.7: DFT Calculations for the EBEs (in meV) of the Valence State of Nitrobenzene

	Aug-pVDZ		Aug-pVTZ			
	VAE	VDE	AEA	VAE	VDE	AEA
SCF	0.31	1.33				
MP2	-0.81	-0.25				
UHF-CCSD	0.33	1.08			1.21	
UHF-CCSD(T)	0.26	0.92	0.77		1.05	0.81
ROHF-CCSD(T)	0.31	0.98	0.83	0.45	1.12	0.88
ORHF-CCSD(T)	0.31	0.98	0.83			
EOM-CCSD	0.25	0.95	0.79	0.42	1.12	0.88
M06-2x	0.7	1.44	1.08	0.78	1.53	1.12
B3LYP	0.69	1.33	1.12	0.71	1.35	1.08
O3LYP	0.73	1.34	1.05	0.75	1.36	1.03
BLYP	0.65	1.2	1.15	0.63	1.19	1.08
BP86	0.84	1.4	1.30	0.83	1.39	1.23
PBE	0.76	1.31	1.19	0.75	1.30	1.13
OLYP	0.57	1.13	0.97	0.57	1.12	0.92
TPSS	0.66	1.23	1.12	0.65	1.23	1.06

CCSD(T) and EOM-CCSD values for the VDE and VEA were also expected to represent good guidelines for the validation of density functional methods. Eight different density functionals (i.e., the M06-2X, B3LYP, and O3LYP hybrid functionals, the less expensive meta-GGA functional TPSS, and the GGA functionals BLYP, BP86, PBE, and OLYP) were used to compute the VEA, VDE, and AEA of nitrobenzene as shown in Table 4.7. Considering the AEA, all functionals systematically over-bind the electron including the most advanced functional used, M06-2X, performing the worst in regards to predicting the respective detachment and attachment energies. All density functional methods shown, even the Aug-cc-pVTZ set, approached the experimental value from above as the basis set was expanded, and most did over-bind the electron by more than 0.1 eV. The exception was the OLYP GGA, which yielded an AEA in perfect agreement with the experimental AEA when using the Aug-cc-pVTZ basis set. However, the situation was worse in calculating the VDE and even moreso for the VAE. The formally more reliable hybrid functionals tended to over-bind the electron by 0.3 eV or more, while the GGAs did not show a clear trend. Particularly, the OLYP and to some extent the BLYP and TPSS functionals, performed

significantly better than the hybrid functionals, a trend that has been noticed before.36 However, even these three functionals significantly overestimated the VAE of the 2B1 state. Because the density functional results tended to be less dependent on diffuse functions than the ab initio methods,[148] particularly for GGAs, an alternative triple-*zeta* basis set with only minimal augmentation was investigated. Indeed using the ma-Def2-TZVP set yielded results in very close agreement with the Aug-cc-pVTZ results for both the OLYP and TPSS functional. In conclusion, for systems larger than nitrobenzene, CCSD(T) or EOM-CCSD are not practical even with the comparatively modest Aug-cc-pVDZ set, and owing to the spin-contamination in the SCF calculation for the anion, MP2 is not an alternative either. Regarding the geometry optimizations, hybrid functionals such as B3LYP, or better M06-2X, are expected to be the best tradeoff between reliability and computational cost. However, our results show that these functionals are not the best choice for predicting electron attachment energies, but that the OLYP GGA functional, and to some extend the TPSS and BLYP functionals, yield results in better agreement with CCSD(T) and the experimental values. Based on our results, one may expect that for systems similar to nitrobenzene, their AEAs will be well reproduced by these GGAs if triple-ζ basis sets are employed, while VDEs and VEAs are expected to be overestimated by a few tenths on an eV.

4.7.2 Dipole-bound state of nitrobenzene as a reference

Computing attachment energies associated with dipole-bound states is far more challenging than those with valence states. Large sets of additional diffuse functions are needed, and saturating the basis set in this respect is crucially important. Secondly, DFT methods cannot be used in the same straightforward way as for valence bound states. On the one hand, dipole-bound states are very diffuse, and therefore the long-range part of the functional must be free of electron self-interaction, so that the asymptotic electron-molecule interaction is correct. This is a principle problem, and uncorrected functionals such as B3LYP will give infinite binding energies in the complete basis set limit. However, there is the practical problem of choosing a suitable integration grid if the basis set contains Gaussian functions with very small exponents. In fact, in many programs, it becomes practically impossible to reach convergence for the Kohn-Sham iterations if three or four sets

Table 4.8: Calculations for the VEAs (in meV) of the Dipole-Bound State of Nitrobenzene

	Aug-cc-pVDZ+6s6p5d	Aug-cc-pVTZ+6s6p5d
KT	6.4	6.3
SCF	7.1	
MP2	8.9	
CCSD	16.6	
CCSD(T)	15.6	
EOM-MP2	29.9	
EOM-CCSD	23.5	24.6

of progressively more diffuse functions are added to the basis set. Third, the attachment energies of dipole-bound states are very sensitive to long-range electron correlations effects, and reliable results often require CCSD(T) calculations with large basis sets. Nitrobenzene is to some extent a typical case. The VEA of the dipole-bound state nitrobenzene is small (i.e., in the order of 15 meV), and the Koopmans's Theorem approximation as well as ΔSCF and ΔMP2 significantly underestimate it (see Table 4.8). The often reliable direct methods, EOM-MP2 and EOM-CCSD, overestimated the VEA while ΔMP2 underestimated, making nitrobenzene a particular challenging case. For larger systems such as NPNPSA or NPNPA, computing VEAs with CCSD(T) and triple-ζ basis sets is clearly out of question. The best approach to use was KT and ΔMP2, and comparing these values to nitrobenzene for trends.

4.7.3 Results for dipole-bound and valence states of NPNPSA

NPNPSA has conformational flexibility around the single bonds of the alanine side-chain, the N-S bond and the C-S bond, and one may expect several conformers with significant populations at room temperature. A manual conformer search yielded four minimal energy configurations, which mainly differ in the orientation of the carboxyl group with respect to the rest of the molecule. We are confident that these four conformers represent all low-energy classes of conformers of neutral NPNPSA, as shown in Figure 5.2. Conformer 1 has an internal hydrogen bond between the acidic proton and the N atom; conformer 2 represents a "stretched-out" structure without an internal hydrogen bond; and conformers 3 and 4 show internal H-OS hydrogen bonds. Regarding the neutral molecule, the stretched conformer

Table 4.9: Relative Energies of Neutral NPNPSA Conformers 1, 2, 3, and 4 Using M06-2X/Aug-cc-pVDZ Method to Locate Minimal-Energy Structures

Conformer (Neutral)	M06-2X Energy (kJ/mol)	MP2 Energy (kJ/mol)
1	21.6	19.8
2	0	0
3	13.1	13.2
4	9.3	9.1

Table 4.10: Relative Energies of NPNPSA Anion Conformers 1^-, 2^-, 3^-, and 4^- Using M06-2X/Aug-cc-pVDZ Method to Locate Minimal-Energy Structures

Conformer (Anion)	M06-2X Energy (kJ/mol)
1^-	21.6
2^-	29.5
3^-	4.5
4^-	0

2 was the most stable. Conformers 3 and 4 were about 10 kJ/mol higher in energy, and conformer 1 was about 20 kJ/mol higher in energy (see Table 4.9). The predicted energetic order was independent of whether M06-2X or MP2 energies are compared, and in fact, both methods yielded very similar relative energies. All conformers attached an electron into valence states similar to the 2B1 state of nitrobenzene without any drastic change to the minimal-energy configurations. However, the energetic order changed dramatically upon anion formation (see Table 4.10).

For the valence anions conformers 3^- and 4^- (see Figure 4.13), which show a C-H-S hydrogen bond, were the most stable. Conformer 1^- is 20 kJ/mol higher in energy, and the anion formed from conformer 2, the most stable neutral conformer is almost 30 kJ/mol less stable than conformer 4^-. Clearly, the intramolecular hydrogen bonds help to stabilize the negative charge, and a hydrogen bond to the oxygen atoms of the sulfonyl group helps even more than a hydrogen bond to the N atom of alanine.

This is in contrast to NPNPA, in which we did not find any anion conformation with the acid hydrogen pointing towards the nitrobenzene ring (see discussion below); the sulfonyl group appears to prevent this type of anion conformation from forming. Following the calibrations with nitrobenzene, the adiabatic electron detachment energies of the four anion

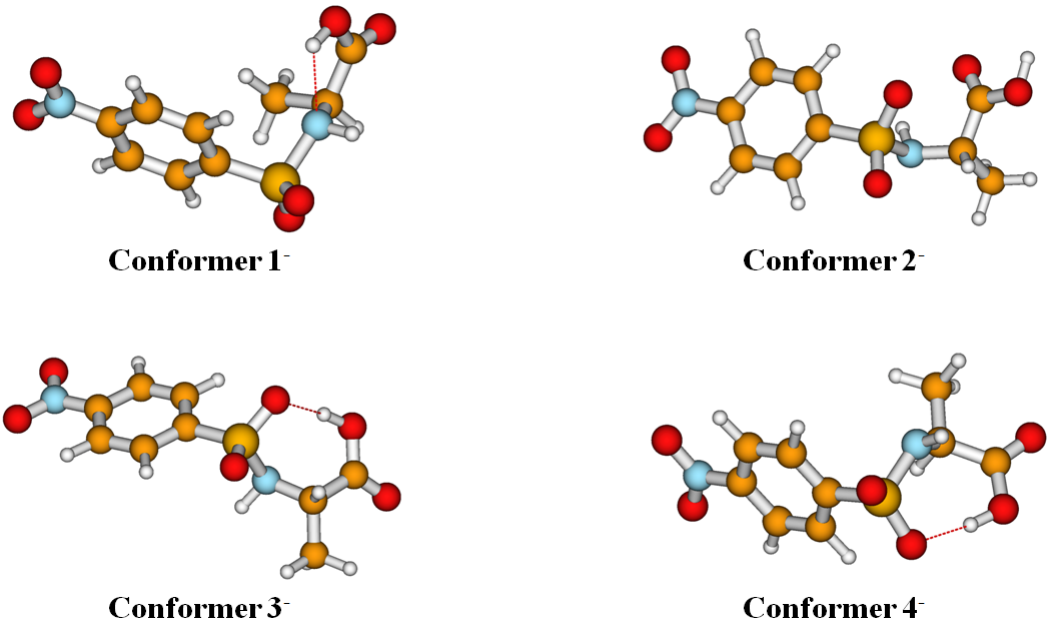

Figure 4.13: Four low-energy classes of the valence anion NPNPSA conformers.

conformers of NPNPSA were computed using OLYP/ma-Def2-TZVP energy differences at the M06-2X/Aug-cc-pVDZ minimal-energy geometries. The energy differences between related conformers of the neutral and the anion, that is, the energy difference between a conformer of the anion and the neutral conformer closest in nuclear coordinate space are displayed in Table 4.10. Adiabatic electron loss is considered to occur with small adjustments of the geometry, but not with substantial changes of conformation. This is the AEA relevant for interpreting photoelectron spectra, because only detachment to the nearest conformer is expected to have favorable Franck-Condon factors. The true AEA is the energy difference between neutral conformer 2 (the most stable neutral NPNPSA conformer) and anion conformer 4^- (the most stable NPNPSA- anion), and is 1.87 eV. All conformers with intramolecular hydrogen bonds show similar AEAs and VDEs, with the AEAs being somewhat above 2.0 eV and VDEs falling into the 2.3 to 2.4 eV range. All values listed are not corrected for zero-point effects, but similar to nitrobenzene, zero-point corrections are in the order of 0.1 eV. The corresponding values for conformer 2^- are somewhat lower in line with the missing hydrogen bond stabilization of the negative charge. Assuming that the anion population in the experiment consists essentially of conformers 3 and 4, and taking into account zero-point corrections somewhat above 0.1 eV, the calculations predict an AEA

in the order of 1.9 eV and a VDE of 2.3 eV. We note that the AEAs have also been computed from the M06-2X energies, and similar to nitrobenzene, the results are roughly 0.2 eV higher than the OLYP AEAs. Regarding dipole-bound states, most conformers of the NPNPSA anion unfortunately require methods that we cannot apply due to its size. The reason is that at the geometry of the neutral for all conformers with intramolecular hydrogen bonds, the dipole-bound state is very close to the valence state, and the two states are found to be heavily mixed with each other. Unraveling the two states requires: a reliable direct method, such as EOM-CCSD, to describe both the dipole-bound and the valence state in a balanced manner and compute both states even at geometries where they mix strongly, and one needs to follow the two states to geometries where they are well separated, so that diabatic states can be constructed. Only the valence state of conformer 2 appears to be sufficiently high in energy so that the dipole-bound state can be clearly identified. Conformer 2 has a dipole moment of 4.5 D (M06-2X/Aug-cc-pVDZ), and the VEA is predicted to be 8.1, 9.4 and 19.9 meV at the KT, ΔSCF, and ΔMP2 levels of theory, in which the Aug-cc-pVDZ set augmented with the 6s6p5d set has been used. The ΔMP2 result is about twice the VEA predicted for nitrobenzene with the same method. Again, using nitrobenzene as a guide, one may expect conformer 2 to have a dipole- bound state with an EBE of about 30 meV.

4.7.4 Results for dipole-bound and valence states of NPNPA

NPNPA has conformational flexibility around the single bonds of the alanine side-chain, and one may expect several neutral NPNPA conformers with significant populations at room temperature. A manual search yielded six minima, and we are confident that these six conformers represent all low-energy classes of conformers of the neutral (see Figure 5.1). Conformer 1 has a stretched out alanine unit and shows no internal hydrogen bond as a neutral or as a valence anion. Conformers 4 and 5 show no internal H-bond as neutrals, but in the anion, the OH bond of the acid group points towards the phenyl ring where the excess electron is largely localized. Conformers 2, 3, and 6 have internal H-bonds with the OH bond of the acid group pointing towards the amine N atom. Relative energies of the neutral conformers at their M06-2X/Aug-cc-pVDZ geometries are compared in Table 12.

Table 4.11: Relative Energies of NPNPSA Anion Conformers 1^-, 2^-, 3^-, and 4^- Using M06-2X/Aug-cc-pVDZ Method to Locate Minimal-Energy Structures

Conformer (Neutral)	M06-2X Energy (kJ/mol)	MP2 Energy (kJ/mol)
1	0	0
2	36.9	30.6
3	10.9	2.7
4	28.5	22
5	41.3	36.6
6	16.8	9

Table 4.12: Relative Energies of NPNPSA Anion Conformers 1^-, 2^-, 3^-,4^-,5^-,and 6^- Using M06-2X/Aug-cc-pVDZ Method to Locate Minimal-Energy Structures

Conformer (Anion)	M06-2X Energy (kJ/mol)
1^-	28.1
2^-	6.3
3^-	0
4^-	13.3
5^-	32.7
6^-	6.6

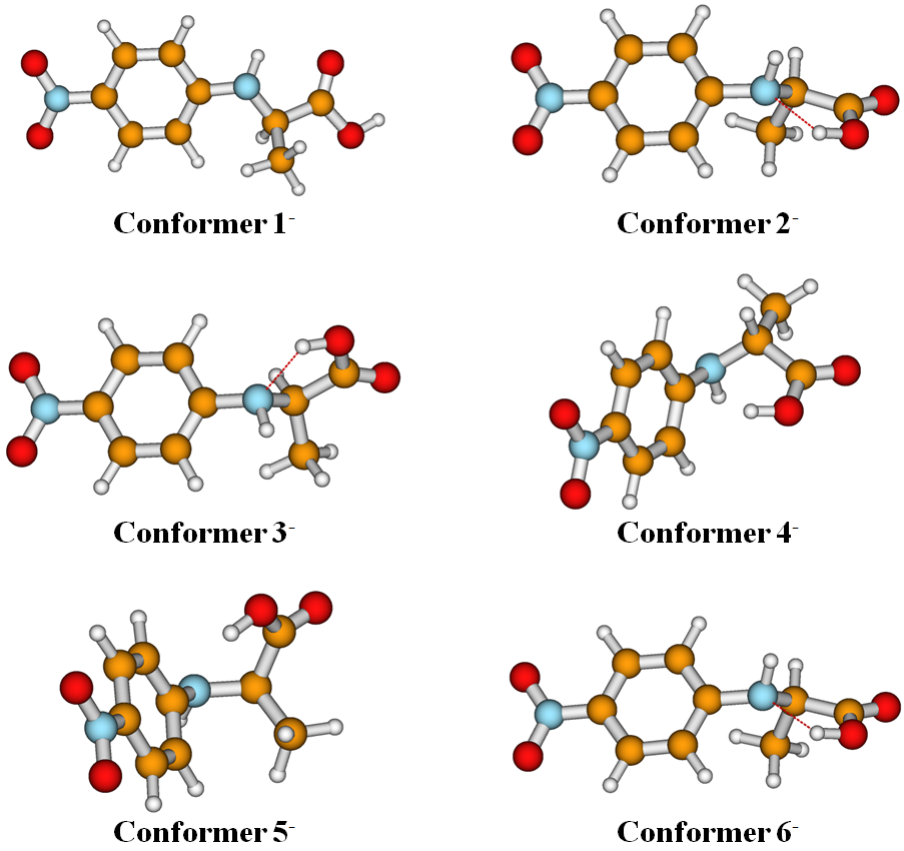

Figure 4.14: Six low-energy classes of the valence anion NPNPA conformers.

The DFT and MP2 trends are similar; however, using MP2, the energy differences between the different conformers are smaller. The stretched conformer 1 is the most stable, yet at room temperature one may expect significant populations of conformers 3 and 6 as well. Similar to NPNPSA, attaching an excess electron to a valence orbital of NPNPA changes the energetic ordering of the conformers. For the anions, those conformers (see Figure 4.14) with the OH bond pointing at the phenyl ring (conformers 2-, 3-, and 6-) are significantly more stable than the other anionic conformers (see Table 4.11). This reflects the stabilization of the excess electron, which is largely localized on the phenyl ring and the nitro group, by the OH bond dipole. Thus, at least three conformers of the NPNPA anion significantly contribute to an equilibrium population at room temperature. The AEA of the different anionic conformers are listed in Table 4.10, and are associated with a specific conformer pair, that is, the energy difference between a conformer of the anion and its closest neutral conformer in nuclear coordinate space. This is the AEA relevant

Table 4.13: Dipole Moments(Debye) and Vertical Attachment energies(meV) of the Dipole-Bound States of the Neutral NPNPA Conformers Optimized at the M06-2X/Aug-cc-pVDZ Geometries and Further Augmented Using the Aug-cc-pVDZ + 6s6p5s Set.

Conformer	Dip. Mom. (D)	KT-VEA	SCF-VEA	MP2-VEA
1	7.6	20	22.6	36.5
2	2.9	2	2.4	11.2
3	7	54.2	67.3	106.6
4	8.5	58.6	70.4	111.5
5	8.5	58.7	68.6	103.1
6	6.9	65	84.4	141.3

for interpreting the NPNPA photoelectron spectrum if one was obtained, because one may expect appreciable Franck-Condon factors only for transitions to the nearest conformer of the neutral. This AEA is 1.08 eV and represents the energy difference between neutral conformer 1 and anion conformer 3^-. Apart from conformer 1^-, the AEAs and VDEs show the same order of magnitude with AEAs between 1.05 and 1.25 eV, and VDEs between 1.4 and 1.7 eV. The values listed in the table have not been corrected for zero-point effects, but similar to nitrobenzene, zero-point corrections are on the order of 0.1 eV. According to their relative energies, conformers 2^-, 3^-, and 6^- should have significant abundance in an experimental populations, and because these three conformers have significantly differing AEAs and VDEs, therefore substantial inhomogeneous broadening may be expected for the photoelectron spectra of NPNPA. The predicted range for the VDE is 1.3 to 1.4 eV, and for the AEA it is 0.9 to 1.1 eV.

Lastly, the dipole moments and the VEAs associated with dipole-bound states have been computed at the M06-2X geometries of the different conformers. Koopmans's Theorem, the SCF, and the MP2 methods were used with the Aug-cc-pVDZ set further augmented with a 6s6p5s set centered at the center of mass of the molecule as described above (see Table 4.13). In a previous study of nitrobenzene anions both dipole and valence anions were reported but the dipole bound anion once formed spends most of its time in the valence anion (i.e., on the NO_2 end of the molecular anion).[104] Apart from conformer 2, all conformers show substantial dipole moments in excess of 6 D, and the associated VEAs are substantially larger than that of nitrobenzene. All values follow the usual trend that KT and SCF yield considerably

lower VDEs than MP2. Provided that the results for nitrobenzene can serve as guidance, the experimental value can be expected to be about 50% larger than the listed MP2 results. There are some interesting differences between conformer 1 and conformers 3, 4, 5, and 6 in the sense that despite similar, fairly large dipole moments, the predicted VEAs differ by as much as a factor of 3. These differences can be explained by different interactions between local bond-moments and excluded volume effects. As an example, consider the dipole-bound orbitals in Figure 4.15.

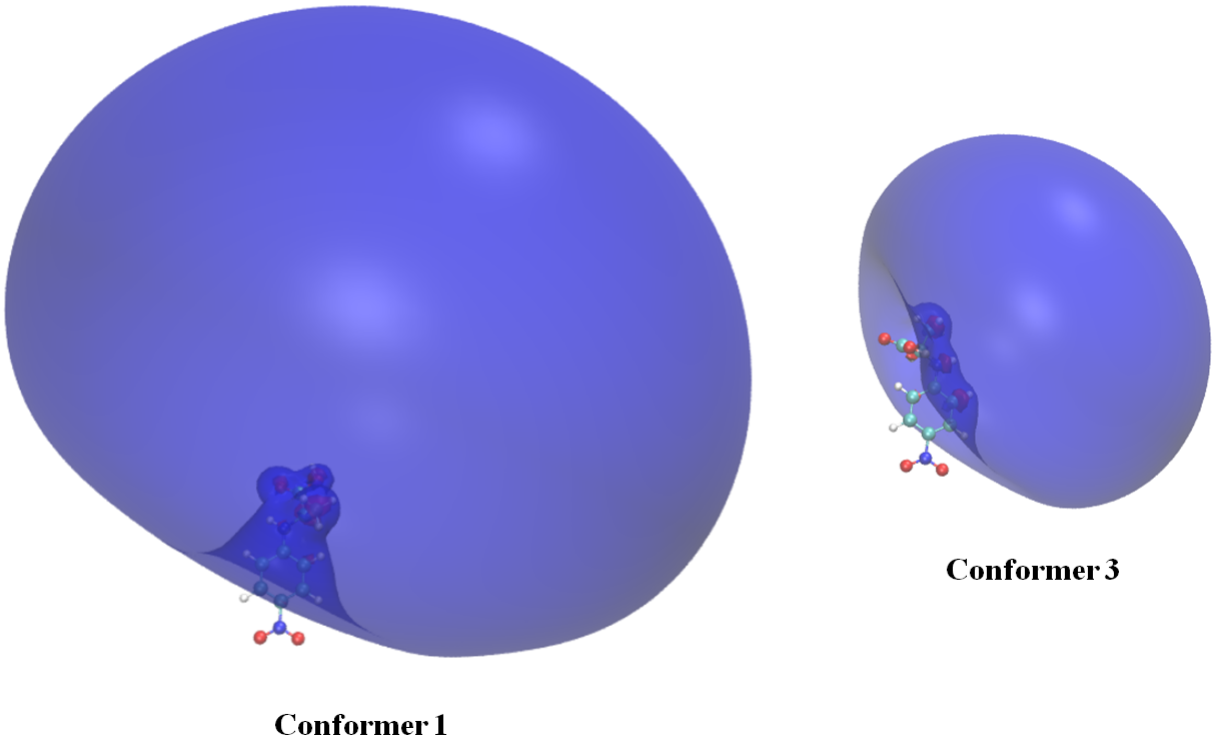

Figure 4.15: Dipole-bound orbitals of NPNPA Conformers 1 and 3. The iso-surfaces shown enclose 75% of the electron density, which corresponds to iso-contour values of 0.0010 and 0.0022, respectively. The associated electron binding energies are listed in Table 4.13.

The essential local dipole-moments stem from the NO_2 and from the carbonyl group, and the phenyl ring creating an excluded volume, that is, a region where the attractive potential due to the NO_2 group is strong, but the electron can nevertheless not be owing to Pauli repulsion with the valence electrons. The relative orientation of these three groups is such that the excess electron can be closer to both local dipoles in conformer 3^-, which is reflected in a larger EBE and a more compact distribution of the excess electron.

4.8 Conclusion

The negative ion properties of two extended molecular structures, N-paranitrophenylsulfonylalanine (NPNPSA) and N-paranitrophenylalanine (NPNPA) were examined both experimentally and theoretically. The calculated electron affinity was in good agreement with the measured valence adiabatic electron affinity of 1.7 ± 0.1 eV for NPNPSA. This value is almost twice that for nitrobenzene showing the effect of the extended system. The experimental and theoretical agreement for (S)- and (R)- NPNPSA as well as that of nitrobenzene provides confidence for at least the predicted electron affinity of the NPNPA conformers. Also, the vertical detachment energy of NPNPSA negative ion was measured to be approximately 2.3 pm 0.1 eV which compares quite well with the calculated VDE of 2.32 eV. The predicted dipole moments of NPNPSA and NPNPA for the most dominant conformers were 4.5 D and 7.6 D, respectively, and the dipole bound electron affinities are predicted in the range of 8.8 to 19.9 meV for NPNPSA and 20 to 36.5 meV for NPNPA (see Table 12). In our previous study of nitrobenzene anions[104] both dipole and valence anions were reported. However, it is argued from the data that the dipole bound state represented a "doorway state" to the more stable valence anion. Once formed, the anion spends most of its time in the valence anion localized on the NO_2 end of the molecular anion. This is very likely the situation for the polar molecules studied here. The bond dissociation energies for NPNPSA-H, NPNPA-H, and a cluster formed by a deprotonated NPNPSA with a neutral NPNPSA were determined using a CID experiment coupled with the fitting program CRUNCH resulting primarily from the work of Armentrout, Erwin, and Rogers.[115–120;124;149? –151] The energy scale and ion beam energy distribution was determined using the previous results for the I_3^- anion of Do et. al.[142] The dissociation parameters were estimated with the inclusion of RRKM theory for

NPNPSA-H and NPNPA-H. Every ion channel, excluding the very weak channels of the $N0_2$ anion and a nitrosobenzene ion lacking hydrogen at the para-position, contained the nitrobenzene moiety even though the anions were created via a deprotonation of a carboxylic acid. This is due to the stabilizing effect of the delocalization of the excess electron on the π orbitals of the nitrobenzene molecule.

Chapter 5

Experimental and Computational Study of the ORD and ECD of N-paranitrophenylsulfonylalanine and N-paranitrophenylalanine

5.1 introduction

In Chapter 4 a study of the negative ion properties of the newly synthesized molecules N-paranitrophenylsulfonylalanine and N-paranitrophenylalanine was presented. In this chapter, the UV/Vis, circular dichroism, and optical rotatory dispersion of both molecules are experimentally obtained and then compared to calculated spectra with the goal of establishing the absolute configuration. These molecules, shown in Figures 5.1 and 5.2, are molecules that have the chiral center in the so called "third sphere".[152] This means that the chiral center is not part of the cyclic structure of the nitrobenzene chromophore(1st sphere) or directly connected to the nitrobenzene chromophore(2nd sphere).* The nitrobenzene chromophore in both molecules is for all intensive purposes planar with the alanine moiety acting as a source of the chiral perturbation. ORD represents a relatively straight forward

*for further explanation see Berova et al.

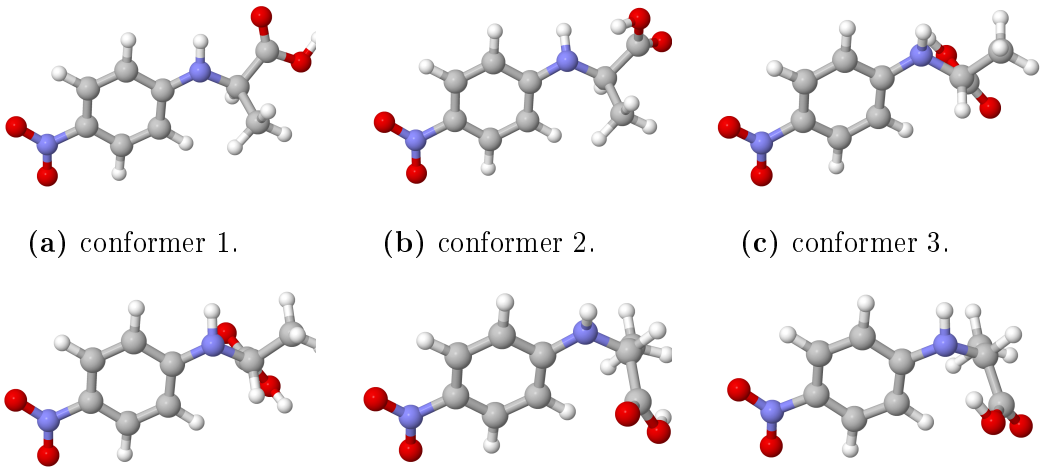

(a) conformer 1. **(b)** conformer 2. **(c)** conformer 3.

(d) conformer 4. **(e)** conformer 5. **(f)** conformer 6.

Figure 5.1: The conformers of *R*-NPNPA.

chiro optical property that has had limited utility for for determining of the absolute configuration of chiral molecules. Before the development of modern computers the optical rotation was used in a limited capacity to determine the absolute configuration using empirical rules. A thorough account of these methods can be found in the cited articles by Polavarapu *et. al.*[18;153] The combination of increased computational speed and advances in computational chemistry now allow the calculation of ORD for of small and medium sized molecules with great ease for some cases.[154] However in some cases the calculated ORD disagrees with the sign of the data determined by experiment (see Chapter 2). A comparison of the sign of theoretical and experimental ECD and ORD is seen as the litmus test for the accuracy of the chosen computational approach. A sign disagreement can be the result of several possible factors. In most cases the optical rotation measurements are recorded in solution or as a neat liquid. The choice of solvent effects may alter the magnitude of an optical rotation measurement and even change the sign of the optical rotation.[103] Furthermore, the concentration of the solute has an effect that is usually ignored when making measurements but it can be large enough to produce a sign change in the ORD but this a rare condition and I know of only one example which is given in the cited reference.[84] This is the result of solute-solute interactions or the lack thereof which is a function of the concentration. Additionally, the solvent can form a transient "structure" around the chiral

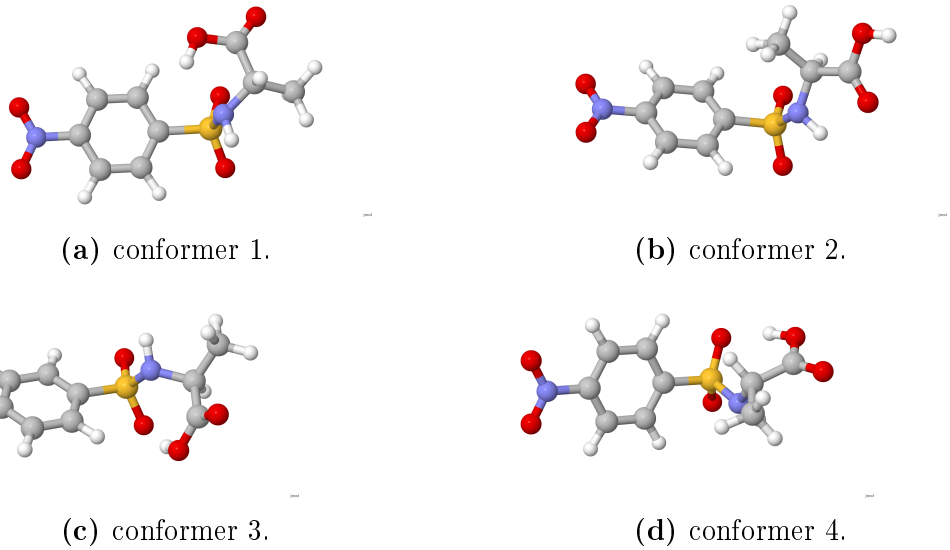

(a) conformer 1. **(b)** conformer 2.

(c) conformer 3. **(d)** conformer 4.

Figure 5.2: The conformers of *S*-NPNPSA.

molecule which can have an ORD commensurate with the ORD of the sample in solution.[155] This sort of effect could not be modeled with something like a polarizable continiuum model. To accurately simulate such effects explicit solvent models need to be utilized.[155] It would be interesting if a polarizable continiuum model could be developed that could model an induced chirality. In addition to solvent effects, the conformational flexibility of a molecule requires that all conformers be identified in order to calculate a Boltzmann weighted optical rotatory dispersion curve. In some cases, like carvone, this is particularly important because the conformers act like pseudoenantiomers which is to say that the two conformers have oppositely signed ECD or ORD.[152] Use of DFT and frequency calculations to determine the population is sometimes insufficient, especially when the predicted sign varies among conformers. This was shown recently to be true in the case of the molecule carvone where more accurate model chemistries, like G3, G3MP2, and G3MP2B3 for example, had to be applied to calculate the ORD of carvone in Chapter 2. On top of traditional solvent effects i.e. the alterations of the solute caused by the solvent, you can have induced chirality in the solvent molecule as well as chiral solvent structures that form around the solute causing a substantial optical rotation on the order of the optical rotation of the solute. To further complicate the issue, calculations performed at the equilibrium geometry often do not produce the correct sign because of neglected vibrational corrections. For example, the

molecules S-propelyne oxide and carvone required the inclusion of vibrational corrections to calculate an accurate ORD.[40;44;47;156] With all these complications, calculations of an accurate optical rotations has proved to be a formidable challenge. Nonetheless, even with all the challenges listed above, there have been some successes in determining absolute configurations using the methods used herein.[18;154;157;158] Electronic circular dichroism can, in principle, also be used to determine the absolute configuration(AC). Before the introduction of computational methods capable of calculating ECD other methods such as empirical rules, exciton coupling, or semiclassical methods were used to determine the AC.[18;152;159] Now methods such as EOM-CCSD and TD-DFT others allow for the calculation of the excited states energy and as well as rotational and oscillator strengths for transitions from the ground state. Generally these are done without considering nuclear motion although there have been some studies of the effect of nuclear motion on an electronic circular dichroism.[98] Bringmann et. al gives recommendation on how to determine the absolute configuration using the electronic circular dichroism.[160]

Since the majority of electronic circular dichroism and optical rotatory dispersion calculations are measured in solution it is important to consider the effects of the solvent. There are several approaches available ranging from Onsager type reaction fields to explicit solvent models(see the introduction of Chapter 22 for further discussion). In this chapter a polarization continiuum model is used to approximate the effects of solvents. Since the approach used in this chapter is similar to those given in 2.1 the key difference between the two approaches will be discussed. There is one key difference between the solvent model used for carvone and the one used for NPNPA and NPNPSA. Both NPNPA and NPNPSA have acidic hydrogens. These acidic hydrogens require a solvent exclusion sphere that is centered around them because of their partial charge which results from them being attached to an electronegative atom.[58]

5.2 Experimental Optical Rotatory Dispersion

The Optical Rotatory Dispersion curves were measured at 22° to 25° C using a 10 cm path length at 589 nm, 578 nm, 546 nm, and 436 nm with a Perkin Elmer model 241 polarimeter. Measurements were performed in reagent grade methanol with a concentration of 3.6×10^{-2}

g/ml and 6.82×10^{-}2 g/ml for S-(-)-NPNPA and S-(+)-NPNPSA, respectively. For S-(-)-NPNPA, the ORD below could not be measured below 546 nm because the of the strong absorption of then $n \rightarrow \pi^{\star}$ transition(see Figure 5.5). These samples were filtered prior to measurement with 0.45 micron filter to remove potential contaminants like dust which can greatly affect optical measurements. Samples used for this study come from the same batch employed in the study on negative ion properties of NPNPA and NPNPSA. Absolute configuration and purity(estimated at >98%) of the samples is established by the synthesis procedure which gets it chirality from the alanine moiety. The ORD curves for S-NPNPSA and S-NPNPA are given in Figures 5.9 and 5.10. The quoted error in the rotation angle for this instrument is ±0.006 degrees. Measurements from the instrument typically fluctuated by ±0.002 degrees.

5.3 Experimental ECD

The CD spectra of NPNPA and NPNPSA were recorded using a 1 mm cuvette with an Aviv Biomedical model 202 CD spectrometer. A 1 cm path-length cell was used for alanine because of the limited solubility of alanine in methanol. All solutions were prepared with HPLC grade methanol. For each scan, three spectra were recorded and averaged. Each datum was acquired with three seconds of averaging and monochromator bandwidth of 1 nm. These spectra were then averaged. The synthesis of NPNPSA and NPNPA is summarized below. The R and S-alanine sample had quoted purities of 98% and 99%, respectively. The concentration S-alanine samples were 6.73×10^{-3} and 1.73×10^{-3} M, respectively. Unlike alanine, NPNPSA and NPNPA are readily soluble in methanol. The R- and S- NPNPSA samples used for measuring the CD had a concentration of 4.30×10^{-3} and 5.30×10^{-3}. To complete the CD of R-NPNPA, a concentration of 3.62×10^{-2}M was used to measure the CD from 190 nm to 350 nm and 7.1×10^{-3} M was used from 350 nm to 800 nm. A lower concentration was required at longer wavelengths because of strong absorption at approximately 380 nm due to the nitrobenzene $n \rightarrow \pi^{\star}$ transition. The spectra produced by these runs were equal and opposite as expected. All runs including two enantiomers were averaged using the $\langle CD \rangle = 0.5(CD_r - CD_s)$. This averaging will subtract out the error due to artifacts in experimental data and gives a cleaner ECD signal.

5.4 Experimental UV/Vis

The UV/Vis spectrum for *R*-NPNPSA, *S*-NPNPA, and *S*-alanine were acquired using a Thermo-scientific EV-60 UV/Vis spectrometer. All solutions were prepared with methanol as a solvent. The data was acquired a various concentrations to obtain the complete spectra. The bandwidth for all scans was set to 1nm. Concentrations of the solutions of NPNPSA were 5.84×10^{-3} M, 2.92×10^{-4} M, and 5.84×10^{-4} M. For NPNPA the solution concentrations were 3.81×10^{-3} M, 3.81×10^{-4} M, and 5.84×10^{-5} M. Multiple concentrations were used because some regions absorbed more strongly and therefore required a smaller concentration. A nearly saturated solution (3 g/l) of alanine was used to record the UV/VIS spectra of alanine. Because of the limited solubility of alanine in methanol, 27 mg of alanine were added to $\sim$ 9 ml of methanol and this was heated and sonicated for 1 hour. After the sample cooled to room temperature a small amount of methanol was added to reach a full 10 ml alanine/methanol solution. Then the fluid sample was removed leaving 21 mg of alanine remaining in the container. The maximum concentration of alanine in methanol at room temperature is approximately 6.73×10^{-3} M. All the samples were filtered with a 0.45 micron syringe filter as a precautionary measure.

5.5 computational methods

5.5.1 PCM and G3MP2B3

Since every measurement was performed with methanol as the solvent the solvent effects of methanol are simulated using the integral equation formulation of the Polarization Continiuum Model(IEF-PCM) as implemented in Gaussian03.[64;161] The PCM model part of the simulations used the UAO (Simple United Atom Topological Model) to construct the solvent exclusion region. Explicit spheres were attached to acidic hydrogens, i.e. all those bond to nitrogen and oxygen in NPNPA and NPNPSA because the simple united topological model does not explicitly account for hydrogens. An accurate conformational population can be very important when calculating the ORD and ECD, especially when the sign of the ORD and CD differs between different conformers. For example, in Chapter **??** it was

shown that energies derived from DFT/B3LYP energies were insufficient when determining the conformational populations in carvone, particularly because some of the conformers had opposing signs(see 2). For carvone, the G3 model chemistry was used for gas phase simulations and the G3MP2 was used in conjunction with the PCM mode to calculate the ORD in solution.[162] This article uses the G3MP2B3 model chemistry to calculate the Gibbs free energy which in then used to determine the relative populations of the conformers of NPNPA and NPNPSA.[77;78;162] The G3MP2B3 begins with geometry optimization and frequency calculation using B3LYP/6-31G(d) to determine the zero point and vibrational energy correction. This is followed by a QCISD/6-31G(d) and a MP2 calculation with the GTMP2Large basis set.

5.5.2 ECD and UV/Vis of NPNPA and NPNPSA

The ECD was calculated with for all conformers using TD-DFT/B3LYP with the 6-31G(d) and the aug-cc-pVDZ(referred to as aVDZ) basis set using a structure optimized with the same method and basis set used to perform the simulations of the optical rotation, circular dichroism, and UV/Vis.[74] Excited state geometry changes and vibronic effects were ignored for these simulations. Fifteen excitations were used to calculate the ECD and the UV/Vis Absorption of NPNPA and NPNPSA. The solvent effects were treated with the PCM model in the exact same fashion used in the G3MP2B3 calculations. The CD in Figures 5.8 and 5.7 were calculated using the following equations

$$CD_i = 0.024569 \sum_{j=1}^{N} \frac{R_j \nu_j}{\sigma} e^{\frac{(\nu-\nu_j)^2}{\sigma^2}} \tag{5.1}$$

$$CD_{total} = \sum_{1}^{n} P_i \cdot CD_i \tag{5.2}$$

where CD_i is the CD for the ith conformer, R_j is the rotational strength in units of $10^{-40}\,\mathrm{erg\,esu\,cm\,Gauss^{-1}}$, ν_j is the frequency in cm^{-1}, respectively, of each CD band, and P_i is the population of the ith conformer. The peak broadening parameter σ was chosen

to be between 2000 and 3000 cm^{-1}.[163†] In the analysis of the ECD the frequencies of the transitions were shifted to bring the experimental and theoretical UV/Vis into aggreement before the ECD was compared to experiment. This is following the recommendation of Bringman *et al.* when using ECD to try to determine the absolute configuration.[160] When simulating the ECD, the velocity gauge rotational strength was used to insure the origin independence of the rotational strength. The ORD of both molecules was calculated using DFT/B3LYP with the 6-31G(d) and the aVDZ basis set using linear response theory at 632.8 nm, 589 nm, 546 nm, and 436 nm using geometries optimized with the method and basis set used to simulate the ORD. For the conformers constituting up the majority of the population the ORD was also calcualted with 6-311G(*d*,*p*). The G3MP2B3 populations were used to simulate the population weighted ORD. As with the G3MP2B3, ECD, and optimizations, the PCM model was included to simulate the effects of solvents.

The method used to do this was based upon the work of Wiberg *et. al.*[50] Essentially a Taylor expansion of the ORD is taken around the equilibrium geometry. The ORD at each step along a normal mode coordinate was taken to be 0.05 with the numerical second derivative calculated with a central difference. The vibrational corrections were weighted to take into account the effects of temperature on the measured value. The ORD used for the vibrational corrections was calculated with B3LYP/6-311G(*d*,*p*). The equilibrium geometry used for these simulations was taken from an optimization performed with B3LYP/aVDZ. The frequency and displacement of each normal mode coordinate came from the B3LYP/6-31G(*d*) calculations that are a part of the G3MP2B3 simulations. As with previous calculations, the solvent was modeled using a polarization continiuum model. The continiuum model produced a new solvent exclusion region for each simulation based on the current geometry. For both NPNPA and NPNPSA some of the vibrations produced spuriously large correction factors because the nature of the vibrational is not well represented by a rectilinear coordinate system used to move the atoms along the normal mode. Gaussian03 lists each normal mode as a list of displacements in the x, y, and z directions. This representation of the normal modes is only accurate for small

†The constant 0.024569 in Equation 5.2 is slighty different than the one given in the book by Bari and Pescitelli and Chapter 2. The one in this chapter uses the full accuracy of the appropriate physical constants

displacements. The results from these vibrations were removed from the analysis. This is noted in the Appendix A.2. For conformer 3 of NPNPA the corrections from normal modes 1-4 were removed and conformer 1 had the modes 1-5 removed from the analysis. these low frequency modes have large displacement expectation values because of the large population in excited states. NPNPSA also required that some modes be removed from the analysis because of excessively large correction factors associated with them. For conformer 2 on NPNPSA the corrections due to normal modes 1-7 were cut from the analysis. Conformer 4 had normal modes 1-6 removed from the analysis. If the signs of the modes that were cut are a representative of the correction factor than they will not correct the ORD in the correct direction.

5.6 Results

5.6.1 G3MP2B3

There are two dominate conformers For both NPNPA and NPNPSA. Conformers 1 and 3 dominate in NPNPA with total populations of 0.384 and 0.569, respectively. These populations are remarkably different than the results reported for gas phase NPNPA using the MO6-2X functional The calculations in Lambert*et al.* suggest that only the first conformer needs to be considered because all others had such a low population. This may be a result of the solvent but it is more likely an effect due to inadequecies associated with DFT that are compensated for by G3MP2B3. Conformers 1 and 3 of NPNPA are both stabilized by intramolecular hydrogen bonding (see Table 5.1). For conformer 1, the hydrogen attached to the nitrogen hydrogen bonds with the doubly bonded oxygen on the carboxlyic acid. For conformer 3, the hydrogen attached to the oxygen in the carboxylate bonds to the lone pair of the nitrogen. In conformer 1 the NH is in the plane of the nitrobenzene which implies that its π electrons are delocalized over the nitrobenzene structure. In conformer 3, the nitrogen takes on a trigonal pyramidal structure because of localization of the hydrogen bonding lone pair. For NPNPSA, the population is dominated by conformers 2 and 4 with a population of 0.656 and 0.339, respectively(see Table 5.2).

Table 5.1: The populations of each conformer of NPNPA at 298.15K calculated with the G3MP2B3 method .

	G3MP2B3		
conformer	relative energy(eV)	Δ G(eV)	population at 298.15
1	0.167	0.010	0.384
2	0.423	0.275	0.000
3	0.151	0.000	0.569
4	0.245	0.082	0.024
5	0.413	0.262	0.000
6	0.000	0.082	0.024

Table 5.2: The populations of each conformer of NPNPSA at 298.15K calculated with the G3MP2B3 method .

	G3MP2B3		
conformer	relative energy(eV)	ΔG(eV)	population at 298.15
1	0.120	0.144	0.002
2	0.000	0.000	0.656
3	0.130	0.145	0.002
4	0.032	0.017	0.339

Conformer 2 of NPNPSA is hydrogen bond stabilized by the NH hydrogen bonding to the lone pair of the double bonded oxygen of the carboxylic acid. Conformer 4 is stabilized by the hydrogen bonding between the lone pair of one of the oxygen in the SO_2 to the hydrogen of the carboxylic acid.

5.6.2 UV/Vis

The CD and UV/Vis spectrum of S-alanine was acquired as a reference since both NPNPA and NPNPSA contained the alanine moiety. This comparison plot is given in Figure 5.5. The majority of the structure in the CD and absorption spectrum of alanine lies in the VUV region.[164] The UV/vis spectrum of alanine in methanol has been measured previously and agree with that in Figure 5.3.[165] The UV/Vis spectra for nitrobenzene is available from NIST webbook and has a maximum absorption wavelength at approximately 260 nm and extends from the UV region to approximately 410 nm. The magnitude of the UV/Vis

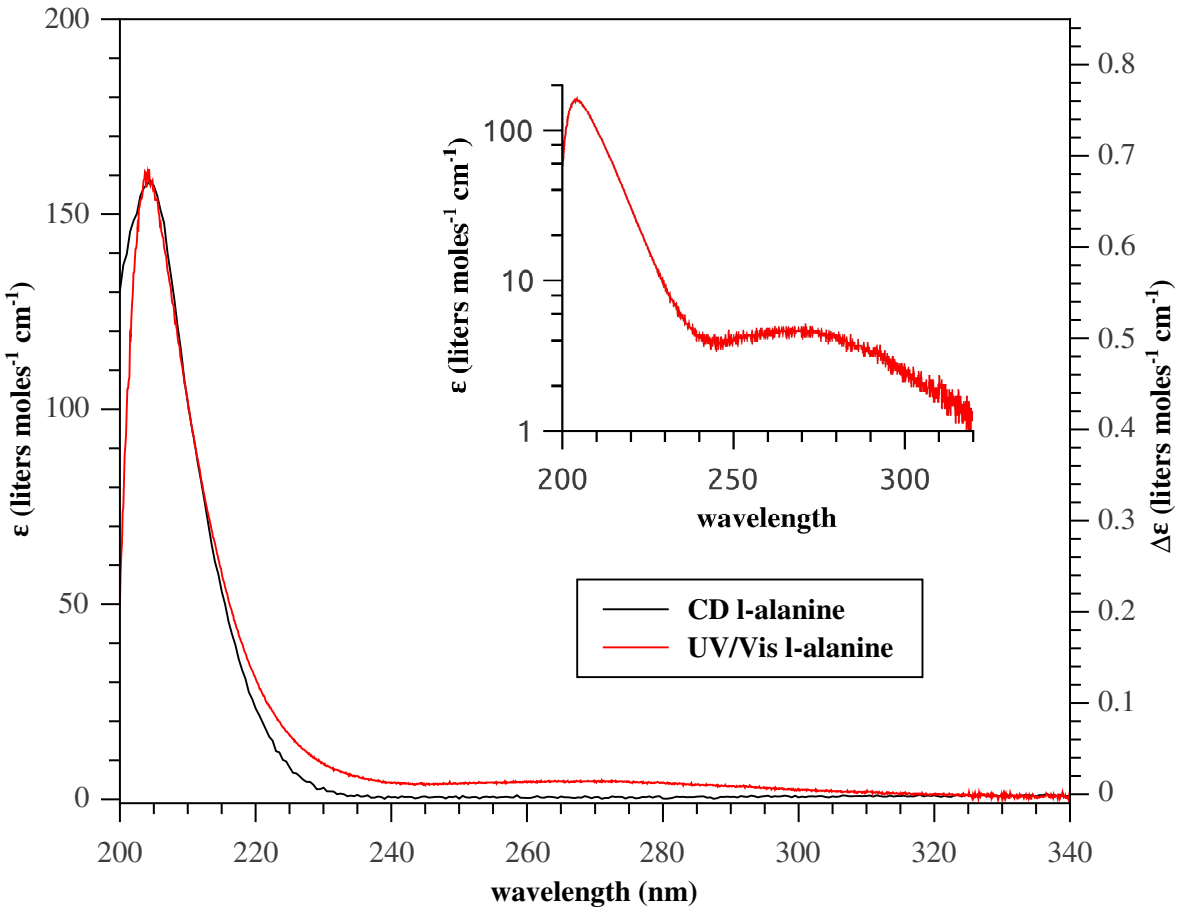

Figure 5.3: The experimental UV/Vis absorption and ECD of the *S*-alanine.

spectrum of alanine is smaller than that of NPNPA or NPNPSA by 2 orders of magnitude. Alanine exhibits a strong absorption peak at the 202 nm and a second much weaker peak at 270 nm. The peak at $\sim$ 270 nm is much smaller in amplitude and did not exhibit an observable CD. The CD of this peak has been observed for a highly concentrated solution of alanine in water but it is below our detection limit.[164] The positions of the absorption peaks of alanine are close to absorption peaks in NPNPSA, albiet much with different amplitudes. Closer inspection of the associated transitions of NPNPSA show that the orbitals appeared to be transitions from the lone pair orbitals of alanine to the $\pi^\star$ orbitals of the nitrobenzene but it is hard to define a definite character to the orbital.

The lowest energy transition of conformer 2 and conformer 4 NPNPSA has a neglible transition dipole moment. The three lowest energy transitions of NPNPSA required

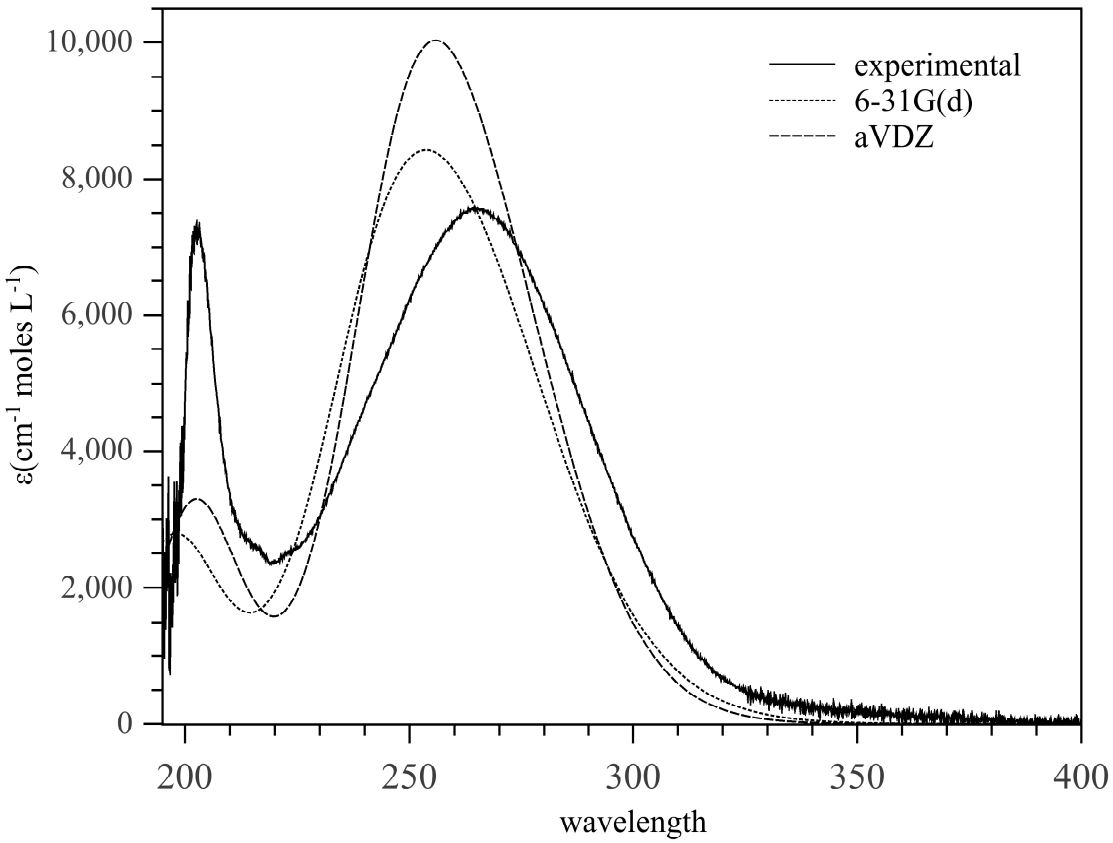

Figure 5.4: A theoretical and experimental comparison plot of UV/Vis of NPNPSA.

significant shifting to higher energy upon when comparing the experimental and calculated UV/Vis spectrum(see Table A.3). The higher energy peaks required less shifting than the lower energy transitions. It is interesting to note that the position of the observed experimental bands is the same for NPNPSA and alanine albeit with very large intensity differences. NPNPA has a peak at the same wavelength as the UV/Vis of alanine and NPNPSA at 202 nm. The $n \rightarrow \pi^{\star}$ transition of NPNPA was clearly the strongest both theoretically and experimentally for NPNPA and contains a total of three absorption bands in its broadened structure. The oscillator strengths and positions did not vary significantly for the $n \rightarrow \pi^{\star}$ transition when comparing the two basis sets employed. The simulations of the UV/Vis data of NPNPA and NPNPSA agreed very well with experiment when the excitation energies were shifted for comparison to the experimental data. Nonetheless, the B3LYP functional consistently underestimated the excitation energy in NPNPSA and

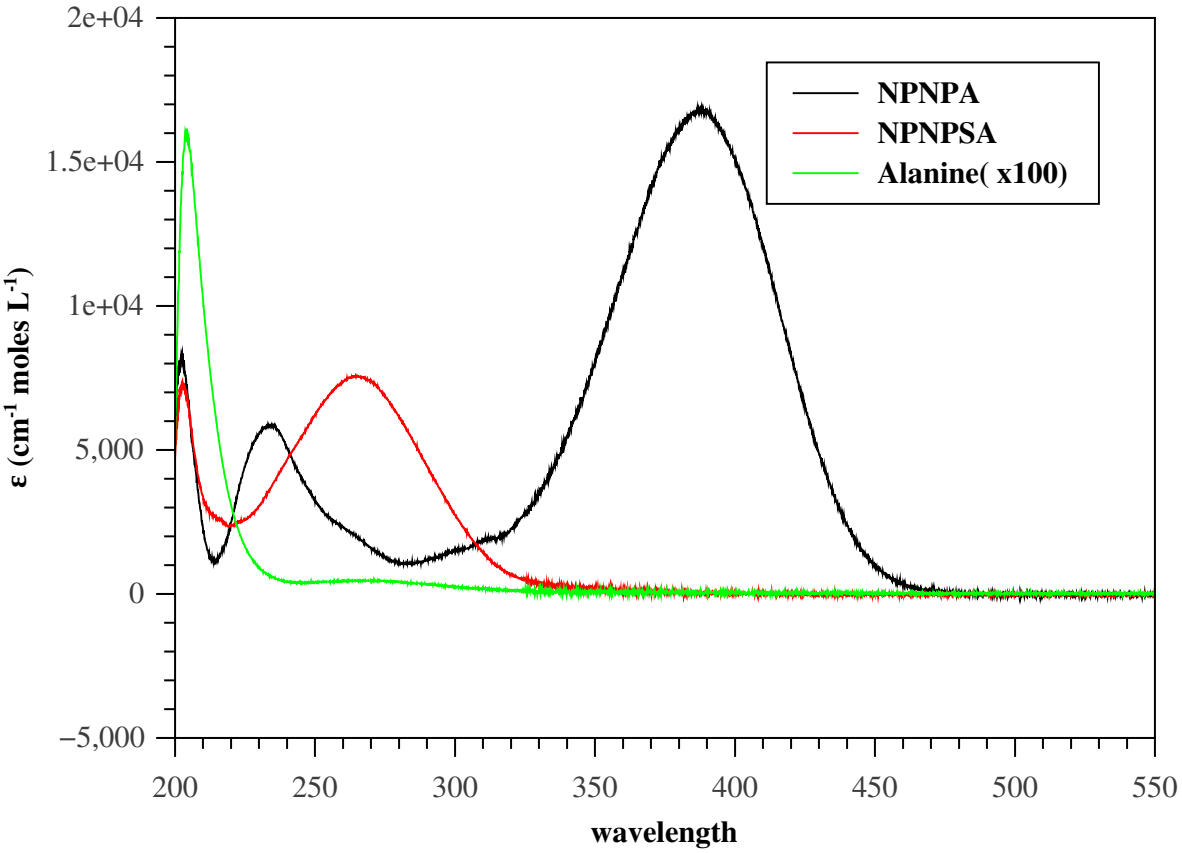

Figure 5.5: A comparison plot of total UV/Vis absorption of alanine, NPNPA and NPNPSA in methanol.

overestimated it in NPNPA. The excitation energies used to model the UV/Vis experimental data NPNPA and NPNPSA are given in Tables A.1, A.2, A.3 and A.4.

5.6.3 ECD

The ECD of *S*-alanine shown in Figure 5.3 in the region observed was smooth, having one positive peak at 202 nm. *S*-NPNPSA also exhibited a positive peak in the same position. For *S*-alanine in water there is also a very small negative ECD peak around 252 nm which corresponds to the 270 nm peak in methanol.[164] In the same region, NPNPSA shows a diffuse weak positive ECD band although it is hard to infer any sort of relationship with the difference in solvent. For NPNPSA, the second lowest energy transition (the first

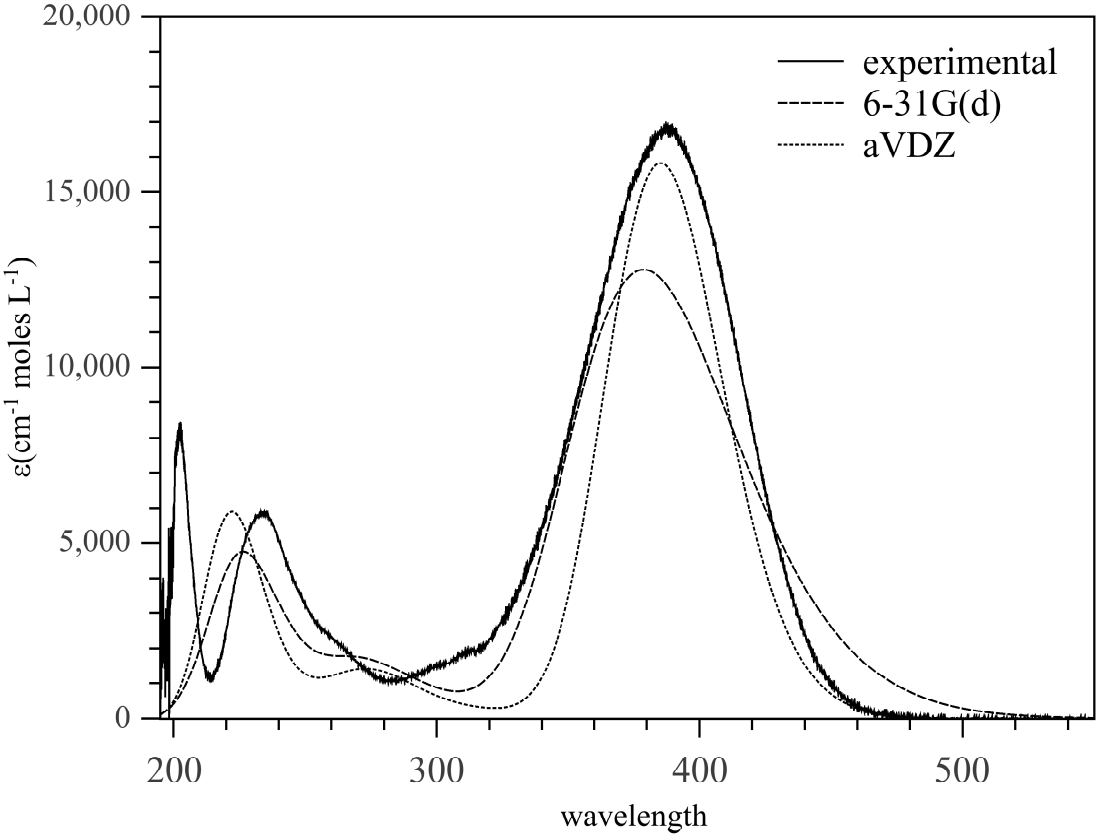

Figure 5.6: A comparison plot between the theoretical and experimental UV/Vis of NPNPA.

dipole active transition) electric and magnetic dipole moments where nearly orthogonal for conformer 2 when calculated with both aVDZ and 6-31G(d). This near orthogonality makes the this transition suceptible to sign changes with subte differences in structure. For NPNPSA the TD-DFT calculations did not reproduce the ECD spectra even though it peak positions were empirically shifted using the UV/Vis data. In fact, in the case of *S*-NPNPSA, the calculated ECD was diametrically opposed to the measured ECD for the whole spectrum (see Figure 5.7). The measurements were performed with two different batches to see if it was possibly an error in the our initial assignment of absolute configuration. For *R*-

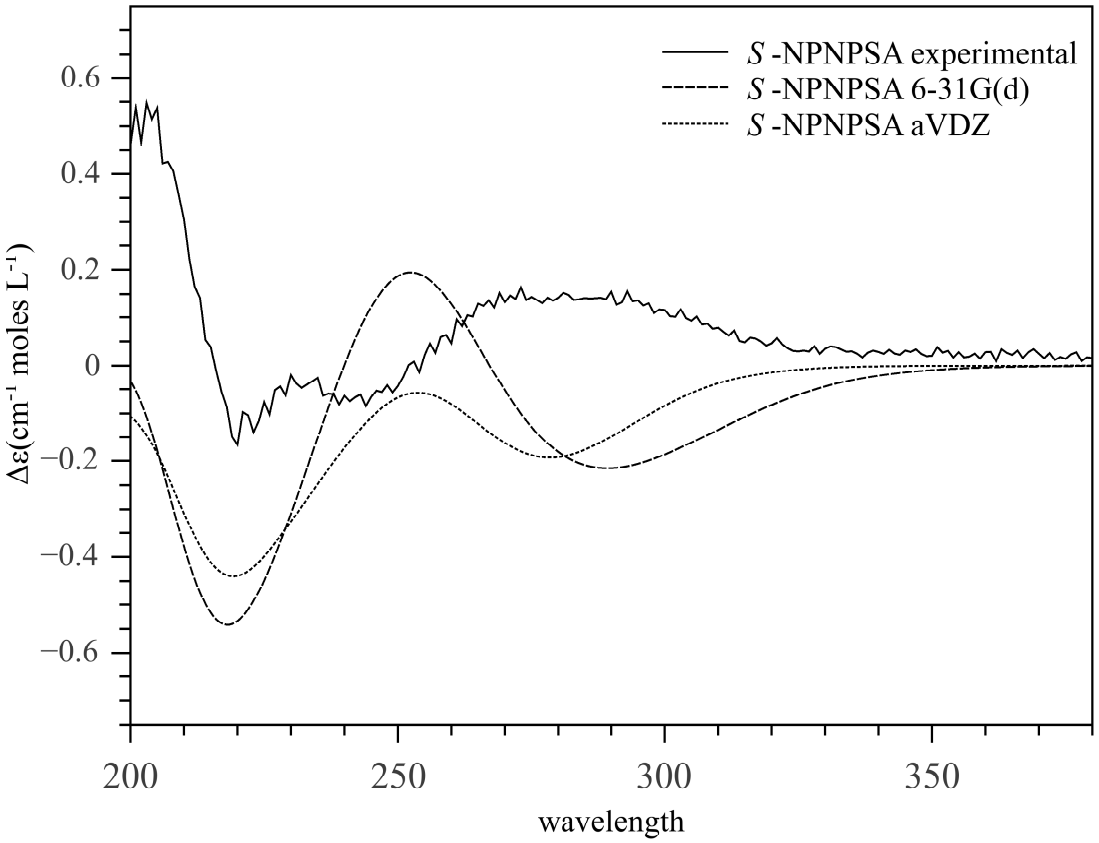

Figure 5.7: A comparison between the theoretical and experimental ECD of *S*-NPNPSA.

NPNPA, there was partial agreement between theory and experiment, depending upon the wavelength region and transition. In the wavelength region covering 220 nm to 260 nm the calculated ECD had the same sign as experiment when calculated with aVDZ basis set. The $n \rightarrow \pi^{\star}$ transition of *R*-NPNPA had the "correct" sign for both conformers 1 and 3 when

calculated with 6-31G(d), but because both of the conformers have significiant population is not expected that the signs should agree. On the other hand, when the transition states were calculated with aVDZ the rotational strength of conformer 1 was positive and conformer 3 was negative. Since the ECD is so small for the $n \rightarrow \pi^{\star}$ transition it is likely that each conformer has a different sign which would decrease the overall magnitude. For conformer 3 the 5th transition was a factor of -10 smaller when calculated with 6-31G(d). The seventh transition of conformer 1 was a factor of 28 smaller when calculated with 6-31G(d) and had the opposite sign. Furthermore, it is worth noting that the direction of the $n \rightarrow \pi^{\star}$ transition dipole moment of conformer 1 nearly reversed its direction when calculated with aVDZ versus 6-31G(d). The results of the calculations of the ECD with TD-DFT are shown in Tables A.1 and A.2. In general, when considering the experimental difficulty in obtaining

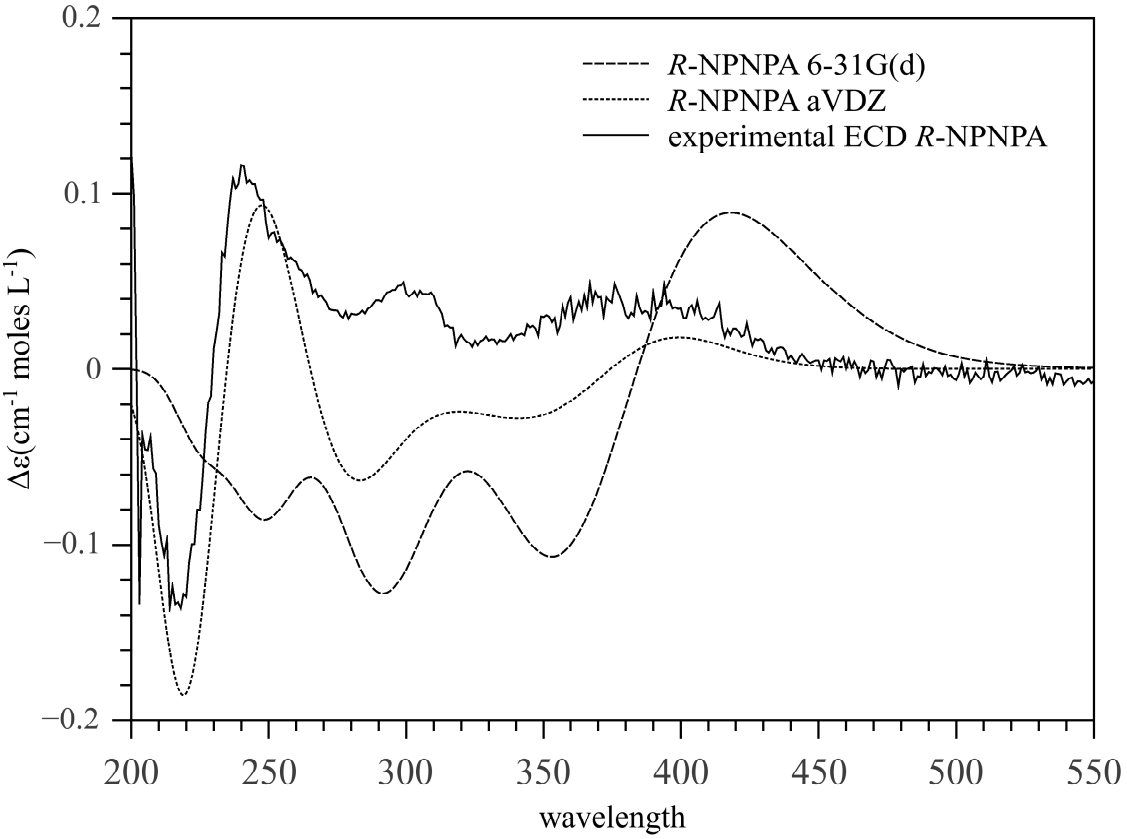

Figure 5.8: comparison of experimental and theoretical ECD of *R*-NPNPA

a spectrum over the region of the $n \rightarrow \pi^{\star}$ because of the strong absorption compared to the magnitude of the CD, the weaker $n \rightarrow \pi^{\star}$ predicted by the aVDZ basis set is more in tune

with experiment. Given the large variation in the calculated ECD when using these two basis sets it is remarkable that the ORD produced with each basis set is so similar. It is important to note that shifting the bands to minimize the difference between the theoretical and experimental UV/Vis was hindered by the fact that some of the ECD bands of both molecules had strong oscillator strengths and weak or nonexistent rotational strengths or vice versa. Also, applying the same scale factor to every conformer may be inaccurate.

5.6.4 ORD

For both molecules the ORD had the opposite sign when compared to experiment and the magnitude was much larger than the magnitude of the observed ORD regardless of method and basis set. This is illustrated by comparing Figures 5.9 and 5.10 with Tables 5.5 and 5.6. Also, the inclusion of the vibrational corrections with the method described by Wiberg *et. al.* pushed the ORD further from the expected result.[50] ORD is strongly dependent upon the position and sign of the electronic circular dichroism bands, which is evident from the Kronig-Kramers relations.

Table 5.3: The calculated ORD of *R*-NPNPA using B3LYP with various basis sets with and without vibrational corrections.

	Calculated ORD		
wavelength	6-31G(d) ORD	aVDZ	6-311G(*d*,*p*) R
632.80	-193.61	-170.67	
589.00	-228.84	-204.38	-246.88
578.00	-239.27	-214.57	
546.00	-274.18	-249.43	
436.00	-473.75	-489.30	-576.78
589.00[a]	-316.61	-292.15	-334.65
436.00[a]	-171.53	-187.09	-274.57

a. vibrational corrected values

Therefore, incorrect signs and positioning of electronic bands will have a strong effect on the ORD. scaling factors were needed because the electronic circular dichroism of both NPNPA and NPNPSA suffer from incorrect positions of excitations. For conformer 3 of NPNPA the ORD did not have any significant difference introduced by the choice of basis

Table 5.4: The calculated ORD of *S*-NPNPSA using B3LYP with various basis sets with and without vibrational corrections.

	Calculated ORD		
wavelength	6-31G(d) ORD	aVDZ	6-311G(*d*,*p*)
632.80	-104.68	-125.34	
589.00	-127.63	-152.48	-107.21
578.00	-134.70	-160.84	
546.00	-159.47	-190.03	
436.00	-354.56	-420.65	-305.85
589.00[a]	-422.95	-447.80	-402.54
436.00[a]	-1567.29	-1633.38	-1518.58

a. vibrational corrected values

set. The calculated ORD for conformer 1 was about a factor of two smaller than the ORD calculated for conformer 3. The exceptions to this are for conformer 1 at 436 nm which decreases to -37 deg dm^{-1} (g/mL)$^{-1}$from -181 degrees when calculated with aVDZ and 302.6 deg dm^{-1} (g/mL)$^{-1}$when calculated with 6-311G(*d*,*p*) This explains the great difference between the magnitude of the ORD when comparing conformer 1 and 3 at 436 nm(see Table 5.5. The vibrational corrections of NPNPA pushed the calculated ORD further from the experimental results with vibrational corrections simulations at 589 nm. The vibrational corrections for NPNPA conformer 1 was -106.56 deg dm^{-1} (g/mL)$^{-1}$at 589 and 447.23 deg dm^{-1} (g/mL)$^{-1}$at 436 nm. The large correction at 436 nm is presumably

Table 5.5: The calculated ORD of *R*-NPNPA using B3LYP with various basis sets with for each conformer.

	conformer 1			conformer 2		conformer 3		
wavelength	6-31G(d)	aVDZ	6-311G(*d*,*p*)	6-31G(d)	aVDZ	6-31G(d)	aVDZ	6-311G(*d*,*p*)
632.800	-104.750	-105.290	-	245.940	116.730	-282.64	-241.96	-
589.000	-116.620	-122.510	-155.770	310.930	150.740	-339.17	-292.41	-337.3
578.000	-119.540	-127.430	-	331.850	161.950	-356.32	-307.86	-
546.000	-127.050	-143.210	-	408.330	204.100	-415.35	-361.54	-
436.000	-37.810	-181.530	-302.600	1217.110	765.510	-846.27	-783.25	-824.14
	conformer 4			conformer 5		conformer 6		
632.800	56.480	141.020	-	-224.930	-226.520	244.45	163.22	-
589.000	72.800	179.000	-	-279.890	-288.750	288.94	191.36	-
578.000	78.110	191.290	-	-297.310	-309.030	302.11	199.52	-
546.000	97.680	236.520	-	-360.090	-384.330	346.25	226.15	-
436.000	308.080	756.370	-	-979.790	-1328.470	604.2	323.71	-

because it is near an absorption band. For conformer 3 the correction value was -82.46

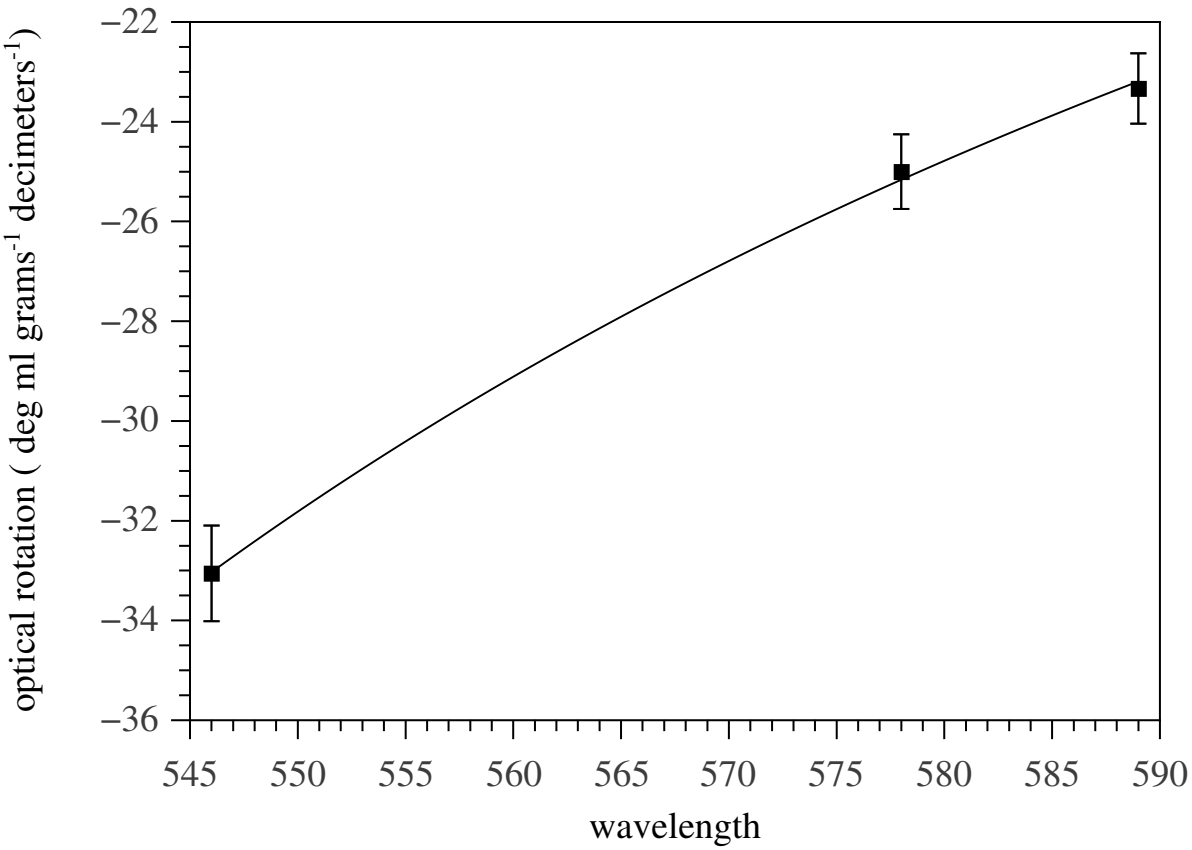

Figure 5.9: The optical rotatory dispersion curve on *S*-NPNPA.

deg dm^{-1} $(g/mL)^{-1}$at 589 nm and 229.85 deg dm^{-1} $(g/mL)^{-1}$at 436 nm. The vibrational corrections in this case do not push the theoretical values closer to experiment. The reason for this is unclear. The use of the polarization continiuum model introduces issues with the solvent response time compared to the vibrations.

Table 5.6: The calculated ORD of *S*-NPNPSA using B3LYP with various basis sets with for each conformer.

	conformer 1		conformer 2		
wavelength	6-31G(d)	aVDZ	6-31G(d)	aVDZ	6-311G(*d*,*p*)
632.80	-151.09	-168.8	-26.91	-57.23	-
589.00	-180.93	-202.9	-34.80	-71.35	-29.91
578.00	-189.93	-213.2	-37.33	-75.80	-
546.00	-220.71	-248.7	-46.56	-91.66	-
436.00	-431.71	-500.1	-132.03	-229.52	-130.21
	conformer 3		conformer 4		
632.80	-173.77	-159.16	-254.31	-256.55	-
589.00	-205.52	-188.69	-306.28	-308.80	-258.23
578.00	-214.94	-197.49	-322.11	-324.70	-
546.00	-246.67	-227.20	-376.83	-379.63	-
436.00	-446.17	-418.36	-785.84	-789.79	-649.83

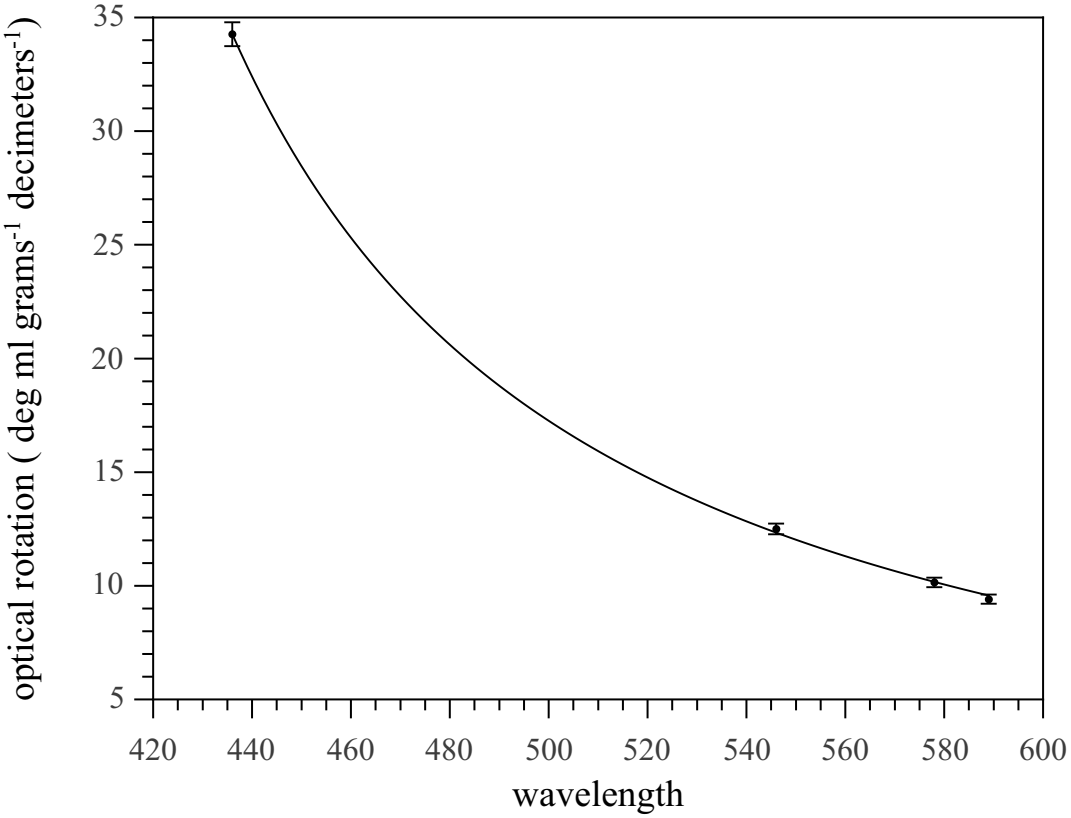

Figure 5.10: The optical rotatory dispersion curve on *S*-NPNPSA.

For *S*-NPNPSA the calculated optical rotation also disagreed with experiment. The optical rotation was calculated to be negative for every conformer at every wavelength. The calculations produced consistent results reqardless of the chosen basis set with the exception of the aVDZ calculation of conformer 2 being 2 times larger in magnitude then the calculations with 6-31G(*d*) and 6-311G(*d*,*p*). Conformer 2 of NPNPSA had a correction factor of -2074.0 deg dm^{-1} $(g/mL)^{-1}$at 436 nm and -534.0 deg dm^{-1} $(g/mL)^{-1}$but these large corrections were balanced by the corrections to coformer 4 which had a correction factor 436.3 deg dm^{-1} $(g/mL)^{-1}$at 436 nm and 162.0 deg dm^{-1} $(g/mL)^{-1}$at 589 nm.

5.7 Summary and Conclusions

The ECD, UV/Vis and the ORD for NPNPA and NPNPSA have been compared to theory with the hope of ascertaining the absolute configuration. All measurements were performed with methanol as a solvent. To account for the effects of the solvent, all simulations were performed with the polarization continiuum model. The model chemistry G3MP2B3 was used to calculate the conformational populations for both NPNPA and NPNPSA. The ECD and UV/Vis were calculated using the TD-DFT/B3LYP/aVDZ and 6-31G(*d*). When comparing the UV/Vis to experiment a significant amount of shifting of the transitions energies to bring the peak positions into agreement with experiment. The magnitude of the calculated UV/Vis peaks reproduced.

The agreeement between experimental and theoretical ECD of NPNPA is intermittent. If you look at the lowest energy transition of NPNPA the assignment the the calculated ECD agrees but this agreement shifts. In general it is known that transitions to Rydberg states are not accurately captured by TD-DFT. The primary culprit for disagreement being the calculated sign of the rotational strengths. This is likely resulting from inadequacy of TD-DFT. Higher level calculations are likely necessary to obtain accurate sign for the rotational strengths.

Agreement between the calculated and experiment optical rotation is nonexistent. The calculated optical rotation had poor agreement when compared to experiment. The inclusion of vibrational corrections pushed the calculated values further from the experimental values. The polarization continiuum model calculated a unique solvent exclusion region when

computing the second derivatives. This may be in err but it not believed to be substansial enough to produce the observed disagreement. The low frequency modes may have may be the culprit for this as they are expected to have large corrections values because the modify the geometry a large amount when populated. This is an interesting problem. Because of the caucophony of potential sources of disagreement it is hard to point to a single major contribution. This may result from an inadequacy of DFT, e.g. its inability to effectively model charge-transfer states and Rydberg states. If this is the case than higher level calculations of the ECD and the ORD using methods like CCSD may provide the answer. If the disagreement is resulting from inadequacy of DFT then the that error would propagate through the vibrational corrections as well. Also, the treatment of the solvent environment as a polarizable continuum may be insufficient. Methanol does have a hydrogen bond donor and this may introduce more exotic solvent effects that were not considered herein which require much larger scale modeling similar to that performed by Neugebauer. This chapter invites some very interesting questions that leave room for additional much research. Quantum chemistry is at the threshold of describing the subtle properties of complex molecules.

Bibliography

[1] Ira N. Levine. *Quantum Chemistry*. Prentice Hall, 6 edition, 2008. 2

[2] J. Dennis Caldwell and Henry Eyring. *The Theory of Optical Activity*. John Wiley, 1 edition, 1971. 2, 10, 12

[3] Ralf Wesendrup, Jon K. Laerdahl, Robert N. Compton, and Peter Schwerdtfeger. Biomolecular homochirality and electroweak interactions. i. the yamagata hypothesis. *J. Phys. Chem. A*, 107(5294):6668–6673, April 2003. 2, 4

[4] T. Martin Lowry. *Optical Rotatory Power*. Dover, New York, 1964. 3, 4

[5] George A. Khoury, Richard C. Baliban, and Christodoulos A. Floudas. Proteome-wide post-translational modification statistics: frequency analysis and curation of the swiss-prot database. *Scientific Reports*, 1:90, 2011. 4

[6] T. J. Leiterig, D. G. Guadagni, Jean Harris, T. R. Mon, and R. Teranishi Eranishi. Evidence for the difference between the odours of the optical isomers (+)- and (-)-carvone. *Nature*, 230, 1971. 4

[7] Jennifer C. Brookes, A. P. Horsfield, and A. M. Stoneham. Odour character differences for enantiomers correlate with molecular flexibility. *J. R. Soc. Interface*, 6:75–86, 2008. 4

[8] SK Teo, WA Colburn, WG Tracewell, KA Kook, DI Stirling, MS Jaworsky, MA Scheffler, SD Thomas, and OL Laskin. Clinical pharmacokinetics of thalidomide. *Clin. Pharmacokinet.*, 43:311–327, 2004. 4

[9] A. Wayne Garrison. *Chiral Pesticides: Stereoselectivity and Its Consequences*. American Chemical Society, 2011. 4

[10] Stephen Mason. Biomolecular homochirality. *Chem. Soc. Rev.*, 17:347–359, 1988. 4

[11] A Lahamer, S Mahurin, R Compton, D House, J Laerdahl, M Lein, and P Schwerdtfeger. Search for a parity-violating energy difference between enantiomers of a chiral iron complex. *Physical review letters*, 85(21), November 2000. 4

[12] Nagy Szabo and Lajos Keszthelyi. Demonstration of the parity-violating energy difference between enantiomers. *Proc. Natl. Acad. Sci.*, 96:4252–4255, 1999. 5

[13] Benoît Darquié, Clara Stoeffler, Alexander Shelkovnikov, Christophe Daussy, Anne Amy-Klein, Christian Chardonnet, Samia Zrig, Laure Guy, Jeanne Crassous, Pascale Soulard, Pierre Asselin, Thérése R. Huet, Peter Schwerdtfeger, Radovan Bast, and Trond Saue. Progress toward the first observation of parity violation in chiral molecules by high-resolution laser spectroscopy. *Chirality*, 22(10):870–884, 2010. 5

[14] A. Moscowitz. Some applications of the kronig-kramers theorem to optical activity. *Tetrahedron*, 13(1–3):48–56, 1961. 8

[15] C. A. Emeis, L. J. Oosterhoff, and Gonda de Vries Devries. Numerical evaluation of the kramers-kronig relations. *Proc. Roy. Soc. A*, 297:54–65, 1967. 9

[16] A. Ohta and H. Ishida. Comparison among several numerical integeration methods for the kramers-kronig transformation. *Applied Spectroscopy.*, 42:952–957, 1988. 9

[17] E. U. Condon. Theories of optical rotatory power. *Rev. Mod. Phys.*, 9:432–457, Oct 1937. 11, 45

[18] Prasad L. Polavarapu. Optical rotation: Recent advances in determining the absolute configuration. *Chirality*, 14(10):768–781, 2002. 12, 92, 94

[19] W. Moffitt, R. B. Woodward, A. Moscowitz, A. W. Klyne, and J. C. Djerassi. *J. Am. Chem. Soc.*, 83:4013–4018, 1961. 12

[20] William Moffitt, R. B. Woodward, A. Moscowitz, W. Klyne, and Carl Djerassi. Structure and the optical rotatory dispersion of saturated ketones. *J. Amer. Chem. Soc.*, 83(19):4013–4018, 1961. 12

[21] T. Crawford. Ab initio calculation of molecular chiroptical properties. *Theor. Chem. Acc.*, 115(4):227–245, April 2006. 12, 18

[22] Christian Reichardt. *Solvents and Solvent effects in Organic Chemistry.* Wiley, 3 edition, 2003. 15, 16, 17, 23

[23] R E Ballard, S F Mason, and G W Vane. Circular dichroism of dissymmetric ketones. *Discussions of the Faraday Society*, 35:43–47, 1963. 15, 27, 41, 42, 43

[24] Takayuki Suga and Kiyoshi Imamura. Stereochemical studies of monoterpene compounds. xvii. a conformational study of monoterpene. *Bulletin of the Chemical Society of Japan*, 45(7):2060–2064, 1972. 15, 41

[25] Toru Egawa, Yukari Kachi, Tsuguhide Takeshima, Hiroshi Takeuchi, and Shigehiro Konaka. Structural determination of carvone, a component of spearmint, by means of gas electron diffraction augmented by theoretical calculations. *Journal of Molecular Structure*, 658(3):241–251, 2003. 16

[26] Masahiro Mineyama and Toru Egawa. Conformational property of carvone as studied by laser-jet spectroscopy and theoretical calculations. *J. Molec. Struc.*, 734(1-3):61–65, 2005. ISSN 0022-2860. 16, 36

[27] Branislav Jansik, Antonio Rizzo, Luca Frediani, Kenneth Ruud, and Sonia Coriani. Combined density functional/polarizable continuum model study of magnetochiral birefringence: Can theory and experiment be brought to agreement? *J. Chem. Phys.*, 125(23):234105, 2006. 16, 20

[28] R. W. Taft, Jose-Luis M. Abboud, and Mortimer J.Kamlet. Solvatochromic comparison method. 20. linear solvation energy relationships. 12. the δ term in the solvatochromic equations. *J. Amer. Chem. Soc.*, 103(5):1080–1086, March 1981. 16

[29] Andrew T. Fischer, Robert N. Compton, and Richard M. Pagni. Solvent effects on the optical rotation of (S)-$(-)$-α-methylbenzylamine. *J. Phys. Chem. A*, 110(22): 7067–7071, June 2006. 18, 24

[30] Yizhak Marcus. *The Properties of solvents*. Wiley, 1998. 16

[31] Suman Lata, K.C. Singh, and Suman Ahlawat. A study of dielectric properties and refractive indices of aniline +benzene, +toluene, +o-xylene, and +p-xylene at 298.15k. *Journal of Molecular Liquids*, 147(3):191–197, August 2009. 17

[32] Mortimer J. Kamlet and R. W. Taft. The solvatochromic comparison method. i. the β-scale of solvent hydrogen-bond acceptor (hba) basicities. *J. Amer. Chem. Soc.*, 98 (2):377–383, January 1976. 18

[33] Mortimer J. Kamlet, Mary Elizabeth Jones, Robert W. Taft, and J.L Abboud. Linear solvation energy relationships. part 2. correlations of electronic spectral data for aniline indicators with solvent $\pi^\star$ and β values. *J. Chem. Soc., Perkin Trans. 2*, (3), 1979. 18

[34] Mortimer J. Kamlet and Robert W. Taft. Linear solvation energy relationships. part 1. solvent polarity–polarizability effects on infrared spectra. *Perkin Trans. 2*, pages 373–341, 1979. 18

[35] M. Pecul and K. Ruud. The ab initio calculation of optical rotation and electronic circular dichroism. *Adv. Quantum Chem.*, 50:185–212, 2005. 18

[36] T. Daniel Crawford, Mary C. Tam, and Micah L. Abrams. The current state of ab initio calculations of optical rotation and electronic circular dichroism spectra. *J. Phys. Chem. A*, 111(48):12057–12068, December 2007.

[37] P. L. Polavarapu. Renaissance in chiroptical spectroscopic methods for molecular structure. *Chem. Rec.*, 7:125–136, 2007.

[38] T. D. Crawford and P. J. Stephens. A comparison of time-dependent density-functional theory and coupled cluster theory for the calculation of the optical rotations of chiral molecules. *J. Phys. Chem. A*, 112:1339–1345, 2008. 18

[39] J. Autschbach. Computing chiroptical properties wth first-principles theoretical methods: Background and illustrative examples. *Chirality*, 21:E116–E152, 2009. 18

[40] T. B. Pedersen, J. Kongsted, and T. D. Crawford. Gas phase optical rotation calculated from coupled cluster theory with zero-point vibrational corrections from density functional theory. *Chirality*, 21:S68–S75, 2009. 18, 94

[41] K. Ruud, P. J. Stephens, F. J. Devlin, P. R. Taylor, J. R. Cheeseman, and M. J. Frisch. Coupled-cluster calculations of optical rotation. *Chem. Phys. Lett.*, 373:606–614, 2003. 18, 20

[42] Mary C. Tam, Nicholas J. Russ, and T. Daniel Crawford. Coupled cluster calculations of optical rotatory dispersion of (S)-methyloxirane. *J. Chem. Phys.*, 121(8):3550–3557, 2004. 18, 20, 33

[43] J. Kongsted, T. B. Pedersen, M. Strange, A. Osted, Aa. E. Hansen, K. V. Mikkelsen, F. Pawlowski, P. Jorgensen, and C. Hättig. Coupled cluster calculations of the optical rotation of (S)-propylene oxide in gas phase and solution. *Chem. Phys. Lett.*, 401 (4-6):385–392, 2005. 18

[44] Kenneth Ruud and Riccardo Zanasi. The importance of molecular vibrations: The sign change of the optical rotation of methyloxirane. *Ange. Chemie Int. Ed.*, 44(23): 3594–3596, 2005. 94

[45] J. Kongsted, T. B. Pedersen, L. Jensen, Aa. E. Hansen, and K. V. Mikkelsen. Coupled cluster and density functional theory study of the vibrational contribution to the optical rotation of (S)-propylene oxide. *J. Am. Chem. Soc.*, 128(3):976–982, 2006. 18, 33

[46] T. D. Crawford, M. C. Tam, and M. L. Abrams. The problematic case of (S)-methylthiirane: Electronic circular dichroism spectra and optical rotatory dispersion. *Mol. Phys.*, 105:2607–2617, 2007. 33

[47] T. B. Pedersen, J. Kongsted, T. D. Crawford, and K. Ruud. On the importance of vibrational contributions to small-angle optical rotation: fluorooxirane in gas phase and solution. *J. Chem. Phys.*, 130:034310, 2009. 18, 94

[48] T Muller, Kenneth B. Wiberg, and Patrick Vaccaro. *J. Phys. Chem. A.*, 104:5959, 2000. 18

[49] S. M. Wilson, K. B. Wiberg, J. R. Cheeseman, M. J. Frisch, and P. H. Vaccaro. The nonresonant optical activity of isolated organic molecules. *J. Phys. Chem. A*, 109(51): 11752–11764, 2005. 18, 29

[50] K. B. Wiberg, P. H. Vaccaro, and J. R. Cheeseman. Conformational effects on optical rotation. 3-substituted 1-butenes. *J. Am. Chem. Soc.*, 125:1888–1896, 2003. 19, 20, 98, 107

[51] K. B. Wiberg, Y.-G. Wang, P. H. Vaccaro, J. R. Cheeseman, and M. R. Luderer. Conformation effects on optical rotation. 2-substituted butanes. *J. Phys. Chem. A*, 109(15):3405–3410, 2005.

[52] M. C. Tam, M. L. Abrams, and T. D. Crawford. Chiroptical properties of (*R*)-3-chloro-1-butene and (*R*)-2-chlorobutane. *J. Phys. Chem. A*, 111(44):11232–11241, 2007.

[53] T. D. Crawford and W. D. Allen. Optical activity in conformationally flexible molecules: A theoretical study of large-amplitude vibrational averaging in (*R*)-3-chloro-1-butene. *Mol. Phys.*, 107:1041–1057, 2009. 19

[54] John G. Kirkwood. Theory of solutions of molecules containing widely separated charges with special application to zwitterions. *J. Chem. Phys.*, 2(7):351–361, July 1934. 19

[55] M. Born. Volumen und hydratationswärme der ionen. *Zeitschrift für Physik A Hadrons and Nuclei*, 1(1):45–48, February 1920. 19

[56] Lars Onsager. Electric moments of molecules in liquids. *J. Am. Chem. Soc.*, 58(8): 1486–1493, August 1936. 19

[57] Jacopo Tomasi. Thirty years of continuum solvation chemistry: a review, and prospects for the near future. *Theor. Chem. Acc.*, 112(4):184–203, September 2004. 19

[58] B. Mennucci, J. Tomasi, R. Cammi, J. R. Cheeseman, M. J. Frisch, F. J. Devlin, S. Gabriel, and P. J. Stephens. Polarizable continuum model (pcm) calculations of solvent effects on optical rotations of chiral molecules. *J. Phys. Chem. A*, 106(25): 6102–6113, June 2002. 19, 94

[59] M. Pecul, D. Marchesan, K. Ruud, and S. Coriani. Polarizable continuum model study of solvent effects on electronic circular dichroism parameters. *J. Chem. Phys.*, 122(2): 024106, 2005. 19

[60] P. J. Stephens, F. J. Devlin, C. F. Chabalowski, and M. J. Frisch. *Ab initio* calculation of vibrational absorption and circular dichroism spectra using density functional theory. *J. Phys. Chem.*, 98(45):11623–11627, 1994. 20

[61] A. D. Becke. Density-functional thermochemistry. iii. the role of exact exchange. *J. Chem. Phys.*, 98:5648–5652, 1993.

[62] C. Lee, W. Yang, and R. G. Parr. Development of the colle-salvetti correlation-energy formula into a functional of the electron density. *Phys. Rev. B.*, 37:785–789, 1988. 20, 64

[63] L. A. Curtiss and K. Raghavachari. Gaussian3 and related methods for accurate thermochemistry. *Theor. Chem. Acc.*, 108:61–70, 2002. 20

[64] M. J. Frisch, G. W. Trucks, H. B. Schlegel, G. E. Scuseria, M. A. Robb, J. R. Cheeseman, Jr. J. A. Montgomery, T. Vreven, K. N. Kudin, J. C. Burant, J. M. Millam, S. S. Iyengar, J. Tomasi, V. Barone, B. Mennucci, M. Cossi, G. Scalmani, N. Rega, G. A. Petersson, H. Nakatsuji, M. Hada, M. Ehara, K. Toyota, R. Fukuda, J. Hasegawa, M. Ishida, T. Nakajima, Y. Honda, O. Kitao, H. Nakai, M. Klene, X. Li, J. E. Knox, H. P. Hratchian, J. B. Cross, V. Bakken, C. Adamo, J. Jaramillo, R. Gomperts, R. E. Stratmann, O. Yazyev, A. J. Austin, R. Cammi, C. Pomelli, J. W. Ochterski, P. Y. Ayala, K. Morokuma, G. A. Voth, P. Salvador, J. J. Dannenberg, V. G. Zakrzewski, S. Dapprich, A. D. Daniels, M. C. Strain, O. Farkas, D. K. Malick, A. D. Rabuck, K. Raghavachari, J. B. Foresman, J. V. Ortiz, Q. Cui, A. G. Baboul, S. Clifford, J. Cioslowski, B. B. Stefanov, G. Liu, A. Liashenko, P. Piskorz, I. Komaromi, R. L. Martin, D. J. Fox, T. Keith, M. A. Al-Laham, C. Y. Peng, A. Nanayakkara, M. Challacombe, P. M. W. Gill, B. Johnson, W. Chen, M. W. Wong, C. Gonzalez, and J. A. Pople. Gaussian 03, Revision C.02, . Gaussian, Inc., Wallingford, CT, 2004. 20, 21, 96

[65] T. D. Crawford and H. F. Schaefer. An introduction to coupled cluster theory for computational chemists. In K. B. Lipkowitz and D. B. Boyd, editors, *Reviews in Computational Chemistry*, volume 14, chapter 2, pages 33–136. VCH Publishers, New York, 2000. 20

[66] I. Shavitt and R. J. Bartlett. *Many-Body Methods in Chemistry and Physics: MBPT and Coupled-Cluster Theory*. Cambridge University Press, Cambridge, 2009.

[67] H. Koch and P. Jorgensen. Coupled cluster response functions. *J. Chem. Phys.*, 93 (5):3333–3344, 1990. 20

[68] O. Christiansen, H. Koch, and P. Jørgensen. The second-order approximate coupled cluster singles and doubles model cc2. *Chem. Phys. Lett.*, 243:409–418, 1995. 20

[69] M. E. Casida. *Recent Advances in Density Functional Methods*, volume 1. World Scientific, Singapore, 1995. 20

[70] J. R. Cheeseman, M. J. Frisch, F. J. Devlin, and P. J. Stephens. Hartree-fock and density functional theory ab initio calculation of optical rotation using giaos: Basis set dependence. *J. Phys. Chem. A*, 104:1039–1046, 2000. 20

[71] F. London. Théorie quantique des courants interatomiques dans les combinaisons aromatiques. *J. Phys. Radium*, 8(10):397–409, 1937.

[72] R. Ditchfield. Self-consistent perturbation theory of diamagnetism. i. a gauge-invariant lcao method for n.m.r. chemical shifts. *Mol. Phys.*, 27(4):789–807, 1974. 20

[73] T. B. Pedersen, H. Koch, L. Boman, and A. M. J. S. de Meras. Origin invariant calculation of optical rotation without recourse to london orbitals. *Chem. Phys. Lett.*, 393(4-6):319–326, 2004. 20

[74] T H Dunning. Gaussian basis sets for use in correlated molecular calculations. i. the atoms boron through neon. *J. Chem. Phys.*, 90(2):1007, 1989. 20, 97

[75] D. E. Woon and T. H. Dunning. Gaussian basis sets for use in correlated molecular calculations. iv. calculation of static electrical response properties. *J. Chem. Phys.*, 100(4):2975, 1994. 20

[76] Chris J. Harding and Ivan Powis. Sensitivity of photoelectron circular dichroism to structure and electron dynamics in the photoionization of carvone and related chiral monocyclic terpenone enantiomers. *J. Chem. Phys.*, 125(23):234306, 2006. 20

[77] D. A. McQuarrie. *Statistical Thermodynamics*. University Science Books, Mill Valley, California, 1973. 20, 97

[78] W. J. Hehre, L. Radom, P. v.R. Schleyer, and J. A. Pople. *Ab Initio Molecular Orbital Theory*. John Wiley and Sons, New York, 1986. 20, 97

[79] M. J. Frisch, G. W. Trucks, H. B. Schlegel, G. E. Scuseria, M. A. Robb, J. R. Cheeseman, G. Scalmani, V. Barone, B. Mennucci, G. A. Petersson, H. Nakatsuji, M. Caricato, X. Li, H. P. Hratchian, A. F. Izmaylov, J. Bloino, G. Zheng, J. L. Sonnenberg, M. Hada, M. Ehara, K. Toyota, R. Fukuda, J. Hasegawa, M. Ishida, T. Nakajima, Y. Honda, O. Kitao, H. Nakai, T. Vreven, J. A. Montgomery, Jr., J. E. Peralta, F. Ogliaro, M. Bearpark, J. J. Heyd, E. Brothers, K. N. Kudin, V. N. Staroverov, R. Kobayashi, J. Normand, K. Raghavachari, A. Rendell, J. C. Burant, S. S. Iyengar, J. Tomasi, M. Cossi, N. Rega, J. M. Millam, M. Klene, J. E. Knox, J. B. Cross, V. Bakken, C. Adamo, J. Jaramillo, R. Gomperts, R. E. Stratmann, O. Yazyev, A. J. Austin, R. Cammi, C. Pomelli, J. W. Ochterski, R. L. Martin, K. Morokuma, V. G. Zakrzewski, G. A. Voth, P. Salvador, J. J. Dannenberg, S. Dapprich, A. D. Daniels, Ö. Farkas, J. B. Foresman, J. V. Ortiz, J. Cioslowski, and D. J. Fox. Gaussian 09 Revision A.1, . 21, 64

[80] T. D. Crawford, C. D. Sherrill, E. F. Valeev, J. T. Fermann, R. A. King, M. L. Leininger, S. T. Brown, C. L. Janssen, E. T. Seidl, J. P. Kenny, and W. D. Allen. Psi3: An open-source ab initio electronic structure package. *J. Comp. Chem.*, 28: 1610–1616, 2007. 21

[81] Larry A. Curtiss, Paul C. Redfern, Krishnan Raghavachari, Vitaly Rassolov, and John A. Pople. Gaussian-3 theory using reduced moller-plesset order. *J. Chem. Phys.*, 110(10):4703–4709, 1999. 21

[82] H Landolt. *The Optical Rotating Power of Organic Substances and its Applications*. Chemical Publishing Co., 1902. 22

[83] E. Eliel, S Wilen, , and M. Doyle. *Basic Organic Stereochemistry*. Wiley-Interscience, 2001.

[84] Prasad L. Polavarapu, Ana Petrovic, and Feng Wang. Intrinsic rotation and molecular structure. *Chirality*, 15(S1):S143–S149, 2003. 22, 92

[85] H. Gordon Rule and Andrew McLean. Xciii.-studies in solvent action. part i. influence of polar solvents on the rotatory power of l-menthyl methyl naphthalate. *Journal of the American Chemical Society*, 1931. 23

[86] H. G. Rule and J. P. Cunningham. Studies in solvent action. part x. rotatory powers of dimethylene tartrate, methylenetartaric acid and its dimethyl ester, in the presence of added solvents and salts. *J. Chem. Soc.*, pages 1038–1043, 1935. 23

[87] Yoshiyuki Kumata, Junji Furukawa, and Takayuki Fueno. The effect of solvents on the optical rotation of poly(propylene oxide). *Bull. Chem. Soc. Jpn*, 43:3663–3666, 1970. 23

[88] Kenneth B. Wiberg, Yi gui Wang, Shaun M. Wilson, Patrick H. Vaccaro, and James R. Cheeseman. Chiroptical properties of 2-chloropropionitrile. *J. Phys. Chem. A*, 105: 3448–3453, 2005. 24

[89] Nathan Hammer, Kadir Diri, Kenneth D Jordan, and and Robert N Compton Charles Desfrançois. Dipole-bound anions of carbonyl, nitrile, and sulfoxide containing molecules. *J. Chem. Phys.*, 119(7):3650–3660, August 2003. 29

[90] Charles Desfrançois, Hassan Abdoul-Carime., and Jean-Pierre Schermann. Ground state dipole-bound anions. *Int. J. Mod. Phys. B*, 10:1339–1395, 1996.

[91] R. C. Fortenberry and T. D. Crawford. Theoretical prediction of new dipole-bound singlet states for anions of interstellar interest. *J. Chem. Phys.*, 134:154304, 2011.

[92] R. C. Fortenberry and T. D. Crawford. Singlet excited states of silicon-containing anions relevant to interstellar chemistry. *J. Phys. Chem. A*, 115:8119–8124, 2011.

[93] J. Simons. Theoretical study of negative molecular ions. *Ann. Rev. Phys. Chem.*, 62: 107–128, 2011. 29

[94] Th. Klahn and P. Krebs. Electron and anion mobility in low density hydrogen cyanide gas. ii. evidence for the formation of anionic clusters. *J. Chem. Phys.*, 109(2):543–550, July 1998. 29

[95] P. Mikulski, Th. Klahn, and P. Krebs. Excess electron mobility in low density ch3cn gas: Short-lived dipole-bound electron ground states as precursors of localized electron states. *Phys. Rev. A*, 55(1):369, January 1997. 29

[96] S. Ard, W.R. Garrett, R.N. Compton, L. Adamowicz, and S.G. Stepanian. Rotational states of dipole-bound anions of hydrogen cyanide. *Chem. Phys. Lett.*, 473(4-6):223–226, May 2009. 29

[97] Johannes Neugebauer, Evert Jan Baerends, Marcel Nooijen, and Jochen Autschbach. Importance of vibronic effects on the circular dichroism spectrum of dimethyloxirane. *J. Chem. Phys.*, 122(23):234–305, 2005. 34

[98] Marcel Nooijen. Investigation of herzberg-teller franck-condon approaches and classical simulations to include effects due to vibronic coupling in circular dichroism spectra: The case of dimethyloxirane continued. *Int. J. Quantum Chem.*, 106(12): 2489–2510, 2006. 34, 94

[99] Lorenzo Di Bari and Gennaro Pescitelli. *Computational Spectroscopy Methods, Experiments and Applications.* Wiley, 2010. 35, 98

[100] Watheq Ahmad Al-Basheer. *Linear and nonlinear chiroptical effects.* PhD thesis, University of Tennessee, 2006. 41, 42

[101] Watheq Al-Basheer, Richard Pagni, and Robert N. Compton. Spectroscopic and theoritical investigations of *R*-(-)-3-methycyclopentanone. the effects of solvents and

temperature on the distribution of conformers. *J. Phys. Chem. A.*, 111:2293–2298, 2007. 43

[102] Kenneth B. Wiberg, Yi gui Wang, Michael J. Murphy, and Patrick H. Vaccaro. Temperature dependence of optical rotation: α-pinene, β-pinene pinane, camphene, camphor and fenchone. *J. Phys. Chem.*, 108:5559–5563, 2004. 43

[103] F. M. Menger and B. Boyer. Solvent effects on comformation dependent optical rotatory dispersion spectra. *J. Org. Chem.*, 49:1826–1828, 1984. 47, 92

[104] C Desfrancois, V Periquet, S A Lyapustina, T P Lippa, D W Robinson, K H Bowen, H Nonaka, and R N Compton. Electron binding to valence and multipole states of molecules: Nitrobenzene, para- and meta-dinitrobenzenes. *J. Chem. Phys.*, 111(10): 4569–4576, 1999. 56, 77, 87, 89

[105] Shuhao Wen, Kaushik Nanda, Yuanhang Huang, and Gregory J O Beran. Practical quantum mechanics-based fragment methods for predicting molecular crystal properties. *Phys. Chem. Chem. Phys*, 14(21):7578–7590, 2012. 57

[106] C J Noren, S J Anthony-Cahill, M C Griffith, and P G Schultz. A general method for site-specific incorporation of unnatural amino acids into proteins. *Science*, 244(4901): 182–188, April 1989. 58

[107] Jianming Xie and Peter G Schultz. A chemical toolkit for proteins [mdash] an expanded genetic code. *Nat Rev Mol Cell Biol*, 7(10):775–782, October 2006. 58

[108] Dennis A Dougherty. Unnatural amino acids as probes of protein structure and function. *Current Opinion in Chemical Biology*, 4(6):645–652, 2000. ISSN 1367-5931. doi: 10.1016/S1367-5931(00)00148-4.

[109] David B F Johnson, Jianfeng Xu, Zhouxin Shen, Jeffrey K Takimoto, Matthew D Schultz, Robert J Schmitz, Zheng Xiang, Joseph R Ecker, Steven P Briggs, and Lei Wang. Rf1 knockout allows ribosomal incorporation of unnatural amino acids at multiple sites. *Nat. Chem. Biol.*, 7(11):779–786, November 2011. 58

[110] Teresa Kowalik-Jankowska, Henryk Kozlowski, Krzysztof Pawelczak, and Maciej Makowski. N-p-amino-and n-p-nitro-phenylsulfonyl derivatives of dipeptides, a new family of ligands for copper(ii). potentiometric and spectroscopic studies. *J. Chem. Soc., Dalton Trans.*, pages 2729–2733, 1995. 58

[111] Maria Luisa Di Gioia, Antonella Leggio, Adolfo Le Pera, Angelo Liguori, and Carlo Siciliano. Optically pure n-hydroxy-o-triisopropylsilyl-α-l-amino acid methyl esters from alcl3-assisted ring opening of chiral oxaziridines by nitrogen containing nucleophiles. *J. Org. Chem.*, 70(25):10494–10501, 2005. 58

[112] Paolo Lo Meo, Francesca D'Anna, Michelangelo Gruttadauria, Serena Riela, and Renato Noto. Thermodynamics of binding between α- and β-cyclodextrins and some p-nitro-aniline derivatives: reconsidering the enthalpy-entropy compensation effect. *Tetrahedron*, 60(41):9099–9111, October 2004. 59

[113] D. M. Neumark, K. R. Lykke, T. Andersen, and W. C Lineberger. Laser photodetachment measurement of the electron affinity of atomic oxygen. *Phys. Rev. A: Gen. Phys.*, 32:1890–1892, 1985. 61

[114] B. H. Smith, A. Buonaugurio, J. Chen, E. Collins, K H Bowen, R.N. Compton, and T. Sommerfield. No Title. 2013. 61, 71

[115] Kent M. Ervin and P. B. Armentrout. Translational energy dependence of ar+xyarx+y (xy=h_2,d_2,h d) from thermal to 30 ev c.m. *J. Chem. Phys.*, 83(1):166, 1985. 62, 89

[116] M. E. Weber, J. L. Elkind, and P. B. Armentrout. Kinetic energy dependence of $al^+ + o_2 \rightarrow alo^+ + o$. *J. Chem. Phys.*, 84(3):1521, 1986. doi: 10.1063/1.450497.

[117] N F Dalleska, Kenji Honma, L S Sunderlin, and P B Armentrout. Solvation of transition metal ions by water . sequential binding energies of m + (hzo), (x = 1-4) for m = ti to cu determined by collision-induced dissociation. *J. Am. Chem. Soc.*, 116(8):3519–3528, 1994.

[118] M T Rodgers, Kent M Ervin, and P B Armentrout. Statistical modeling of collision-induced dissociation thresholds. *J. Chem. Phys.*, 106(11):4499–4508, 1997.

[119] M. T. Rodgers and P. B. Armentrout. Statistical modeling of competitive threshold collision-induced dissociation. *J. Chem. Phys.*, 109(5):1787, 1998.

[120] P B Armentrout, Kent M Ervin, and M T Rodgers. Statistical rate theory and kinetic energy-resolved ion chemistry: theory and applications. *J. Phys. Chem. A*, 112(41): 10071–85, October 2008. 62, 63, 89

[121] G. Gioumousis and D. P. Stevenson. Reactions of gaseous molecule ions with gaseous molecules. v. theory. *J. Chem. Phys.*, 29:294, 1958. 62

[122] T Beyer and D.R. Swineheart. *ACM commun*, 16:379, 1973. 63

[123] Stephen E. Stein and B.S. Rabinovitch. On the use of exact state counting methods in rrkm rate calculations. *Chem. Phys. Lett.*, 49:183–188, 1977. 63

[124] C. Lifshitz, R.L.C. Wu, T.O. Tiernan, and D. T. Terwilliger. Negative ion-molecule reactions of ozone and their implications on the thermochemistry of o_3^-. *J. Chem. Phys.*, 68:247, 1987. 63, 89

[125] T. H. Dunning. Gaussian basis sets for use in correlated molecular calculations. i. the atoms boron through neon. *J. Chem. Phys.*, 90(2):1007, 1989. 64

[126] Rick A Kendall, Jr. Thom H. Dunning, and Robert J Harrison. Electron affinities of the first-row atoms revisited. systematic basis sets and wave functions. *J. Chem. Phys.*, 96(9):6796–6806, 1992. doi: 10.1063/1.462569.

[127] Florian Weigend and Reinhart Ahlrichs. Balanced basis sets of split valence{,} triple zeta valence and quadruple zeta valence quality for h to rn: Design and assessment of accuracy. *Phys. Chem. Chem. Phys.*, 7(18):3297–3305, 2005. doi: 10.1039/B508541A.

[128] Ewa Papajak and Donald G Truhlar. Efficient diffuse basis sets for density functional theory. *Journal of Chemical Theory and Computation*, 6(3):597–601, 2010. 64

[129] Yan Zhao and Donald G Truhlar. Comparative dft study of van der waals complexes: Rare-gas dimers, alkaline-earth dimers, zinc dimer, and zinc-rare-gas dimers. *J. Phys. Chem. A*, 110(15):5121–5129, 2006. 64

[130] John P Perdew. Density-functional approximation for the correlation energy of the inhomogeneous electron gas. *Phys. Rev. B*, 33(12):8822–8824, June 1986.

[131] A D Becke. Density-functional exchange-energy approximation with correct asymptotic behavior. *Physical Review A*, 38(6):3098–3100, September 1988.

[132] A D Becke. Density-functional thermochemistry. iii. the role of exact exchange. *J. Chem. Phys.*, 98:5648–5652, 1993.

[133] Nicholas C Handy and Aron J. Cohen. Left-right correlation energy. *Molecular Physics*, 99(5):403–412, 2001.

[134] Jianmin Tao, John P Perdew, Viktor N Staroverov, and Gustavo E Scuseria. Climbing the density functional ladder: Nonempirical meta\char21{}generalized gradient approximation designed for molecules and solids. *Phys. Rev. Lett.*, 91(14): 146401, September 2003. 64

[135] F. Neese, U. Beeker, D. Gauiouchine, S. Koß mann, T Petrenko, C. Riplinger, and F. Wennmohs. Orca vers. 2.8.0, 2010. 64

[136] J.F. Stanton, J. Gauss, M.E. Harding, P.G. Szalay, Auer, with contributions From, A.A., Bartlett, R.J., Benedikt, U., Berger, C., Bernholdt, D.E., Bomble, Y.J., Cheng, L., Christiansen, O., Heckert, M., Heun, Huber, Jagau, T.-C., Jonsson, D., Jusélius, J., Klein, K., Lauderdale, W.J., D.A., Matthews, T. Metzroth, L.A. Mück, D.P. O'Neill, D.R. Price, E. Prochnow, C. Puzzarini, K. Ruud, F. Schiffmann, W. Schwalbach, S. Stopkowicz, A. Tajti, J. Vázquez, F. Wang, , the Integral, and See packages MOLECULE (J. Almlöf and P.R. Taylor), PROPS (P.R. Taylor), ABACUS (T. Helgaker, H.J. Aa. Jensen, P. Jørgensen, and J. Olsen), and ECP routines by A. V. Mitin and C. van Wüllen. For the current version. CFOUR, Coupled-Cluster techniques for Computational Chemistry, a quantum-chemical program package by. URL http://www.cfour.de. 64

[137] H.Y. Afeefy, J.F. Liebman, and S.E. Stein. *NIST Chemistry WebBook, NIST Standard Reference Database Number 69*. National Institute of Standards and Technology, Gaithersburg MD, 2010. URL http://webbook.nist.gov. 68

[138] Miriam Karni and Asher Mandelbaum. The even-electron rule. *Organic Mass Spectrometry*, 15(2):53–64, February 1980. 69

[139] Karsten Levsen, Hans-Martin Schiebel, Johan K Terlouw, Karl J Jobst, Manfred Elend, Alfred Preiss, Herbert Thiele, and Arnd Ingendoh. Even-electron ions: a systematic study of the neutral species lost in the dissociation of quasi-molecular ions. *Journal of mass spectrometry : JMS*, 42(8):1024–1044, August 2007. 69

[140] Zhen Wang, Cornelis E C A Hop, Mi-Sook Kim, Su-E W Huskey, Thomas A Baillie, and Ziqiang Guan. The unanticipated loss of so_2 from sulfonamides in collision-induced dissociation. *Rapid communications in mass spectrometry : RCM*, 17(1):81–6, January 2003. ISSN 0951-4198. doi: 10.1002/rcm.877. URL http://www.ncbi.nlm.nih.gov/pubmed/12478558. 69

[141] C D Cooper and R N Compton. Metastable anions of co2. *Chem. Phys. Let.*, 14(1): 29–32, 1972. 71

[142] Khanh Do, Timothy P. Klein, Cynthia Ann Pommerening, and Lee S. Sunderlin. A new flowing afterglow-guided ion beam tandem mass spectrometer. applications to the thermochemistry of polyiodide ions. *Journal of the American Society for Mass Spectrometry*, 8(7):688–696, July 1997. 71, 89

[143] P. J. Hay and W. R. Wadt. No Title. *J. Chem. Phys.*, 82:270–283, 1985. 72

[144] P. J. Hay and W. R. Wadt. No Title. *J. Chem. Phys.*, 82:299–310, 1985.

[145] W. R. Wadt and P. J. Hay. No Title. *J. Chem. Phys.*, 82:284–298, 1985. 72

[146] F W Parrett and N J Taylor. Spectroscopic studies on some polyhalide ions. *Journal of Inorganic and Nuclear Chemistry*, 32(7):2458–2461, July 1970. 72

[147] Pankaj Sinha, Scott E Boesch, Changming Gu, Ralph A Wheeler, and Angela K Wilson. Harmonic vibrational frequencies: Scaling factors for hf, b3lyp, and mp2 methods in combination with correlation consistent basis sets. *J. Phys. Chem. A*, 108 (42):9213–9217, October 2004. 73

[148] Ewa Papajak, Jingjing Zheng, Xuefei Xu, Hannah R. Leverentz, and Donald G. Truhlar. Perspectives on basis sets beautiful: Seasonal plantings of diffuse basis functions. *Journal of Chemical Theory and Computation*, 7(10):3027–3034, 2011. 80

[149] Alexandre a. Shvartsburg, Kent M. Ervin, and John H. Frederick. Models for statistical decomposition of metal clusters: Vibrational frequency distributions. *J. Chem. Phys.*, 104(21):8458, 1996. 89

[150] James B. Griffin and P. B. Armentrout. Guided ion beam studies of the reactions of fe_n^+ (n=2-18) with o_2: Iron cluster oxide and dioxide bond energies. *J. Chem. Phys.*, 106(11):4448, 1997.

[151] P B Armentrout. Statistical modeling of sequential collision-induced dissociation thresholds. *J. Chem. Phys.*, 126(23):234302, June 2007. 89

[152] Nina Berova, Lorenzo Di Bari, and Gennaro Pescitelli. Application of electronic circular dichroism in configurational and conformational analysis of organic compounds. *Chem. Soc. Rev.*, 36(6):914–931, 2007. 91, 93, 94

[153] Prasad L. Polavarapu, Dilip K. Chakraborty, and Kenneth Ruud. Molecular optical rotation: an evaluation of semiempirical models. *Chem. Phys. Lett.*, 319(5-6):595–600, March 2000. ISSN 0009-2614. 92

[154] Egidio Giorgio, Rosario G. Viglione, Riccardo Zanasi, and Carlo Rosini. Ab initio calculation of optical rotatory dispersion (ord) curves: A simple and reliable approach to the assignment of the molecular absolute configuration. *J. Amer. Chem. Soc.*, 126: 12968–12976, 2004. 92, 94

[155] Johannes Neugebauer. Induced chirality in achiral media-how theory unravels mysterious solvent effects. *Angew. Chem. Int. Ed. Engl.*, 46:7738–7740, 2007. 93, 113

[156] Jason Lambert, R. N. Compton, and T. Daniel Crawford. The optical activity of carvone:a theoretical and experimental investigation. *J. Chem. Phys.*, 136:114512, 2012. 94

[157] D. M. McCann and P. J. Stephens. Determination of absolute configuration using density functional theory calculations of optical rotation and electronic circular dichroism: Chiral alkenes. *The Journal of Organic Chemistry*, 71(16):6074–6098, 2006. 94

[158] D. M. McCann, P. J. Stephens, and J. R. Cheeseman. Determination of absolute configuration using density functional theory calculation of optical rotation: Chiral alkanes. *J. Org. Chem.*, 69(25):8709–8717, December 2004. 94

[159] N. Harada and K Nakanishi. *Circular Dichroism Spectroscopy: Exciton coupling in Organic Stereochemistry*. University Science Books, 1983. 94

[160] Gerhard Bringmann, Torsten Bruhn, Katja Maksimenka, and Yasmin Hemberger. The Assignment of Absolute Stereostructures through Quantum Chemical Circular Dichroism Calculations. *European Journal of Organic Chemistry*, 2009(17):2717–2727, June 2009. 94, 98

[161] E Cances, B Mennucci, and J Tomasi. A new integral equation formalism for the polarizable continuum model: Theoretical background and applications to isotropic and anisotropic dielectrics. *J. Chem. Phys.*, 107(8):3032–3041, 1997. 96

[162] Anwar G. Baboul, Larry a. Curtiss, Paul C. Redfern, and Krishnan Raghavachari. Gaussian-3 theory using density functional geometries and zero-point energies. *J. Chem. Phys.*, 110(16):7650, 1999. 97

[163] Philip J Stephens and Nobuyuki Harada. Ecd cotton effect approximated by the gaussian curve and other methods. *Chirality*, 22(2):229–330, February 2010. 98

[164] Takayuki Fukuyama, Koichi Matsuo, and Kunihiko Gekko. Vacuum-ultraviolet electronic circular dichroism of l-alanine in aqueous solution investigated by time-dependent density functional theory. *J. Phys. Chem. A*, 109(31):6928, August 2005. 100, 101, 103

[165] R. Abu-Eittah, A. Obaid, S. Basahl, and E. Diefallah. Molecular Orbital Treatment of Some Amino Acids. *Bulletin of the Chemical Society of Japan*, 61(7):2609–2613, 1988. 100

Appendix

A.1 Oscillator and Rotational Strengths of NPNPA and NPNPSA

Table A.1: The oscillator strength and rotatory strength of (R)-NPNPA calculated with B3LYP/aVDZ. E' is the shifted energy used to fit experimental and theoretical UV/vis absorption, f is the dimensionless oscillator strength, and R is the rotational strength in 10^{-40} erg esu cm Gauss^{-1}.

Conformer 1				Conformer 2			
E (eV)	E' (eV)	f	R	E (eV)	E' (eV)	f	R
3.316	3.151	0.576	2.018	3.366	3.197	0.538	11.906
3.770	3.581	0.000	-2.949	3.773	3.584	0.000	-8.942
4.123	3.917	0.005	-0.275	4.094	3.889	0.008	0.031
4.514	4.289	0.001	0.424	4.491	4.267	0.001	0.597
4.638	4.406	0.044	-4.604	4.742	4.505	0.007	-8.461
4.731	4.494	0.002	-2.094	4.762	4.524	0.040	-5.417
5.248	4.986	0.007	7.423	5.131	4.875	0.003	1.216
5.258	4.995	0.000	-0.285	5.279	5.015	0.009	8.087
5.567	5.289	0.049	4.367	5.649	5.367	0.045	-1.35
5.608	5.328	0.008	-2.583	5.696	5.411	0.007	1.761
5.687	5.403	0.004	2.346	5.724	5.437	0.005	23.958
5.754	5.466	0.003	0.114	5.775	5.486	0.005	-5.918
5.879	5.585	0.106	-8.496	5.906	5.611	0.099	-3.269
5.898	5.603	0.001	-5.071	5.966	5.667	0.003	1.442
6.049	5.747	0.004	-2.132	6.129	5.823	0.000	-0.748

Table A.1: Continued. The oscillator strength and rotatory strength of (R)-NPNPA calculated with B3LYP/aVDZ. E' is the shifted energy used to fit experimental and theoretical UV/vis absorption, f is the dimensionless oscillator strength, and R is the rotational strength in 10^{-40} erg esu cm Gauss^{-1}.

Conformer 3				Conformer 4			
E (eV)	E' (eV)	f	R	E (eV)	E' (eV)	f	R
3.439	3.267	0.504	-1.662	3.365	3.196	0.538	7.431
3.777	3.588	0.000	-6.931	3.773	3.584	0.000	-1.709
4.087	3.883	0.009	0.438	4.104	3.898	0.006	-0.207
4.478	4.254	0.001	-0.533	4.502	4.277	0.001	-0.069
4.806	4.566	0.039	20.837	4.587	4.358	0.028	23.816
4.877	4.633	0.010	1.030	4.919	4.673	0.018	-22.154
5.074	4.820	0.005	-17.181	5.002	4.752	0.004	-3.179
5.507	5.231	0.008	-17.694	5.325	5.059	0.004	-2.723
5.812	5.522	0.025	13.600	5.654	5.372	0.005	-2.48
5.881	5.587	0.020	-33.654	5.715	5.429	0.024	22.698
5.924	5.627	0.055	-19.178	5.742	5.455	0.032	-26.137
5.934	5.637	0.057	19.968	5.768	5.479	0.003	-0.776
5.983	5.684	0.003	-2.810	5.832	5.540	0.004	-6.9
6.016	5.716	0.013	-1.802	5.903	5.608	0.102	3.412
6.101	5.796	0.002	-0.059	6.127	5.820	0.001	4.146

Table A.1: Continued. The oscillator strength and rotatory strength of (R)-NPNPA calculated with B3LYP/aVDZ. E' is the shifted energy used to fit experimental and theoretical UV/vis absorption, f is the dimensionless oscillator strength, and R is the rotational strength in 10^{-40} erg esu cm Gauss^{-1}.

Conformer 5				Conformer 6			
E (eV)	E' (eV)	f	R	E (eV)	E' (eV)	f	R
3.333	3.166	0.543	-14.697	3.424	3.253	0.487	-5.938
3.772	3.583	0.000	8.001	3.773	3.585	0.001	10.394
4.095	3.890	0.006	0.013	4.084	3.879	0.008	-0.483
4.515	4.289	0.001	-0.901	4.476	4.253	0.001	0.076
4.673	4.439	0.009	17.316	4.842	4.600	0.037	-10.482
4.729	4.492	0.033	-18.950	4.869	4.626	0.008	-1.227
5.003	4.753	0.003	1.625	4.949	4.702	0.004	15.414
5.268	5.005	0.003	-3.268	5.498	5.223	0.006	4.903
5.582	5.303	0.035	-8.931	5.718	5.432	0.037	10.387
5.632	5.351	0.005	3.434	5.820	5.529	0.002	1.181
5.701	5.416	0.017	8.690	5.828	5.625	0.099	1.773
5.765	5.477	0.000	2.166	5.828	5.536	0.020	-4.038
5.784	5.495	0.003	-8.748	5.921	5.625	0.099	1.773
5.886	5.591	0.104	4.245	6.015	5.714	0.001	-2.038
6.080	5.776	0.001	1.815	6.115	5.809	0.002	-0.254

Table A.2: The oscillator strength and rotatory strength of (R)-NPNPA calculated with B3LYP/6-31G(d). E' is the shifted energy used to fit experimental and theoretical UV/vis absorption, f is the dimensionless oscillator strength, and R is the rotational strength in 10^{-40} erg esu cm Gauss^{-1}.

Conformer 1				Conformer 2			
E (eV)	E' (eV)	f	R	E (eV)	E' (eV)	f	R
3.307	3.043	0.480	13.21	3.637	3.346"	0.474	50.227
3.75	3.450	0.001	-13.529	3.831	3.525	0.008	-41.566
4.089	3.762	0.005	"0.454	4.270	3.928"	0.008	0.243
4.500	4.050	0.000	"0.676	4.469	4.022"	0.000	0.667
4.721	4.248	0.042	-17.83	5.064	4.557	0.043	-20.217
4.736	4.262	0.005	"6.601	5.096	4.586	0.003	1.030
5.271	4.744	0.001	-0.259	5.192	4.673	0.007	-4.419
5.469	4.922	0.044	0.431	5.774	5.197	0.002	3.289
5.585	5.027	0.001	-8.654	5.797	5.217	0.029	4.631
5.787	5.209	0.036	5.567	6.104	5.493	0.041	13.354
5.861	5.274	0.082	-0.915	6.191	5.572	0.076	-1.985
5.873	5.286	0.001	-0.022	6.234	5.610	0.000	0.043
5.938	5.344	0.001	-1.423	6.427	5.784	0.002	-2.862
6.037	5.433	0.008	-2.967	6.562	5.905	0.001	-1.177
6.147	5.532	0.000	-0.132	6.574	5.917	0.011	-4.165

Table A.2: Continued. The oscillator strength and rotatory strength of (R)-NPNPA calculated with B3LYP/6-31G(d). E' is the shifted energy used to fit experimental and theoretical UV/vis absorption, f is the dimensionless oscillator strength, and R is the rotational strength in 10^{-40} erg esu cm Gauss^{-1}.

Conformer 3				Conformer 4			
E (eV)	E' (eV)	f	R	E (eV)	E' (eV)	f	R
3.679	3.384	0.466	0.716	3.593	3.234	0.506	7.285
3.831	3.524	0.001	-10.574	3.831	3.448	0.000	-3.009
4.290	3.947	0.007	0.600	4.301	3.871	0.004	-0.390
4.470	4.023	0.000	-0.609	4.492	4.043	0.000	-0.314
4.902	4.412	0.019	-2.270	4.850	4.365	0.034	18.775
5.067	4.561	0.041	31.462	5.064	4.558	0.005	-2.732
5.335	4.801	0.005	-22.999	5.171	4.654	0.018	-21.208
5.969	5.372	0.006	-7.179	5.823	5.241	0.003	-11.153
5.979	5.381	0.002	-7.072	5.939	5.345	0.055	2.275
6.118	5.506	0.059	-4.522	6.147	5.533	0.012	-5.389
6.197	5.578	0.035	-9.316	6.198	5.579	0.079	2.092
6.204	5.583	0.048	4.989	6.236	5.612	0.001	0.947
6.452	5.807	0.006	7.197	6.408	5.767	0.000	1.227
6.536	5.882	0.002	3.510	6.493	5.844	0.148	5.855
6.572	5.914	0.016	3.450	6.524	5.872	0.000	0.473

Table A.2: Continued. The oscillator strength and rotatory strength of (R)-NPNPA calculated with B3LYP/6-31G(d). E' is the shifted energy used to fit experimental and theoretical UV/vis absorption, f is the dimensionless oscillator strength, and R is the rotational strength in 10^{-40} erg esu cm Gauss^{-1}.

Conformer 5				Conformer 6			
E (eV)	E' (eV)	f	R	E (eV)	E' (eV)	f	R
3.549	3.194	0.516	-18.471	3.652	3.287	0.456	-12.337
3.834	3.451	0.001	10.555	3.830	3.447	0.002	19.735
4.296	3.866	0.003	0.116	4.288	3.859	0.007	-1.039
4.501	4.051	0.000	-0.377	4.470	4.023	0.000	-0.065
4.878	4.390	0.026	21.665	4.911	4.420	0.015	2.280
4.978	4.480	0.025	-25.833	5.074	4.566	0.042	-6.104
5.105	4.594	0.005	3.810	5.241	4.717	0.001	2.962
5.851	5.266	0.002	4.433	5.936	5.342	0.007	16.331
5.898	5.308	0.056	-5.672	6.006	5.405	0.004	0.229
6.117	5.505	0.013	0.409	6.019	5.417	0.045	-5.142
6.193	5.574	0.081	0.351	6.136	5.522	0.016	0.364
6.240	5.616	0.001	0.858	6.194	5.575	0.077	0.811
6.445	5.800	0.000	-0.607	6.432	5.789	0.000	0.640
6.513	5.861	0.023	-10.352	6.538	5.885	0.006	-3.268
6.564	5.907	0.000	-0.047	6.563	5.906	0.008	2.579

Table A.3: The oscillator strength and rotatory strength of (S)-NPNPSA calculated with B3LYP/apVDZ. E' is the shifted energy used to fit experimental and theoretical UV/vis absorption, f is the dimensionless oscillator strength, and R is the rotational strength in 10^{-40} erg esu cm Gauss^{-1}.

Conformer 1				Conformer 2			
E (eV)	E' (eV)	f	R	E (eV)	E' (eV)	f	R
3.726	4.099	0.000	-0.352	3.729	4.102	0.000	-2.501
4.026	4.429	0.000	1.262	3.952	4.347	0.000	-3.243
4.070	4.477	0.119	-9.107	4.091	4.500	0.132	-2.565
4.318	4.750	0.000	-0.589	4.326	4.758	0.000	0.237
4.478	4.702	0.182	-9.306	4.630	4.862	0.154	6.387
4.824	5.066	0.101	7.231	4.746	4.983	0.056	-7.655
5.026	5.277	0.017	-2.581	5.010	5.261	0.002	0.249
5.257	5.520	0.002	0.012	5.206	5.466	0.011	0.044
5.544	5.822	0.000	0.064	5.469	5.742	0.003	2.881
5.634	5.915	0.001	1.612	5.667	5.950	0.003	-2.389
5.646	5.929	0.001	-0.881	5.823	6.114	0.055	5.666
5.705	5.990	0.001	-7.115	5.870	6.164	0.000	-0.068
5.805	6.095	0.055	3.647	5.918	6.213	0.001	4.797
5.986	6.286	0.008	2.669	5.944	6.241	0.014	-16.027
6.025	6.326	0.013	-5.474	6.087	6.391	0.001	-1.213

Table A.3: Continued. The oscillator strength and rotatory strength of (*S*)-NPNPSA calculated with B3LYP/apVDZ. E' is the shifted energy used to fit experimental and theoretical UV/vis absorption, f is the dimensionless oscillator strength, and R is the rotational strength in 10^{-40} erg esu cm Gauss^{-1}.

Conformer 3				Conformer 4			
E (eV)	E' (eV)	f	R	E (eV)	E' (eV)	f	R
3.715	4.086	0.000	-2.528	3.719	4.091	0.001	-9.217
3.859	4.245	0.000	1.281	3.837	4.221	0.000	-2.757
4.038	4.442	0.021	1.473	4.045	4.450	0.029	0.831
4.300	4.730	0.000	-0.887	4.312	4.743	0.000	-0.772
4.478	4.702	0.338	6.796	4.480	4.704	0.256	16.485
4.819	5.060	0.070	-16.411	4.973	5.222	0.065	-13.788
5.222	5.483	0.004	0.368	5.234	5.496	0.002	-0.825
5.288	5.552	0.005	1.257	5.412	5.683	0.005	-32.327
5.465	5.739	0.005	-31.527	5.429	5.701	0.005	2.649
5.510	5.785	0.003	1.783	5.462	5.735	0.001	-0.353
5.672	5.956	0.005	1.437	5.592	5.872	0.006	-8.135
5.757	6.045	0.059	0.627	5.768	6.057	0.002	-1.872
5.767	6.055	0.000	-0.082	5.780	6.070	0.052	5.585
5.885	6.180	0.007	-5.413	5.799	6.089	0.009	-1.009
5.913	6.209	0.004	2.823	5.960	6.258	0.035	12.816

Table A.4: The oscillator strength and rotatory strength of (S)-NPNPSA calculated with B3LYP/apVDZ. E' is the shifted energy used to fit experimental and theoretical UV/vis absorption, f is the dimensionless oscillator strength, and R is the rotational strength in 10^{-40} erg esu cm Gauss^{-1}.

Conformer 1				Conformer 2			
E (eV)	E' (eV)	f	R	E (eV)	E' (eV)	f	R
3.753	4.128	0.000	-0.173	3.762	4.138	0.000	-0.991
4.128	4.541	0.008	-4.750	4.109	4.520	0.014	-6.470
4.216	4.637	0.025	0.274	4.244	4.668	0.093	-4.396
4.306	4.736	0.000	-0.157	4.317	4.749	0.000	2.902
4.578	4.806	0.200	-12.442	4.783	5.022	0.065	10.663
5.039	5.291	0.117	9.265	4.882	5.126	0.141	-7.041
5.244	5.506	0.016	-4.277	5.211	5.472	0.002	-0.418
5.386	5.655	0.001	-0.173	5.413	5.683	0.012	-1.855
5.569	5.848	0.000	-0.127	5.663	5.946	0.003	1.973
5.757	6.044	0.001	-2.423	5.816	6.107	0.004	-0.299
5.836	6.128	0.000	-1.537	5.921	6.217	0.000	-0.019
5.859	6.152	0.001	2.104	5.955	6.253	0.044	3.833
5.910	6.206	0.042	4.738	6.028	6.330	0.001	-0.338
6.073	6.376	0.003	2.460	6.131	6.438	0.010	-9.684
6.159	6.467	0.013	-6.962	6.336	6.653	0.015	1.213

Table A.4: Continued. The oscillator strength and rotatory strength of (*S*)-NPNPSA calculated with B3LYP/6-31G(d). E' is the shifted energy used to fit experimental and theoretical UV/vis absorption, f is the dimensionless oscillator strength, and R is the rotational strength in 10^{-40} erg esu cm Gauss^{-1}.

Conformer 3				Conformer 4			
E (eV)	E' (eV)	f	R	E (eV)	E' (eV)	f	R
3.746	4.121	0.000	-2.867	3.752	4.128	0.000	-0.173
3.891	4.280	0.007	2.076	4.128	4.541	0.008	-4.750
4.210	4.631	0.022	0.249	4.216	4.637	0.025	0.274
4.291	4.720	0.000	0.071	4.306	4.736	0.000	-0.157
4.606	4.836	0.281	8.825	4.578	4.806	0.200	-12.442
4.971	5.220	0.110	-17.952	5.039	5.291	0.117	9.265
5.316	5.582	0.003	-0.167	5.244	5.506	0.016	-4.277
5.435	5.706	0.002	1.037	5.386	5.655	0.001	-0.173
5.531	5.807	0.004	-25.237	5.569	5.848	0.000	-0.127
5.679	5.963	0.006	0.287	5.757	6.044	0.001	-2.423
5.733	6.020	0.006	3.001	5.836	6.128	0.000	-1.537
5.868	6.161	0.039	-0.067	5.859	6.152	0.001	2.104
5.901	6.196	0.004	0.404	5.910	6.206	0.042	4.738
6.020	6.321	0.004	-2.455	6.073	6.376	0.003	2.460
6.109	6.415	0.002	2.587	6.159	6.467	0.013	-6.962

A.2 Vibrational Corrections for the Relevant Conformers of NPNPA and NPNPSA

This appendix has the calculated vibrational correction factors for both NPNPA and NPNPSA. Each Table has the following items in it:

- Freq=transition frequency in inverse centimeters.
- $< x^2 >$=Expectation value for the displacement squared.
- $[\alpha]_{436}$=Correction factor at 436 nm.
- $[\alpha]_{589}$=Correction factor at 589 nm.
- $[\alpha_{436}](q - \delta q)$=Value of the ORD at 436 nm when normal mode is diplaced by -0.05.
- $[\alpha_{589}](q - \delta q)$=Value of the ORD at 589 nm when normal mode is diplaced by -0.05.
- $[\alpha_{436}](q + \delta q)$=Value of the ORD at 436 nm when normal mode is diplaced by 0.05.
- $[\alpha_{589}](q + \delta q)$=Value of the ORD at 589 nm when normal mode is diplaced by 0.05.

Table A.5: Vibrational corrections from each normal mode of conformer 1 of NPNPA.

Freq	$< x^2 >$	$[\alpha]_{436}$	$[\alpha]_{589}$	$[\alpha_{436}](q-\delta q)$	$[\alpha_{436}](q+\delta q)$	$[\alpha]_{589}(q-\delta q)$	$[\alpha]_{589}(q+\delta q)$
30.09	7.73	6309.37	1051.56	-252.49	-350.67	-142.27	-168.93
55.44	2.29	-12154.40	-768.22	-351.71	-266.78	-162.00	-150.38
61.32	1.87	-29.94	-29.94	-302.41	-302.83	-156.58	-155.00
83.48	1.02	-10301.70	-564.87	-498.57	-131.98	-186.88	-126.05
94.95	0.79	-3005.83	-246.02	-228.31	-386.42	-143.14	-169.18
113.17	0.56	-143.09	-60.37	-244.95	-360.89	-144.55	-167.26
198.35	0.19	-32.84	-14.51	-264.91	-340.72	-144.94	-166.79
226.51	0.15	399.37	7.17	-338.19	-260.33	-158.06	-153.36
230.84	0.14	-32.34	-24.84	-326.55	-279.21	-161.88	-150.09
280.40	0.10	-821.07	-169.76	-314.39	-310.93	-160.91	-154.79
286.04	0.10	-82.77	-31.14	-249.85	-357.45	-139.90	-172.43
334.81	0.08	202.18	16.57	-271.16	-327.33	-154.38	-156.61
395.17	0.06	46.49	8.98	-373.74	-229.44	-179.26	-131.89
418.56	0.05	139.27	25.04	6.57	-605.15	-86.70	-223.65
437.33	0.05	55.67	18.88	-290.74	-311.63	-157.94	-152.64
464.80	0.04	252.41	71.27	-195.31	-395.83	-123.64	-183.93
501.23	0.04	116.43	38.92	-270.56	-327.40	-146.63	-162.49
528.66	0.04	198.93	16.25	-325.15	-266.71	-153.46	-156.99
561.74	0.03	36.34	6.31	-286.44	-316.11	-150.20	-160.88
590.65	0.03	18.33	8.59	-311.82	-291.95	-159.75	-151.12
616.05	0.03	-27.40	-9.46	-275.68	-331.78	-152.51	-159.81
644.03	0.03	-2.06	-6.30	-380.58	-224.80	-169.64	-142.45
687.02	0.03	-137.42	-21.32	-171.01	-447.21	-129.11	-184.45
705.21	0.03	635.65	135.41	-186.77	-356.23	-128.60	-169.69
746.00	0.02	59.28	24.92	-343.47	-255.52	-165.01	-143.92
759.88	0.02	-48.00	-27.74	-245.16	-365.18	-135.69	-178.82
813.05	0.02	11.73	0.26	-228.53	-375.31	-138.63	-172.88
831.72	0.02	-133.98	-23.03	-222.20	-398.94	-142.78	-171.50
842.81	0.02	-34.69	-13.99	-375.10	-234.29	-172.92	-140.31
847.37	0.02	-23.94	-8.31	-309.06	-299.05	-159.50	-153.05
869.96	0.02	-38.26	-3.83	-366.08	-243.91	-170.62	-141.40
946.95	0.02	7.49	0.87	-310.74	-293.43	-153.89	-157.53
970.80	0.02	2.26	4.67	-348.56	-256.32	-164.09	-146.79
983.29	0.02	7.68	6.70	-293.20	-310.90	-150.75	-159.83
1012.71	0.02	2.10	3.85	-475.97	-128.92	-192.07	-118.90
1090.81	0.02	29.98	9.87	-337.90	-262.50	-173.65	-136.31
1102.71	0.02	-12.41	-3.58	-470.11	-137.10	-204.51	-107.61
1140.52	0.01	31.47	6.97	-325.99	-273.93	-158.21	-152.16
1143.84	0.01	-17.83	-5.23	-244.49	-363.71	-143.42	-169.00
1160.55	0.01	-19.20	-6.91	-311.45	-297.03	-156.19	-156.53
1206.56	0.01	-13.72	-6.86	-348.16	-259.48	-169.84	-142.92
1218.94	0.01	3.78	-0.83	-364.13	-240.39	-171.01	-140.68
1295.88	0.01	17.65	3.71	-208.50	-393.32	-135.58	-175.25
1322.80	0.01	23.94	7.62	-165.51	-435.01	-118.83	-191.22
1339.17	0.01	66.06	-1.67	-418.45	-173.67	-184.14	-127.73
1352.77	0.01	53.59	6.25	-255.43	-339.05	-136.40	-173.89
1363.95	0.01	23.94	6.79	-406.33	-194.04	-191.50	-118.67
1403.87	0.01	8.91	-6.84	-261.72	-341.63	-156.62	-156.34
1412.74	0.01	2.97	-0.77	-223.62	-380.96	-134.31	-177.39
1437.98	0.01	-26.31	-8.08	-319.34	-291.46	-159.71	-153.55
1481.04	0.01	-35.16	-7.52	-361.94	-250.97	-166.81	-146.38
1510.79	0.01	-11.58	-4.65	-266.53	-341.26	-150.59	-161.99
1517.00	0.01	-3.47	-1.96	-355.54	-250.44	-173.80	-138.18
1528.07	0.01	-12.06	-4.29	-346.85	-261.08	-163.98	-148.53
1551.19	0.01	-309.84	-57.44	-161.44	-514.96	-126.10	-198.64
1580.93	0.01	-17.85	-7.39	-368.35	-241.03	-173.62	-139.65
1626.67	0.01	43.93	8.92	-157.09	-437.52	-120.62	-188.77
1653.55	0.01	-28.12	-15.14	-369.99	-242.10	-168.17	-147.08
1806.25	0.01	26.77	7.62	-338.09	-259.94	-167.65	-141.85
3015.88	0.01	30.21	10.66	-209.90	-381.79	-121.89	-184.88
3064.28	0.01	-8.56	-2.86	-273.16	-335.93	-144.33	-168.51
3140.21	0.01	-12.28	-4.21	-271.58	-339.34	-148.83	-164.67
3149.97	0.01	-4.28	-1.46	-318.54	-288.66	-160.32	-151.90
3150.14	0.01	-4.28	-1.50	-236.30	-370.90	-134.87	-177.37
3195.74	0.01	10.28	1.73	-285.68	-314.65	-153.01	-157.71
3204.04	0.01	-7.72	-3.33	-279.39	-329.48	-151.50	-161.62
3207.48	0.01	2.40	1.37	-278.56	-325.50	-151.20	-159.69
3575.03	0.00	-22.71	-7.41	-396.85	-220.39	-178.32	-137.15
3661.56	0.00	4.99	1.73	-313.85	-288.64	-159.47	-151.13

Table A.6: Vibrational corrections from each normal mode of conformer 3 of NPNPA.

Freq	$< x^2 >$	$[\alpha]_{436}$	$[\alpha]_{589}$	$[\alpha_{436}](q - \delta q)$	$[\alpha_{436}](q + \delta q)$	$[\alpha]_{589}(q - \delta q)$	$[\alpha]_{589}(q + \delta q)$
33.31	7.73	-530.20	-656.44	-822.47	-826.02	-336.36	-338.50
48.52	2.29	-10004.93	-95.40	-741.19	-915.48	-321.01	-353.67
59.17	1.87	-4378.98	-1566.79	-742.90	-910.83	-315.34	-361.21
78.38	1.02	-5233.73	-216.35	-1072.38	-587.27	-384.72	-290.35
99.01	0.79	101.66	69.71	-827.37	-820.56	-333.54	-340.82
133.92	0.56	-127.35	-24.18	-838.21	-810.86	-340.95	-333.80
201.38	0.19	51.23	-2.97	-830.20	-817.39	-337.31	-337.33
236.08	0.15	42.14	19.41	-789.78	-857.74	-323.60	-350.65
259.30	0.14	-89.01	-42.16	-833.25	-816.93	-333.52	-341.98
277.63	0.10	-131.21	-26.16	-820.66	-830.78	-336.96	-338.27
303.44	0.10	-19.57	-19.93	-863.25	-785.58	-350.65	-324.51
335.11	0.08	-109.81	-34.00	-930.82	-721.11	-377.55	-298.18
351.21	0.06	-13.36	-3.06	-868.35	-780.41	-346.49	-328.22
423.03	0.05	92.51	12.42	-545.26	-1098.55	-278.43	-395.57
453.53	0.05	48.23	12.10	-815.05	-830.64	-335.99	-337.96
504.17	0.04	66.18	21.05	-832.12	-812.01	-334.98	-338.30
524.27	0.04	215.45	67.59	-728.81	-905.19	-309.21	-360.91
539.01	0.04	268.09	66.19	-723.35	-906.46	-311.42	-358.62
577.21	0.03	35.03	6.61	-747.70	-897.93	-316.80	-357.30
637.25	0.03	-36.09	-1.74	-906.83	-744.56	-359.94	-314.81
665.45	0.03	137.85	37.23	-849.32	-786.41	-347.09	-324.12
682.73	0.03	46.80	16.70	-806.15	-837.73	-331.65	-341.38
703.61	0.03	78.60	10.97	-645.30	-995.31	-283.56	-389.97
717.07	0.03	-283.58	-93.62	-1043.97	-632.63	-413.11	-270.84
751.35	0.02	-167.35	-59.44	-947.17	-718.79	-379.03	-301.85
763.80	0.02	-183.69	-58.85	-900.82	-767.25	-361.67	-319.27
816.91	0.02	23.17	4.89	-795.77	-849.81	-328.39	-345.64
825.89	0.02	56.69	10.00	-718.98	-922.61	-311.18	-362.24
834.31	0.02	169.86	14.49	-751.20	-876.80	-322.29	-350.58
852.92	0.02	-19.44	-8.98	-832.36	-818.30	-340.18	-335.52
873.08	0.02	-10.42	-6.44	-891.64	-757.95	-357.49	-317.92
964.74	0.02	11.61	2.78	-838.26	-808.39	-341.43	-332.78
971.61	0.02	15.20	5.16	-872.00	-774.13	-346.14	-327.73
982.19	0.02	16.70	7.75	-813.31	-832.58	-331.97	-341.52
1018.81	0.02	-22.77	-3.09	-885.00	-766.67	-351.38	-323.68
1056.24	0.02	-18.48	-7.82	-797.62	-853.52	-330.37	-345.44
1113.22	0.02	-15.22	-7.34	-781.10	-869.67	-323.59	-352.21
1136.66	0.01	39.30	5.68	-815.90	-825.81	-336.74	-336.91
1145.51	0.01	-5.81	-3.38	-823.13	-826.13	-339.69	-335.48
1178.33	0.01	-3.46	-3.69	-846.47	-802.41	-344.46	-330.78
1217.00	0.01	-7.19	-2.17	-848.02	-801.55	-347.79	-327.20
1226.07	0.01	-50.98	-18.30	-884.18	-773.32	-357.58	-320.33
1296.54	0.01	28.77	7.88	-893.49	-749.28	-353.98	-319.11
1330.61	0.01	-61.16	-20.95	-918.34	-741.97	-374.17	-304.55
1341.12	0.01	2.32	-0.25	-829.35	-818.47	-340.35	-334.30
1361.67	0.01	-25.13	-12.61	-915.97	-737.37	-371.22	-305.92
1367.60	0.01	-8.95	-4.30	-843.77	-806.32	-342.66	-332.81
1376.56	0.01	-67.43	-27.70	-982.90	-679.11	-393.83	-286.41
1390.14	0.01	18.09	-4.91	-941.91	-702.65	-373.83	-301.78
1429.87	0.01	-0.61	-1.42	-826.78	-821.63	-337.71	-337.19
1463.53	0.01	1.75	3.09	-789.23	-858.67	-329.51	-344.42
1516.38	0.01	3.21	0.76	-790.27	-857.29	-325.39	-349.04
1520.44	0.01	1.82	0.80	-841.71	-806.16	-343.30	-331.12
1528.47	0.01	20.10	4.73	-858.58	-785.15	-347.52	-326.01
1547.92	0.01	4.23	2.35	-863.67	-783.64	-348.70	-325.36
1575.38	0.01	124.29	15.30	-844.23	-775.04	-337.71	-333.32
1643.81	0.01	-3.08	1.27	-869.22	-779.81	-346.75	-327.54
1651.44	0.01	-32.16	-5.92	-890.68	-765.47	-357.31	-318.74
1837.88	0.01	68.44	15.74	-820.17	-809.46	-341.45	-328.86
3027.21	0.01	-11.49	-4.39	-788.21	-865.23	-327.83	-348.74
3058.79	0.01	-4.98	-1.94	-816.51	-834.03	-334.02	-341.46
3131.60	0.01	-3.08	-1.03	-835.66	-814.05	-339.23	-335.85
3148.16	0.01	2.76	0.60	-821.50	-825.49	-337.10	-337.22
3156.31	0.01	-5.21	-1.94	-831.06	-819.66	-337.79	-337.72
3185.58	0.01	-1.14	-0.59	-823.21	-825.61	-337.64	-337.24
3203.58	0.01	-0.86	-0.65	-829.78	-818.91	-338.62	-336.29
3204.79	0.01	-3.41	-1.89	-830.93	-818.97	-339.02	-336.48
3530.91	0.00	-15.79	-5.19	-782.67	-873.88	-320.80	-356.52
3567.12	0.00	-2.93	-2.68	-936.01	-713.82	-370.73	-305.29

Table A.7: Vibrational corrections from each normal mode of conformer 2 of *S*-NPNPSA.

Freq	$< x^2 >$	$[\alpha]_{436}$	$[\alpha]_{589}$	$[\alpha_{436}](q - \delta q)$	$[\alpha_{436}](q + \delta q)$	$[\alpha]_{589}(q - \delta q)$	$[\alpha]_{589}(q + \delta q)$
17.72	7.73	-19140.31	-5510.09	-124.80	-137.60	-27.71	-32.68
27.20	2.29	-3981.88	-1149.41	-133.73	-127.66	-30.62	-29.48
40.23	1.87	-1860.42	-563.76	-138.81	-122.60	-32.15	-27.97
55.02	1.02	-40.30	-171.26	-263.82	3.36	-65.96	5.97
67.40	0.79	-733.51	-195.15	-113.37	-148.14	-24.75	-35.36
87.74	0.56	-403.34	-111.82	-127.86	-133.57	-30.16	-29.94
121.13	0.19	-339.34	-93.32	-125.13	-136.89	-28.20	-32.06
155.98	0.15	-136.54	-39.01	-131.57	-129.90	-30.61	-29.51
160.82	0.14	-30.66	-2.45	-129.59	-131.08	-30.08	-29.76
217.07	0.10	-91.30	-29.27	-133.80	-127.93	-31.16	-29.08
226.12	0.10	-95.67	-26.50	-132.67	-129.23	-31.22	-29.01
256.70	0.08	-56.46	-19.50	-128.69	-132.83	-29.32	-30.88
260.35	0.06	-89.07	-23.52	-125.18	-137.02	-28.18	-32.11
300.94	0.05	-24.80	-8.91	-134.68	-126.38	-31.13	-28.92
317.67	0.05	-41.99	-9.88	-143.76	-117.85	-33.21	-26.89
328.06	0.04	-35.74	-11.69	-136.15	-125.34	-30.84	-29.33
401.74	0.04	-32.30	-10.53	-158.15	-103.62	-36.81	-23.45
411.66	0.04	-15.42	-2.53	-61.94	-199.15	-14.99	-44.94
423.07	0.03	-62.40	-18.52	-164.15	-99.10	-38.03	-22.63
445.34	0.03	-43.99	-11.20	-110.16	-152.42	-24.68	-35.69
469.62	0.03	-37.77	-10.90	-132.66	-129.77	-29.19	-31.21
496.75	0.03	-5.70	-1.38	-144.51	-116.24	-33.39	-26.51
532.76	0.03	-48.60	-8.91	-141.57	-121.96	-30.75	-29.64
540.21	0.03	-16.85	-8.43	-135.34	-126.18	-33.23	-27.14
569.39	0.02	-19.65	-6.12	-113.40	-148.40	-22.92	-37.33
586.75	0.02	-15.03	-4.92	-120.36	-141.16	-26.80	-33.38
619.85	0.02	-28.18	-11.68	-128.37	-134.27	-32.25	-28.49
633.21	0.02	-13.20	-2.84	-127.74	-133.75	-26.94	-33.11
635.71	0.02	-15.84	-3.56	-126.98	-134.73	-29.04	-31.07
693.07	0.02	-32.30	-7.58	-148.99	-114.37	-36.93	-23.58
732.17	0.02	-27.81	-10.78	-125.09	-138.04	-28.24	-32.63
743.10	0.02	-36.58	-10.98	-124.15	-139.90	-28.80	-32.11
756.18	0.02	-20.13	-4.54	-135.36	-127.10	-30.81	-29.47
832.58	0.02	-7.04	-1.50	-123.83	-137.39	-28.17	-31.82
840.07	0.02	-9.67	-2.87	-152.10	-109.43	-35.03	-25.12
862.81	0.02	-11.32	-2.28	-129.96	-131.80	-31.56	-28.53
872.24	0.02	-10.01	-1.92	-123.53	-138.09	-28.18	-31.87
889.26	0.01	-27.34	-6.12	-126.07	-137.70	-30.95	-29.62
972.37	0.01	-19.65	-4.80	-114.36	-148.72	-25.57	-34.90
983.17	0.01	-6.64	-2.85	-107.78	-153.55	-25.09	-35.12
991.52	0.01	-6.14	-0.43	-146.10	-115.17	-32.88	-27.00
1026.31	0.01	-6.20	-1.67	-127.56	-133.75	-29.22	-30.84
1081.93	0.01	-30.79	-6.78	-160.23	-104.87	-38.55	-22.30
1088.94	0.01	-12.28	-4.05	-135.71	-126.59	-33.72	-26.72
1123.94	0.01	-13.46	-3.41	-123.24	-139.31	-29.09	-31.27
1126.16	0.01	-22.89	-4.48	-154.56	-109.49	-36.43	-24.10
1127.86	0.01	-11.65	-3.34	-126.59	-135.68	-28.53	-31.82
1136.07	0.01	-8.68	-2.69	-130.00	-131.81	-30.22	-30.03
1142.17	0.01	-11.43	-2.86	-139.74	-122.52	-34.02	-26.26
1199.88	0.01	-12.33	-3.78	-130.17	-132.34	-28.66	-31.80
1201.42	0.01	-2.42	-1.00	-135.41	-125.42	-31.71	-28.28
1281.17	0.01	-18.91	-5.90	-135.74	-128.11	-32.76	-28.13

Table A.7: Vibrational corrections from each normal mode of conformer 2 of *S*-NPNPSA.

Freq	$< x^2 >$	$[\alpha]_{436}$	$[\alpha]_{589}$	$[\alpha_{436}](q-\delta q)$	$[\alpha_{436}](q+\delta q)$	$[\alpha]_{589}(q-\delta q)$	$[\alpha]_{589}(q+\delta q)$
53 1308.63	0.01	-6.90	-1.35	-118.46	-143.24	-23.41	-36.66
54 1325.96	0.01	-5.37	-1.70	-120.69	-140.74	-26.24	-33.90
55 1362.76	0.01	-9.67	-2.69	-119.08	-143.21	-25.41	-34.93
56 1370.24	0.01	20.89	4.48	-107.37	-148.99	-23.09	-35.86
57 1375.65	0.01	-16.34	-5.43	-132.68	-130.93	-31.66	-29.22
58 1396.09	0.01	-280.16	-36.89	-76.60	-239.33	-16.85	-50.28
59 1435.80	0.01	-1.77	0.15	-136.14	-124.64	-33.45	-26.34
60 1436.86	0.01	-8.09	-2.21	-101.14	-160.93	-18.46	-41.81
61 1450.39	0.01	-10.63	-3.45	-124.08	-138.53	-26.52	-34.01
62 1517.97	0.01	-4.26	-1.16	-128.96	-132.38	-29.03	-31.04
63 1519.51	0.01	-5.33	-1.48	-130.96	-130.61	-30.06	-30.08
64 1521.77	0.01	-3.51	-0.92	-132.31	-128.87	-30.66	-29.36
65 1597.94	0.01	13.07	2.29	-106.17	-151.28	-23.07	-36.23
66 1637.28	0.01	-57.55	-12.75	-82.46	-191.36	-15.30	-47.49
67 1658.31	0.01	4.96	3.18	-156.85	-102.40	-37.91	-21.16
68 1799.02	0.00	-13.16	-3.59	-151.74	-112.05	-39.16	-21.58
69 2999.97	0.00	-12.97	-5.13	-106.90	-159.06	-19.80	-42.21
70 3070.47	1.00	1.49	0.96	-113.39	-146.38	-22.42	-36.98
71 3143.73	2.00	4.78	2.35	-118.11	-140.17	-24.07	-34.70
72 3157.19	3.00	-3.43	-1.22	-160.65	-101.31	-43.42	-16.95
73 3169.29	4.00	-3.92	-1.44	-132.88	-129.31	-31.49	-28.98
74 3194.99	5.00	-0.86	-0.04	-132.30	-128.51	-30.98	-28.86
75 3204.28	6.00	-3.53	-1.36	-136.82	-125.21	-33.26	-27.18
76 3205.67	7.00	-2.17	-0.57	-135.85	-125.56	-32.21	-27.87
77 3464.06	8.00	-4.36	-0.71	-149.79	-112.78	-35.18	-24.99
78 3664.18	9.00	-3.03	-1.00	-136.33	-125.67	-32.05	-28.29

Table A.8: Vibrational corrections from each normal mode of conformer 4 of *S*-NPNPSA.

Freq	$< x^2 >$	$[\alpha]_{436}$	$[\alpha]_{589}$	$[\alpha_{436}](q-\delta q)$	$[\alpha_{436}](q+\delta q)$	$[\alpha]_{589}(q-\delta q)$	$[\alpha]_{589}(q+\delta q)$
4.59	7.73	-402334.82	-56240.35	-671.37	-631.08	-261.72	-255.13
27.89	2.29	-1288.06	-741.61	-651.63	-648.36	-257.81	-258.84
49.40	1.87	-5216.98	-599.08	-689.14	-614.70	-267.55	-249.39
52.56	1.02	-11981.30	-1014.99	-593.79	-716.73	-244.94	-272.44
75.53	0.79	-2115.70	-596.05	-669.30	-634.30	-266.90	-250.67
91.58	0.56	-88.09	-88.09	-652.53	-647.37	-258.94	-257.76
138.30	0.19	22.95	11.48	-647.26	-652.26	-256.86	-259.53
156.98	0.15	-6.42	-28.26	-629.24	-670.47	-251.72	-264.96
194.82	0.14	195.24	67.35	-652.03	-645.34	-258.05	-257.62
228.71	0.10	96.22	41.15	-647.66	-650.48	-255.73	-260.08
237.22	0.10	-1.18	-4.14	-655.17	-644.51	-260.54	-255.99
251.00	0.08	78.56	29.93	-679.06	-619.13	-268.45	-247.45
267.04	0.06	132.46	41.60	-652.49	-644.40	-259.87	-255.72
287.59	0.05	84.71	28.94	-624.71	-672.93	-250.62	-265.15
306.32	0.05	-13.15	-10.14	-646.68	-653.33	-257.35	-259.38
349.51	0.04	137.22	41.74	-638.32	-656.77	-255.08	-259.99
364.48	0.04	-10.64	-6.44	-682.81	-617.23	-272.09	-244.60
383.42	0.04	57.25	21.15	-693.35	-604.09	-271.93	-243.71
412.36	0.03	51.88	19.51	-679.97	-617.43	-263.91	-251.70
448.37	0.03	55.02	21.36	-665.34	-631.59	-264.50	-250.90
460.26	0.03	-38.54	-12.20	-652.55	-649.10	-256.90	-260.19
475.00	0.03	63.73	19.95	-654.34	-641.87	-259.03	-256.35
513.93	0.03	6.25	2.47	-687.87	-611.41	-273.16	-243.15
536.47	0.03	71.49	15.01	-670.89	-624.15	-265.38	-250.11
543.44	0.02	-15.80	-6.99	-681.33	-619.37	-269.85	-247.07

Table A.8: Vibrational corrections from each normal mode of conformer 4 of *S*-NPNPSA.

Freq	$< x^2 >$	$[\alpha]_{436}$	$[\alpha]_{589}$	$[\alpha_{436}](q-\delta q)$	$[\alpha_{436}](q+\delta q)$	$[\alpha]_{589}(q-\delta q)$	$[\alpha]_{589}(q+\delta q)$
586.33	0.02	-41.30	-6.84	-673.62	-629.06	-261.82	-255.14
621.15	0.02	8.73	7.34	-670.86	-628.11	-264.11	-251.77
634.81	0.02	18.20	2.58	-664.99	-633.19	-261.74	-254.51
689.41	0.02	114.48	28.87	-641.03	-648.28	-255.20	-258.65
704.12	0.02	6.03	4.63	-634.38	-664.72	-248.64	-267.39
740.79	0.02	-73.74	-11.94	-714.69	-592.26	-280.31	-237.33
754.38	0.02	-67.08	-25.43	-645.59	-660.85	-256.04	-262.99
762.41	0.02	-2.34	1.27	-670.89	-629.01	-265.99	-250.34
832.31	0.02	-27.65	-8.89	-651.15	-651.65	-261.62	-255.85
840.18	0.02	-0.44	0.00	-635.73	-663.98	-255.91	-260.55
858.89	0.02	-84.65	-10.44	-610.72	-698.91	-248.31	-269.38
872.09	0.02	-11.60	-3.50	-653.45	-647.60	-262.37	-254.51
876.69	0.01	-23.22	-2.49	-620.59	-681.87	-251.37	-265.39
971.85	0.01	3.10	-0.07	-646.51	-652.73	-257.21	-259.26
984.98	0.01	-3.20	-1.53	-658.79	-641.31	-260.24	-256.43
991.03	0.01	4.12	2.97	-641.20	-657.89	-256.03	-260.02
1025.05	0.01	8.44	3.07	-709.91	-588.54	-271.61	-244.41
1064.92	0.01	-21.75	-7.63	-647.64	-655.27	-254.79	-262.81
1070.65	0.01	-13.91	-4.32	-650.87	-650.88	-260.40	-256.71
1119.07	0.01	-60.37	-14.47	-608.71	-700.46	-249.21	-269.53
1125.32	0.01	-27.26	-3.09	-682.87	-621.11	-263.63	-253.32
1126.08	0.01	-14.82	-1.95	-691.25	-610.76	-271.49	-245.28
1137.97	0.01	-1.56	-0.50	-657.67	-642.24	-260.43	-256.11
1150.06	0.01	4.07	1.97	-643.19	-655.81	-254.14	-262.00
1203.17	0.01	1.06	0.18	-655.98	-643.50	-259.55	-256.88
1234.09	0.01	-8.48	-2.69	-669.13	-632.01	-266.45	-250.48
1268.69	0.01	18.43	8.30	-647.62	-648.73	-254.45	-260.52
1327.99	0.01	-3.19	-0.05	-654.70	-645.56	-260.26	-256.21
1333.65	0.01	9.36	5.98	-623.21	-674.68	-250.14	-265.19
1348.57	0.01	-12.55	-3.45	-650.94	-651.12	-259.70	-257.42
1369.59	0.01	47.30	15.13	-723.11	-567.36	-278.76	-234.76
1389.59	0.01	-19.52	-3.75	-615.84	-687.67	-246.37	-270.83
1396.91	0.01	150.72	31.73	-618.63	-651.15	-258.31	-251.86
1437.02	0.01	1.03	0.05	-641.91	-657.54	-253.99	-262.46
1437.85	0.01	-1.18	-0.59	-642.58	-657.32	-258.42	-258.16
1450.91	0.01	19.27	7.96	-641.27	-654.42	-251.80	-263.02
1510.31	0.01	-1.12	-1.12	-652.07	-647.83	-259.55	-257.15
1515.45	0.01	3.81	1.35	-652.01	-646.83	-258.87	-257.30
1518.45	0.01	-8.11	-2.22	-678.79	-622.62	-264.67	-252.27
1599.88	0.01	-181.11	-32.40	-679.10	-661.76	-260.29	-263.54
1636.39	0.01	-65.91	-11.95	-693.53	-621.47	-266.77	-252.47
1658.96	0.01	-62.55	-2.16	-566.18	-748.24	-235.80	-281.17
1830.85	0.00	-27.98	-5.49	-686.78	-620.17	-273.83	-244.06
3043.31	0.00	7.87	3.39	-640.65	-655.60	-252.98	-262.01
3071.83	1.00	0.25	0.05	-641.47	-658.08	-255.23	-261.21
3146.31	2.00	1.50	0.45	-655.72	-643.27	-261.25	-255.01
3157.63	3.00	-1.71	-1.00	-665.31	-635.12	-265.25	-251.66
3167.30	4.00	-0.22	-0.42	-626.66	-673.10	-251.41	-265.24
3191.64	5.00	-1.52	-0.84	-653.07	-647.28	-258.85	-257.99
3203.02	6.00	-1.14	-0.31	-642.27	-657.91	-255.03	-261.57
3205.15	7.00	-0.37	-0.02	-661.95	-637.88	-260.89	-255.58
3439.78	8.00	4.53	1.98	-637.96	-659.48	-252.77	-262.72
3532.48	9.00	-3.56	-1.03	-652.20	-649.25	-260.15	-256.83

Vita

Jason Lambert was born in a small rural town called Falls Mills in the mountains of Southwestern Virginia. He was the first person in his family to obtain a college degree. During high school he took mathematics and english courses at Shawnee State University. From there He attended Berea College from 2002-2006 graduating with a Bachelor's of Arts in mathematics and physics. He subsequently entered the graduate school at the university of Tennessee where he was the reciepient of the Neilson Fellowship in spectroscopy. In 2007 he obtained the second highest score on his Ph'D qualifying exam out of about 30 students. Dr. Lambert graduated with a 3.84 GPA for his doctoral courses. His work has centered around the theoretical and experimental analysis of the optical properties of chiral molecules.